Metal Oxides as Photocatalysts for Selective Oxidations

by

Aaron Proctor

A dissertation submitted in partial fulfillment
of the requirements for the degree of
Doctor of Philosophy
(Chemistry)
in the University of Michigan
2020

Doctoral Committee:

Professor Bart M. Bartlett, Chair
Assistant Professor Bryan R. Goldsmith
Professor Stephen Maldonado
Professor Corey R. J. Stephenson

Aaron Proctor

aarproct@umich.edu

ORCID iD: 0000-0001-8384-6746

To those who keep curiosity alive in others

Acknowledgements

I'd like to first acknowledge the fellow Bartlett lab members I spent almost every day with during this work. To those that began before me – Ben, Kayla, Emily, Frances, Jimmy, Charles, and Sam. You all passed down experimental, theoretical, and presentation-crafting knowledge that will stick with me for the rest of my scientific career. A heartfelt thanks to Jimmy and Kim specifically – your presence and support through some particularly difficult times meant the absolute world to me. To those that began with or after me – Adam, Andy, John, Dan, Kori, Brad, and Christian. You all were a blast to be around at or outside of work. I will always be grateful for the comradery and friendship that formed in the lab. To the undergraduate researcher I had the pleasure of mentoring – Shobhana. It was a joy to work with you. I always admired your optimism and energy. I'm proud of the work we were able to publish together.

To my research advisor – Bart. Though I was completely new to the science you were exploring, you allowed me to join your group, and I want to thank you for that. You were also there to support me when I questioned myself as a scientist. I am confident that not all advisors would have exhibited the compassion you did. Thank you for motivating me to push through and keep moving forward. The time I spent in your lab made me a better scientist and person. I am grateful I had the opportunity to contribute to your science, and I wish you all the best in its continuation.

To my thesis committee – Stephen Maldonado, Corey Stephenson, Mark Barteau, and Bryan Goldsmith. Thank you for your suggestions during my candidacy and data meetings. You all helped develop my experimental design skills as I progressed in my research. I thank you for

your patience and input. A special thank you to Bryan for stepping in as my cognate member when Mark had to vacate the role after pursuing an opportunity at another university. To my master's research advisor – Gary Meints. Thank you for allowing me to take my first research steps in your lab. The skills I learned under your leadership helped prepare me for the work I conducted here. To my 8th grade science teacher – Mr. Oswalt. You don't know it, but you were a large driving force behind my interest in science. Your class was the first to make me curious about nature and our descriptions of it.

To my same-year chemistry friends and board game group – Alonso, Michael, and Grayson. Looking back, the regularity with which we maintained our Saturday game nights is astounding. I will always have fond memories of those nights. I hadn't been so excited about a new hobby in a very long time. I was always thrilled to explore the possibilities of these games with you guys. While most of our time was spent thinking and strategizing around a board centered on top of the perfectly sized green table at Grayson's place, we were also able to spend time sharing the highs and lows that come along with chemistry graduate school. I certainly know that I expressed some lows, but they were made substantially more bearable because of your support and advice. Thank you.

I would like to acknowledge the love and support I've received from my parents. I knew I could always call to talk whenever I wanted, and I looked forward to our weekend conversations. Discussing my more difficult times with you likely contributed to my completion of this work more than I realize now. Your words of encouragement were always appreciated, and I love you both. Grandma Barb and Grandpa Gordon, thank you for your financial support throughout the entirety of my time in graduate school. I also appreciated your emails; it always brightened up my day to see one in my inbox. I want to thank my sister and stepparents as well, who I always looked

forward to seeing when I was able to make it back to Missouri each December or when you were able to visit me here. To my aunt – Shonda. You always believed in my success and the value of the path I was taking, and I thank you for communicating that. I'm also thankful you were able to visit Ann Arbor.

I want to acknowledge the health care providers who gave me peace of mind over my years here whenever I became injured. My physical state was and remains important to me. Weightlifting and rock climbing were activities I looked forward to during my time here. When I couldn't put full effort into them because of an injury, it heavily affected me, especially when research wasn't going well. These medical personnel taught me what was wrong and how to best go about recovering. The plans they gave me were invaluable in maintaining my mood and sense of progress. I owe a tremendous amount of thanks to Jason Scott Shellhaas, MD at the University Health Service Sports Medicine who correctly diagnosed me with a sports hernia. He also guided me through how to recover from damaging a pulley in my left ring finger (came in handy when I did it again to my right one) and how best to recover from a shoulder injury. Thank you to Jennifer Shifferd, PT at the University of Michigan University Hospital, Michael McQuillan, DPT and Kerrie Grove, PT at ATI Physical Therapy for the sports hernia physical therapy. My physical condition would be an absolute disaster without these people.

I want to thank my friends from back home in Springfield, MO. Elliott and Tim – it's odd how close of friends I think we still are with how little we communicate. Seeing you back in Missouri always made me miss home more than anything. It's amazing how much an evening with you two can rejuvenate me. Thank you to Tim, Steve, and Jordan for helping me move to Ann Arbor to begin my degree. Ashley – I feel like our friendship is refreshingly unique. Every time I visit home it makes me so happy how effortlessly we communicate and enjoy each other's

company. Jenn, Eric, and Jason – on the few occasions that it was possible to get the old Missouri State chemistry crew back together over the years here, it was always rewarding. Jenn – it was always helpful talking to you about how your and Eric's graduate school experiences compared to mine. I appreciate the advice and encouragement I received from you throughout the tail end of our formal educations.

Seeing the magnitude of support I've received throughout my scientific career concentrated in these paragraphs is utterly overwhelming. I feel beyond fortunate to have been able to compile these descriptions. To each who contributed to my wellbeing and development over these years, you have my gratitude.

Table of Contents

List of Tables

List of Figures

Abstract

Hydrogen gas is an alternative fuel that could be important in reducing global CO_2 emissions. This fuel not only burns cleanly (hydrogen's combustion products are water and energy) but can also be used in other energy-extracting devices, such as fuel cells, to provide electrical energy. While there is an industrial process in place to generate hydrogen gas (i.e. steam reforming), it requires natural gas as a reactant and produces CO_2 as a product. A more environmentally conscious method to generate hydrogen gas is through photoelectrocatalytic (PEC) water splitting. Of the two half-reactions that make up overall water splitting, water oxidation is the slower process. To make PEC water splitting a more viable hydrogen production process, the kinetics of water oxidation must be improved. This thesis focuses on two ways to approach the slow kinetics of water oxidation – first, through modification of the surface of a visible light-absorbing metal oxide with a water oxidation electrocatalyst and second, by exploring photocatalytic organic oxidations to replace water oxidation.

The first approach involves investigating PEC water oxidation on WO_3 coated with FeOOH (WO_3 | FeOOH). Dr. Charles Lhermitte of the Bartlett group discovered that WO_3 | FeOOH had a higher Faradaic efficiency for water oxidation than did bare WO_3. It was not known why. This thesis provides a potential answer. Through •OH trapping experiments, it is shown that the quantity of •OH generated during PEC water oxidation decreases when the deposition time of FeOOH onto WO_3 is increased. This suggests that photogenerated holes in WO_3 travel to the valence band of FeOOH (has an energy more reducing than the potential required to oxidize water to •OH) before reaching the solution. Faradaic efficiency loss for water oxidation on

WO_3 electrodes can be caused by direct and indirect oxidation of electrolyte anions by valence band holes and •OH generated by oxidation of water, respectively. Having the holes travel to a more reducing valence band before oxidizing water shuts down the •OH reaction pathway while also making it more difficult to oxidize electrolyte anions directly. This is a reasonable explanation for the increase in Faradaic efficiency of $WO_3 \mid FeOOH$ vs. bare WO_3 for water oxidation. $WO_3 \mid FeOOH$ was also demonstrated, through Tafel analysis, to possess improved kinetics for water oxidation over bare WO_3 (Tafel slopes of 77 ± 14 and 172 ± 7 mV • dec^{-1}, respectively).

The second approach to improving the slow kinetics of water oxidation was entertaining the idea that water oxidation could be replaced altogether by an organic oxidation. Organic oxidations have the potential to be faster (both thermodynamically and kinetically) while generating a soluble oxidation product that could be more economically and chemically valuable than the starting compound. It also gives rise to the possibility of utilizing sustainable biomass-derived compounds as targets for oxidation. This thesis explores this idea by demonstrating that PEC and photocatalytic oxidation of amines is possible on $CuWO_4$ and $BiVO_4$ catalysts. For the photocatalytic experiments, both $CuWO_4$ and $BiVO_4$ produced the oxidized product in high yields (98-99%) while being first order in amine concentration (first order rate constants of 0.34 and 0.70 h^{-1} • g^{-1}, respectively). While most attempts to photocatalytically oxidize alcohols resulted in no catalysis, evidence for the slow photocatalytic oxidation of glycerol to lactate on Fe_2O_3 and slow production of formic acid from fructose when reacted with WO_3 was obtained.

Chapter 1 Introduction

1.1 Renewable Energy is an Inevitable Component of Future Civilization

Fossil fuels were formed underground over millions of years by application of pressure and heat to buried organic matter.[1] The first instance of humans using one of these energy-rich substances was about 4,000 years ago in northern China where coal was burned for warmth and cooking.[2] Since then, humans have found more creative ways to use the energy released from burning a variety of fossil fuels, and our rate of consuming them continues to increase (Figure 1.1).[3] With so many facets of daily life being powered by these fuels, it is difficult to imagine what the world would look like without them. However, their rate of consumption greatly outpaces their rate of generation, and this means they *will be depleted*. Referencing the rate of fossil fuel production during 2015 and the quantity of fuels in known reserves at that time, coal reserves are estimated to last another ~110 years while oil and natural gas reserves are expected to last

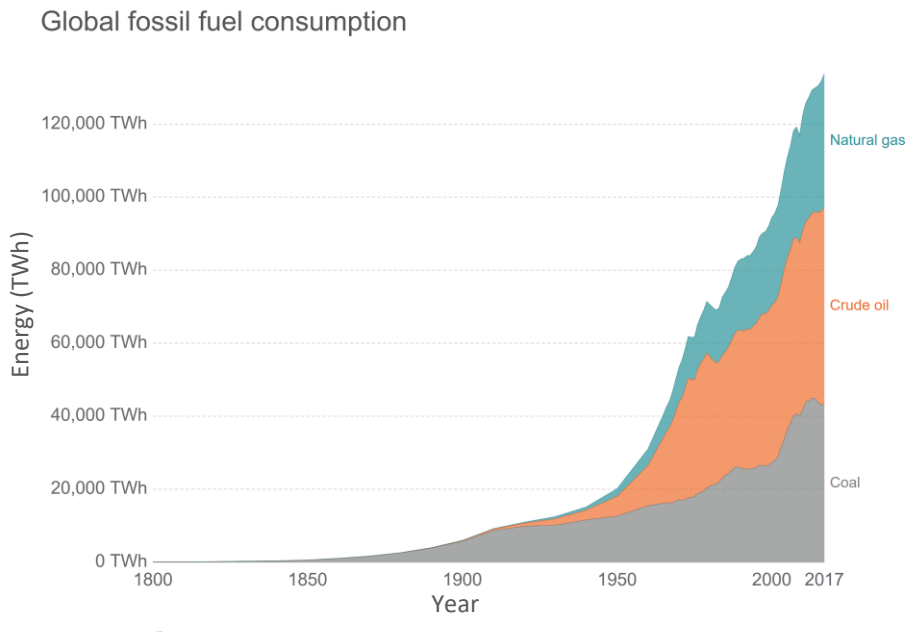

Figure 1.1: Energy consumption (measured in terawatt-hours (TWh)) of three types of coal, crude oil, and natural gas from the year 1800 to 2017. Each fossil fuel has seen an overall increase in usage during this time period. Adapted from ref. 3.

another ~46 years.[4] Even if these substances were inexhaustible, there are environmental consequences to burning them.

Since the beginning of the industrial revolution in about 1750, the concentration of CO_2 in the atmosphere has increased from ~277 to 405 parts per million (ppm) in 2017, with almost 100 ppm of that increase occurring within the last 50 years.[5] This concentration increase is likely due to humans' accelerated rate of burning fossil fuels, which produces CO_2 gas as a byproduct (Figure 1.2 (a) and (b)). As a greenhouse gas, CO_2 traps heat radiated by Earth. Carbon dioxide was the most emitted greenhouse gas in the United States in 2017, accounting for 82% of the total (methane was next highest at 10%). Thus, climate change and the increase in the average global temperature by 0.8 °C since 1880 can be attributed, at least in part, to the increase in CO_2 concentration in the atmosphere.[6] The two facts that 1) fossil fuels will eventually be depleted and 2) burning them causes an increase in CO_2 concentration in the atmosphere both necessitate research towards developing renewable energy alternatives to these world-shaping fuels.

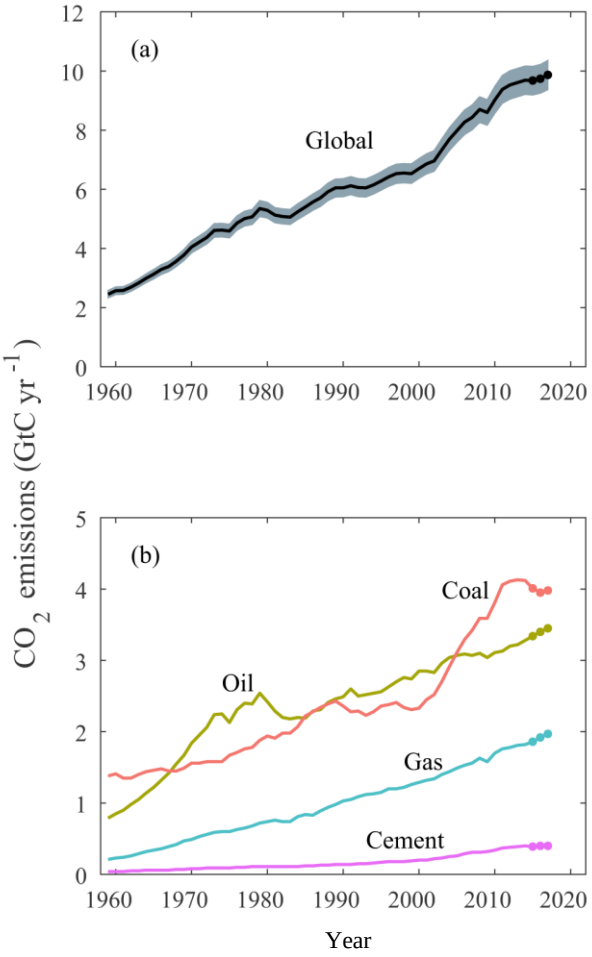

Figure 1.2: (a) The trend of increasing global CO_2 emissions (±5% uncertainty in grey outline). Black dots represent extrapolated values. (b) Contribution of fuel types to global overall CO_2 emissions. Emissions calculated in gigatons of carbon per year. Adapted from ref. 5.

To produce renewable energy is simply an act of converting the energy associated with a natural self-replenishing process in nature to some useful form of work.[7] An early example of harnessing such a process for energy is the

windmill. This machine converts wind energy into rotational energy, which can then be used to accomplish various tasks (milling grain or pumping water were common). While much more advanced, this same concept is taken advantage of today in the form of wind turbines that convert wind energy into electrical energy. Of the many different routes to renewable energy (i.e. wind, geothermal, hydropower, solar, biomass) the sun provides the most power *and* is the most abundant.

Accounting for cloud cover, a total of near 95,000 TW of power strikes the surface of earth in a year.[8] This is orders of magnitude greater than the amount of power consumed worldwide in 2016 (~19 TW).[9] A major drawback of solar energy is that sunlight is not energy dense. This diffuse nature means that capturing a useful amount of sunlight requires collection devices to be large. It is then crucial that the materials and manufacturing methods implemented to craft these devices are low-cost. The area of land required to house these devices will also need to be substantial. While progress is being made on overcoming these inconveniences, there is another issue associated with all forms of renewable energy that must also be addressed – energy storage.

1.2 Storing the Sun's Energy in Chemical Bonds – Water Splitting

When thinking about solar energy, one typically imagines solar panels that convert photons from the sun into electricity. If this electricity is not used immediately, however, it must be either stored or lost. Instead of having to use this energy at the time of generation, it would be convenient if the energy could be stored for later use on demand. One clever way of doing this is using sunlight to drive a reaction that forms a fuel. The sun's energy can then be thought of as stored in the chemical bonds of the synthesized fuel. One popular research area that achieves this is water splitting. Water splitting can be separated into two half-reactions – an oxidation and reduction. The oxidation half-reaction (reaction 1.2.1 below) has 2 moles of water being oxidized by 4

electrons to form 1 mole of oxygen gas while releasing 4 protons. These protons are then used in the reduction half-reaction (reaction 1.2.2 below) where 2 protons are reduced by 2 electrons to form hydrogen gas. The overall water splitting reaction (reaction 1.2.3 below) then, has 2 moles of water being converted to 2 moles of H_2 gas and 1 mole of O_2 gas.

$2\ H_2O_{(l)} \rightarrow O_{2(g)} + 4\ H^+ + 4\ e^-$	+1.23 V vs RHE	(1.2.1)
$2\ H^+ + 2\ e^- \rightarrow H_{2(g)}$	+0.00 V vs RHE	(1.2.2)
$2\ H_2O_{(l)} \rightarrow O_{2(g)} + 2\ H_{2(g)}$	+1.23 V vs RHE	(1.2.3)

Of the two products from this reaction, the hydrogen gas is valued as the fuel. Hydrogen gas can be burned in air, where the hydrogen reacts with oxygen gas in the atmosphere to yield water and energy ($\Delta G° = -237\ \text{kJ} \bullet \text{mol}^{-1}$).[10] The largest benefit from using hydrogen gas as a fuel is that the only emissions generated upon its burning are water vapor and warm air. While the feasibility of future widespread adoption of hydrogen as a fuel is debatable, its current most common use as a transportation fuel is in fuel cell electric vehicles, though the technology and supporting infrastructure are young.[11] Also, the hydrogen that *is* used for this purpose is almost exclusively produced by a process known as steam reforming, where steam and natural gas are mixed at high temperatures to make hydrogen gas as one of the reaction products. This is inconvenient because a fossil fuel is still being consumed to make the hydrogen gas. So why is water splitting not used instead? The reason is that water splitting requires a form of energy input to overcome the thermodynamic and kinetic barriers associated with this reaction (mostly due to the water oxidation half-reaction, discussed later) that is difficult to achieve with high selectivity. One way of fulfilling this energy requirement is through the use of a photocatalyst.

1.3 Metal Oxides as Heterogeneous Photocatalysts

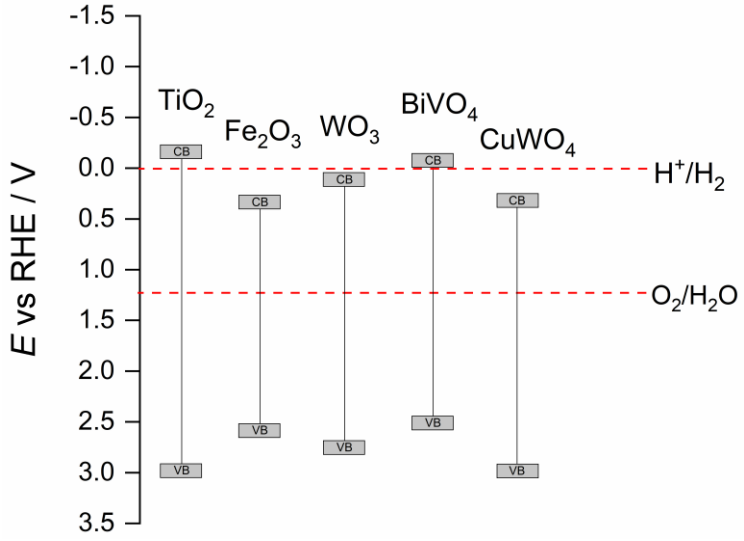

Figure 1.3: Valence bands (VB) and conduction bands (CB) for a series of metal oxide photocatalysts. The thermodynamic reduction potentials for protons to hydrogen gas and oxygen gas to water are indicated by red dotted lines. Potentials are versus the reversible hydrogen electrode (RHE) in volts (V).

Compounds containing at least one metal element and oxygen are known as metal oxides. A couple of well-known examples using the two most abundant transition metals are Fe_2O_3 (rust) and TiO_2 (used in sunscreen and paints).[12] An important feature of these materials with respect to photocatalysis is their band gap. The band gap is the energy difference between the top of the valence band where the highest energy electrons of the material are located (the analog for single molecules is the highest occupied molecular orbital) and the bottom of the conduction band, which is the next highest energy level available for electrons to populate (similar to the lowest unoccupied molecular orbital for single molecules). This energy difference dictates the maximum wavelength of light the material can absorb. Using the previously mentioned metal oxides as examples, anatase phase TiO_2 has a band gap of ~3.2 eV while Fe_2O_3 has one of ~2.1 eV (Figure 1.3).[13] The smaller band gap of Fe_2O_3 gives it the ability to absorb light into the green of the visible spectrum, down to about 590 nm, while the wider band gap of anatase TiO_2 limits the onset of absorption to ~387 nm, which is in the ultraviolet region of the electromagnetic spectrum. The minimum energy of light a metal oxide can absorb is important when considering the oxide for photocatalysis, but there are many more

factors to consider other than the band gap when deciding if a material is a suitable photocatalyst for a given reaction.

The energy values for the valence band maximum and conduction band minimum of a material are a couple of these other factors that help guide one towards an appropriate metal oxide for photocatalysis. When considering water splitting on a metal oxide particle, the energy value for the valence band maximum must be at least as positive as the reduction potential for the O_2/H_2O couple (i.e. 1.23 V vs. RHE). Likewise, the conduction band minimum must be at least as negative as the reduction potential for the H^+/H_2 couple (i.e. 0.00 V vs RHE). So, for example, all photogenerated holes in each of the metal oxides in Figure 3 would have energies at positive enough potentials to oxidize water if only thermodynamics was considered, but not all of those metal oxides would have photogenerated electrons with negative enough potentials to reduce protons. However, just because the energy values of the photocatalyst bands relative to redox couples of interest are met does not mean that a photocatalyst is guaranteed conduct those reactions if illuminated with light energetic enough to cause the generation of charge carriers. These band energy values represent minimum thermodynamic requirements for these half reactions; they are necessary prerequisites.

If the band energies of a metal oxide are positioned favorably for a given reaction, the rate will still be slow if the material cannot efficiency absorb photons to generate the charge carriers that carry out redox chemistry. The efficiency of light absorption is largely determined by the type of bandgap possessed by the solid – either a direct or indirect bandgap. A direct bandgap allows for a much more efficient and probable electronic transition of an electron from the valence band to the conduction band of the material.[14] The more efficient the material is at absorbing light, the more charge carriers that will be generated, and the faster the redox chemistry will be, all other

factors being equal. Bismuth vanadate ($BiVO_4$) is an example of a compound that has a fundamentally indirect band gap. While this band gap represents the lowest energy electronic transition in this compound, $BiVO_4$ also has another electronic transition very close (200 meV) in energy that is a direct transition.[15] The presence of this direct transition makes $BiVO_4$ one of the stronger light absorbers among metal oxides.

Charge transport through a material is also a property to consider when choosing a metal oxide photocatalyst. When light with equal or greater energy than the band gap is absorbed by a metal oxide, the photogenerated charge carriers (referred to as "excitons" before they are separated from each other) must have the capability to travel away from each other. If this separation does not happen, then the charges will recombine instead of carrying out photocatalysis. Some materials, such as Fe_2O_3, are notoriously poor at transporting charge[16]. This material has a valence band positive enough to conduct water oxidation and a relatively small bandgap, which are both attractive features for a water oxidation catalyst. However, holes in Fe_2O_3 have a low diffusion length (~10 nm), which leads to a high rate of charge recombination, resulting in a highly inefficient photocatalyst.[17]

There are a few methods that are used to decrease the amount of charge recombination. One is through nanostructuring of the material. Making particles smaller means the charges must travel a smaller distance before arriving at the particle surface where they can carry out photocatalysis. One can also use the fact that charge transport is not the same throughout all directions of the crystal structure of the solid. Making materials with preferential orientation for a particular crystal facet that charges travel faster through is beneficial to the rate of photocatalysis. For example, there have been many examples of synthesizing TiO_2 nanosheets with a preferential orientation for the (001) facet.[18–22] It is hypothesized that the attraction of charge carriers to the

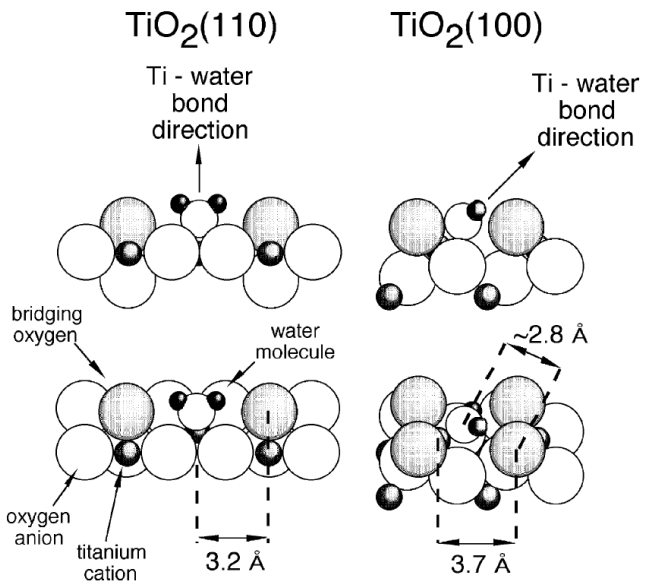

Figure 1.4: An example of different crystal faces of a metal oxide leading to different binding orientations of a substrate. Here, a distance of 3.2 Å between the water molecule on a rutile TiO_2(001) surface and the nearest bonded bridging oxygen atom is too great for there to be hydrogen bonding between the two. However, water on a rutile TiO_2(100) surface can hydrogen bond with the nearest bridging oxygen atom through a shorter distance of about 2.8 Å. Adapted from ref. 22 with permission from Elsevier.

different surface energies of different crystal facets leads to anisotropic charge mobility throughout a material.[23] Substrates may interact/bind more favorably/differently with a certain crystal facet over others, which is another reason preferentially oriented photocatalysts may have an improved rate of catalysis. For example, water binds in a different orientation on the rutile TiO_2(110) facet than it does on the TiO_2(100) facet (Figure 1.4).[24] Binding orientations such as this can influence catalysis.

An ideal photocatalyst must also possess photochemical stability. A benefit of metal oxides is that they are generally stable in nonaqueous photochemistry. When conducting catalysis in aqueous conditions the pH must be noted, as many metal oxides are unstable in either acidic or basic environments.[25] For example, Fe_2O_3 is perfectly stable under strongly basic conditions whereas WO_3 begins dissolving when used under even mild basic conditions. Some metal oxides like TiO_2 are stable under both acidic and basic conditions. The dependable stability of metal oxides is an attractive feature that the popular metal chalcogenide photocatalysts do not share. Metal chalcogenides such as CdS and CdSe typically absorb light more efficiently but lack photochemical stability.

Even if all the above discussed metal oxide properties would seem to suit photocatalysis, the kinetics of a reaction may not be favorable and can dramatically decrease the reaction rate or prevent the reaction from occurring altogether. This is true for water splitting, which is dramatically slowed by the water oxidation half-reaction. Metal oxides with valence band maxima more positive than the standard reduction potential for water to oxygen (i.e. +1.23 V vs RHE) can often not conduct this reaction at high rates due to the poor kinetics of the 4 proton coupled electron transfers involved in this reaction. A way around this problem is to conduct the catalysis photoelectrocatalytically.

1.4 Photoelectrocatalysis on Metal Oxide Electrodes

It is often the case that a metal oxide will have either its valence band maximum or conduction band minimum at an energy that, thermodynamically, one would expect it to catalyze a reaction of interest, but when the reaction is attempted photocatalytically on a powder it is limited by slow kinetics. It is possible to increase the rate of the reaction by anchoring the metal oxide to a conductive substrate (often fluorinated tin oxide or indium tin oxide glass) to be used as a photoelectrode. When attached to a potentiostat, an external potential can be applied to the metal oxide electrode that can increase reaction rates. To better understand how an applied bias influences catalysis, it is best to first understand the electronic structure of a metal oxide.

Their electronic structures are what make metal oxides such viable materials for photoelectrocatalysis. In the previous section, the electronic transitions that occur between the valence and conduction bands of metal oxides upon illumination, as well as the importance of the energy positions of these bands, was discussed. However, there is much more complexity when considering these electronic states and how they interact with a solution in the dark and under illumination. During their synthesis, it is common for metal oxides to take on oxygen vacancies in

their structures. Since each oxygen accounts for a 2– charge in the material, any lack of those means the material would have a net positive charge if nothing were done to balance the lack of negative charge. The way the material compensates for this is to have reduced metal centers. These reduced metal centers act as electron donors to the material, adding what are known as donor states, which are slightly more positive than electronic states at the conduction band minimum. Because these states are so close in energy to the conduction band minimum, these electrons are easily thermally excited into the conduction band, leaving behind positive holes in the donor states. However, because of their small number, these donor states are isolated. So while the donated electrons easily populate the conduction band and are allowed to move relatively freely throughout the material, the holes left behind in the isolated donor states remain on the metal site and do not move. This results in an increased concentration of conductive electrons in the conduction band but an unchanged concentration of conductive holes in the valence band. Because the conduction band has an increased concentration of conductive electrons relative to a metal oxide with no oxygen vacancies or other defects (where there is an equilibrium of an equal concentration of conductive electrons and holes), electrons are said to be the majority charge carriers and holes the minority charge carriers. Materials that have electrons as their majority charge carriers are called n-type semiconductors (where the "n" stands for negative, the charge on the electron).

This excess of conductive electrons in the conduction band has consequences on the Fermi level of the material as well. The Fermi level is the energy level that has a 50% chance of containing an electron.[26] For a semiconductor with equal concentrations of mobile valence band holes and conduction band electrons, the Fermi level is in the center of the band gap. However, n-type semiconductors such as metal oxides have their Fermi levels closer to the conduction band minimum due to the presence of donor states. This movement of the Fermi level towards more

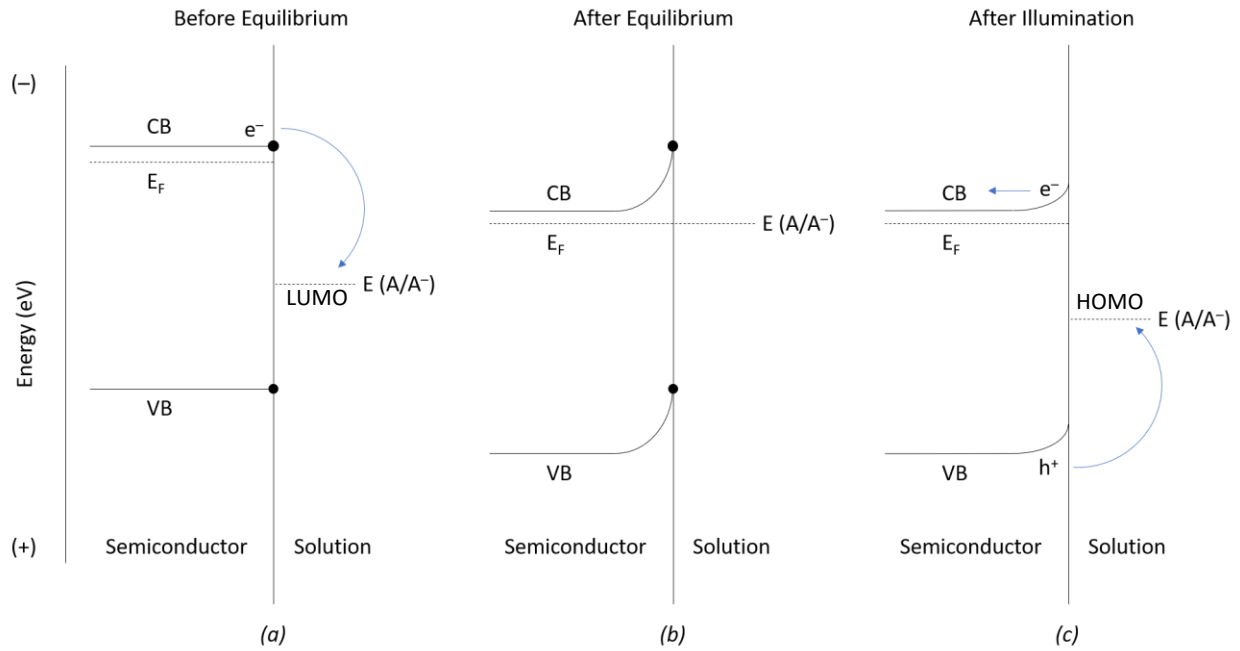

Figure 1.5: Bands of an n-type semiconductor in contact with a solution containing a redox couple A/A^- with a reduction potential of E. (a) The semiconductor immediately after contact with the solution. The equilibrium of the semiconductor Fermi level (E_F) with E of the redox couple has not had time to occur. The valence band (VB) and conduction band (CB) of the semiconductor have an equal energy in the bulk and near the material surface. The blue arrow represents electrons beginning to travel from the conduction band into solution upon contact of the semiconductor with solution. (b) Bands of a semiconductor in contact with solution after equilibrium between E_F of the semiconductor and E of A/A^- has occurred. The bulk energy values of the bands are more positive than before equilibrium and bend upward as they approach the semiconductor surface. The energy values of the bands at the surface are identical to those before equilibrium was established. (c) Bands of a semiconductor electrode in contact with solution after illumination by a light source with energy greater than or equal to the band gap of the semiconductor. The height of the energy barrier created by band bending decreases and the energy values of the bands at the surface are more positive than those in cases (a) or (b). Because there is no longer equilibrium between the E_F of the semiconductor and E of A/A^-, holes from the valence band (which now have a much higher concentration after illumination) transfer from the semiconductor to A/A^-. A positive bias applied to the semiconductor electrode by a potentiostat causes electrons to travel through the bulk of the material, eventually leaving the semiconductor by traveling through an electrical contact and to the potentiostat.

negative potentials has consequences towards what type of catalysis is possible on n-type semiconductors.

While the energy of the conduction band minimum and valence band maximum are the same throughout a metal oxide before contact with a solution, a change in energy of the bands close to the surface of the metal oxide occurs when the metal oxide is brought into contact with a solution (Figure 1.5a and 1.5b). This is referred to as band bending, and it occurs due to the electrostatic equilibrium that must be established between the Fermi level of the metal oxide and a redox couple (A/A^-) in solution. When the lowest unoccupied molecular orbital (LUMO) of a species in solution is more positive in energy than the Fermi level of the metal oxide, electrons

from the conduction band of the metal oxide will be donated to this LUMO until the energy of the metal oxide Fermi level and average energy of the LUMO of the species redox couple are equal. The electrons that left the conduction band leave behind positive charges in a width of the semiconductor close to its surface. This width (typically 10-1000 nm) that is positively charged, called the depletion layer (or space-charge region), bends to more positive energy values.[27] The energy of the conduction band at the surface of the metal oxide remains the same as it was before contact with the solution. Now it is possible to see the consequence this has on catalysis. The band bending creates an energy barrier between conduction band electrons and the solution. This makes it much more difficult for n-type metal oxides to carrier out reduction reactions. However, the bending of the valence band (in the same direction as the conduction band) favors transport of holes from the valence band to solution, which is why n-type materials are favored for oxidation reactions. The bands of p-type materials bend in the opposite direction compared to n-type materials, and so are suited for reduction reactions. This thesis focuses solely on oxidation reactions, and so only utilizes n-type materials in the work.

This electronics picture of the metal oxide electrode / solution interface is drastically affected upon absorption of photons by the metal oxide (Figure 1.5c). The electrons promoted to the conduction band in the depletion layer of the material negate some of the positive charge associated with this region that accumulated when electrons were donated into the solution during electrostatic equilibrium that occurred when the metal oxide was brought into contact with the solution. This injection of electrons into the depletion layer diminishes the strength of the electric field (caused by the contact of the positive depletion layer and the negatively charged solution) felt by the depletion layer. The result is decreased band bending and a movement of the surface band energies to more positive values compared to the electrodes in the dark. However, there still

exists a barrier to electrons and a driving force for holes to transfer to solution. While illumination does promote electrons to the conduction band, the concentration change of electrons is negligible compared to their concentration before illumination, which is high due to the reduced metal states acting as electrons donors. This is not true for holes; their concentration relative to the pre-illuminated metal oxide increases substantially. This increase in hole concentration paired with a driving force in the depletion layer to transfer holes to solution results in the solution redox couple donating electrons to the valence band of the metal oxide. This causes a movement of the average electron energy in the redox couple to move to more positive values as it undergoes continuous oxidation reactions. As the holes in the valence band are reacting with the solution redox couple, the conduction band electrons are moved out of the semiconductor through an external circuit and into the potentiostat, where they are ultimately transferred to another electrode (the counter electrode) to do a reduction reaction. The oxidation of the solution species can occur at potentials (generated by the potentiostat) that are more negative than the thermodynamic potential required for this reaction. While this could not happen on an electrode in the dark, it is possible on an illuminated metal oxide due to the built-in voltage between the energy of the holes and the energy of the redox couple that occurs when the hole population increases upon illumination. This is why metal oxides are able to act as photoelectrocatalysts for oxidation reactions.

1.5 Selectivity of Photoelectrocatalytic Water Oxidation on Metal Oxide Photoanodes

Water oxidation is the half-reaction of water splitting that is rate-limiting. Because n-type semiconductors are good candidates for photoelectrocatalytic oxidation reactions, there has been a large effort to utilize metal oxides as water oxidation photoelectrocatalysts.[28–32] As discussed in the previous section, when illuminated, the holes in a metal oxide valence band have a driving force to oxidize a substrate in solution if the thermodynamic redox couple of this substrate is more

negative in energy than the valence band maximum. This is the scenario for metal oxides and the H_2O/O_2 redox couple. The potential required to oxidize water into O_2 is 1.23 V vs. RHE. The majority of metal oxides have their valence bands composed mostly of low-lying O(2p) orbitals, which are typically always more positive than +2.5 V vs. RHE (Figure 1.3). This energy surpasses the thermodynamic potential required to oxidize water by over a volt, making valence band holes of metal oxides much more oxidizing than necessary to thermodynamically carry out water oxidation. So oxidizing, in fact, that some metal oxides, like TiO_2, have been used as organic pollutant degradation catalysts.[33] The highly oxidizing valence band holes have the capability to oxidize organic pollutants completely to CO_2 gas. While this strong oxidizing power gives these compounds the ability to oxidize water (thermodynamically-speaking), it also gives them the ability to oxidize other components of the solution.

An important metric for any catalyst is how selective it is for a desired process. For photoelectrocatalysts, this is known as the Faradaic efficiency (Equation 1.5.1)

$$Faradaic\ efficiency = \frac{n \times N \times F}{Q} \tag{1.5.1}$$

where n is the number of electrons required for the process ($n = 4$ for water oxidation), N represents the moles of product detected after catalysis has been stopped, F is the Faraday constant (i.e. 96,485.3365 Coulombs of charge / mol of electrons), and Q is the total charge passed during the experiment. While base-stable metal oxides such as Fe_2O_3 and TiO_2 have high Faradaic efficiencies reported for water oxidation under basic conditions, high efficiencies are not always the case. For example, Faradaic efficiencies for the acid stable catalyst WO_3 are reported to be low in acidic or neutral conditions.[34] Some suggested causes for this low Faradaic efficiency have been electrolyte anion oxidation[34,35] and incomplete oxidation of water to peroxide species, the latter

being invoked as the cause of current degradation of WO_3 during electrolysis.[36–38] Our lab has reported that all current degradation of WO_3 during electrolysis can be attributed to deintercalation of protons in the synthesized WO_3 during electrolysis, which casts doubt on the claims of peroxide generation.[39] However, the evidence for electrolyte oxidation is strong. While many of these electrolyte oxidation reactions are thermodynamically more difficult than water oxidation (i.e. their redox couples are more positive than the H_2O/O_2 couple), they are kinetically easier to achieve, resulting in them competing with water for the valence band holes of WO_3. These side reactions may proceed through either direct anion oxidation on the metal oxide surface, or through indirect anion oxidation where water is first oxidized on the metal oxide to hydroxyl radical that then goes on to oxidize the electrolyte anion before it can be further oxidized to oxygen gas. It may be possible to greatly increase the Faradaic efficiency of WO_3 through suppression of these side reactions. These suppression methods would be valuable not only for WO_3, but potentially other metal oxides suffering from sub-unity Faradaic efficiencies for water oxidation.

1.6 Substituting Water Oxidation with Biomass-Derived Compound Oxidation

While water splitting uses an abundant starting material (water) to generate a renewable energy source (hydrogen gas), there are certainly drawbacks to water splitting. These issues mostly stem from the water oxidation half-reaction. Water oxidation is notorious for having poor kinetics, while proton reduction is kinetically facile.[40] This is the foremost issue with water oxidation. The poor water oxidation kinetics arise from the requirement of a total of four proton-coupled electron transfer (PCET) reactions that must occur to oxidize water to O_2. The many elementary reactions necessary to complete this process tax the reaction rate considerably. Proton reduction, on the other hand, does not suffer from a cumbersome number of steps, as it only requires two electrons and two protons. This makes the overall reaction rate of water splitting depend solely on the rate of

water oxidation. Not only is water oxidation slow, but its product, O_2, is not economically valuable. While H_2 has no natural deposits on Earth and is valued as a renewable fuel from water splitting, O_2 is already abundant in the Earth's atmosphere (~21% by volume, making it easy to sequester) and cannot be used as a fuel. Therefore, the generation of O_2 can be considered an inefficient use of solar energy input. Oxygen is also a gas, and in a one-compartment water splitting cell, will combine with the H_2 to make a dangerous H_2/O_2 mixture. These critiques of water oxidation lead one to consider other possible replacements for this half-reaction.

It would be convenient to substitute water oxidation with an alternative oxidation reaction while keeping proton reduction as the reduction half-reaction. This does mean that this replacement reaction would need to be proton-coupled, as protons need to be generated during the oxidation to get reduced to H_2. Organic substrates are a possible starting point for the oxidizable substrate, as one could imagine doing 2 PCET reactions to oxidize an amine or alcohol to an imine or aldehyde, respectively. There is also a list of other desirable characteristics of this alternative organic oxidation, summed up quite nicely by Yujie Sun:

"(i) the organic substrate should be soluble in aqueous media; (ii) the oxidized product should be nongaseous and more valuable than the starting compound; (iii) the oxidation potential of the organic substrate should be less positive than that of [water oxidation] (otherwise the Faradaic efficiency of the new oxidation reaction will be low); and (iv) the substrate and its oxidized product will not compete with [proton reduction] even though a two-compartment configuration would be preferably adopted"[41]

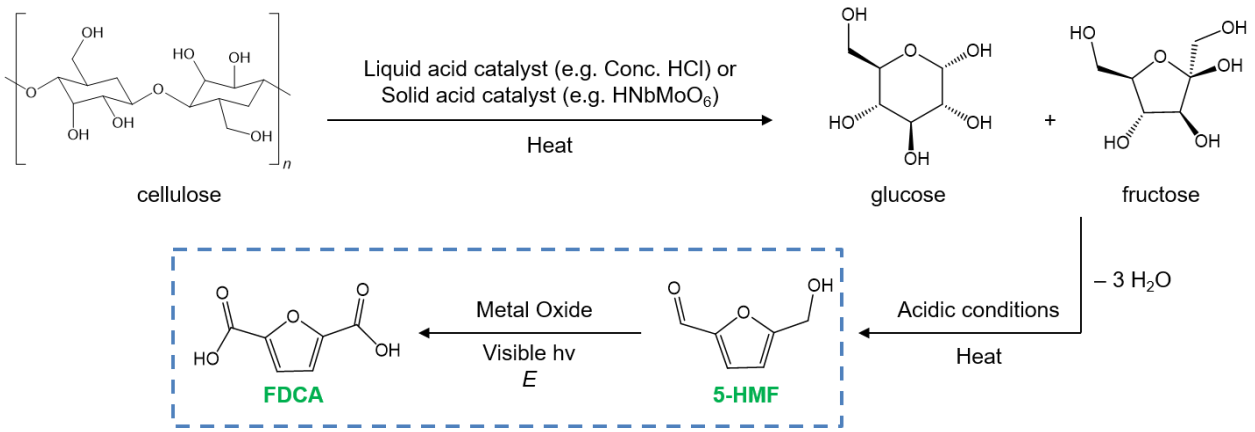

Figure 1.6: An example of a series of reactions taking cellulose (a component of raw biomass) to 2,5-furandicarboxylic acid (FDCA). The oxidation of 5-hydroxymethylfurfural (5-HMF) to FDCA (boxed in blue) would be an impactful substitution for water oxidation. The FDCA product has the capability to replace terephthalic acid in the synthesis of many useful plastics.

It should be noted that just because the potential of the redox couple for an organic substrate is more positive than that for water oxidation does not necessarily mean that water oxidation will compete for valence band holes. It is possible that the organic oxidation is so much more kinetically accessible than water oxidation that unity Faradaic efficiency could be achieved. So while it would certainly be preferable to have the organic redox couple more negative than that for water oxidation, it is not necessary. Another desirable quality of the replacement reaction would be if the starting organic substrate was from a renewable energy source, which can be realized by using biomass-derived compounds as the oxidizable compound.

While raw biomass, such as lignocellulose from plants, is much too structurally complex and chemically inert to use as a starting material, there are known processes that break down these more complex forms of biomass into more manageable compounds. For example, cellulose (the primary constituent of lignocelluloses) can be broken down to fructose and glucose with heat and a catalyst (Figure 1.6).[42] The catalysts are usually strong liquid acid catalysts, but solid acid catalysts have been used as well. The sugars can then undergo a triple dehydration reaction under acidic conditions and heat to yield a biomass-derived compound more fit for use as the starting material for an oxidation reaction, 5-hydroxymethyfurfural (5-HMF).[43] The oxidization of this

compound could then be conducted photoelectrocatalytically on a metal oxide catalyst to yield 2,5-furandicarboxylic acid (FDCA). This compound can replace terephthalic acid (currently made with petroleum-derived starting materials) as the monomer in many polyester, polyamide, and polyurethane syntheses.[41,44] Oxidizing 5-HMF instead of water fulfills both the (i) and (ii) desirable characteristics listed above – (i) 5-HMF is water-soluble and (ii) its product (FDCA) is a solid (also water-soluble) and is more valuable than the starting material due to its capability of acting as a monomer for widely used plastics. Though no standard redox potential has been reported for 5-HMF, point (iii) is supported by many examples of aqueous 5-HMF catalytic oxidation.[41,44–48] These examples that quantified H_2 production reported no interference of proton reduction by the oxidized alcohol, supporting point (iv).

1.7 Scope of this Thesis

This thesis is motivated by the idea that a transition away from photocatalytic water oxidation as the half-reaction involved in a H_2-generating redox process and towards a selective organic oxidation is beneficial. An organic oxidation has the potential to be faster than the water oxidation that hampers the rate of overall water splitting while generating a soluble oxidation product that is an economical upgrade from the starting compound. Water splitting, however, is a renewable and environmentally benign process – water is split into H_2 and O_2, the H_2 is then burned in the presence of O_2 to make water and release energy, arriving back at the begin of the cycle where it can be started again. Utilizing petroleum-derived compounds as the starting material for this oxidation would certainly be a drawback and a move away from sustainable catalysis. However, this can be avoided if a biomass-derived compound is used as the starting compound for this photocatalytic oxidation. The work herein is an effort towards this goal of replacing water

oxidation with a selective organic oxidation. Various metal oxide catalysts are investigated for this purpose due to their ability to absorb visible light and their robust photochemical stability.

Chapter 2 begins with a description of how the water oxidation chemistry on the surface of a WO_3 photoanode can be influenced by the photodeposition of a FeOOH layer. The shape of the Tafel plot of WO_3 is shown to be different than that for $WO_3 \mid FeOOH_{10,000s}$, and that the $WO_3 \mid FeOOH_{10,000s}$ material exhibits a greatly reduced Tafel slope compared to WO_3. Results are discussed that show how the quantity of hydroxyl generated during photoelectrocatalytic water oxidation changes with increasing FeOOH deposition time. These results then led to a series of experiments where selective oxidation of benzyl alcohol, a model compound for biomass-derived compounds, was attempted on oxyhydroxide-coated WO_3. Chapter 3 discusses a shift away from aqueous environments and alcohol organic substrates, moving towards acetonitrile solvent and benzylic amines as the substrates. This allows for isolation of the organic oxidation by removing solvent oxidation as a possibility. In an effort to move towards catalysts that absorb more of the visible spectrum while also continuing exploration of the capabilities of a catalyst used previously in the Bartlett lab for water oxidation, $CuWO_4$ was chosen as the photoanode for the photoelectrocatalytic amine oxidations described in this chapter, where the chemoselectivity of benzylamine and *N*-methylbenzylamine is investigated. Chapter 4 then moves away from photoelectrocatalytic reactions and into the photocatalytic reactions on metal oxide powders. Specifically, the rate and selectivity of photocatalytic benzylamine oxidation on $CuWO_4$ and $BiVO_4$ powders are described, as well as the recyclability of both of these metal oxides for this oxidation reaction. Chapter 5 gives a brief look at identifying differences in product distribution of the photocatalytic oxidation of 1-phenyl-1,2-ethanediol on different crystalline phases of TiO_2 in both aqueous and nonaqueous solvents, while also looking at some other various benzylic and

saturated alcohol photocatalytic oxidations on a variety of metal oxide photocatalysts. Finally, Chapter 6 closes the thesis with a summary of the conclusions of previous chapters preceding a brief discussion of reasonable next steps in this work.

1.8 References

[1] Fossil. https://www.energy.gov/science-innovation/energy-sources/fossil (accessed September 5, 2019).
[2] The Story of Fossil Fuels, Part 1: Coal. https://climatekids.nasa.gov/fossil-fuels-coal/ (accessed September 5, 2019).
[3] Ritchie, H. and Roser, M. Fossil Fuels. https://ourworldindata.org/fossil-fuels (accessed September 6, 2019).
[4] How long before we run out of fossil fuels? https://ourworldindata.org/how-long-before-we-run-out-of-fossil-fuels (accessed September 16, 2019).
[5] Le Quéré, C.; Andrew, R. M.; Friedlingstein, P.; Sitch, S.; Hauck, J.; Pongratz, J.; Pickers, P. A.; Korsbakken, J. I.; Peters, G. P.; Canadell, J. G.; Arneth, A.; Arora, V. K.; Barbero, L.; Bastos, A.; Bopp, L.; Chevallier, F.; Chini, L. P.; Ciais, P.; Doney, S. C.; Gkritzalis, T.; Goll, D. S.; Harris, I.; Haverd, V.; Hoffman, F. M.; Hoppema, M.; Houghton, R. A.; Hurtt, G.; Ilyina, T.; Jain, A. K.; Johannessen, T.; Jones, C. D.; Kato, E.; Keeling, R. F.; Goldewijk, K. K.; Landschützer, P.; Lefèvre, N.; Lienert, S.; Liu, Z.; Lombardozzi, D.; Metzl, N.; Munro, D. R.; Nabel, J. E. M. S.; Nakaoka, S.; Neill, C.; Olsen, A.; Ono, T.; Patra, P.; Peregon, A.; Peters, W.; Peylin, P.; Pfeil, B.; Pierrot, D.; Poulter, B.; Rehder, G.; Resplandy, L.; Robertson, E.; Rocher, M.; Rödenbeck, C.; Schuster, U.; Schwinger, J.; Séférian, R.; Skjelvan, I.; Steinhoff, T.; Sutton, A.; Tans, P. P.; Tian, H.; Tilbrook, B.; Tubiello, F. N.; van der Laan-Luijkx, I. T.; van der Werf, G. R.; Viovy, N.; Walker, A. P.; Wiltshire, A. J.; Wright, R.; Zaehle, S.; and Zheng, B. Global Carbon Budget *Earth Syst. Sci. Data* **2018**, *10*, 2141–2194.
[6] Earth Observatory. https://earthobservatory.nasa.gov/world-of-change/DecadalTemp (accessed September 6, 2019).
[7] Renewable energy explained. https://www.eia.gov/energyexplained/renewable-sources/ (accessed September 5, 2019).
[8] Wick, R. and Tilley, S. D. Photovoltaic and Photoelectrochemical Solar Energy Conversion with Cu_2O. *J. Phys. Chem. C* **2015**, *119*, 26243-26257.
[9] International Energy Statistics. https://www.eia.gov/beta/international/data/browser/ (accessed September 5, 2019).
[10] Standard Thermodynamic Properties of Chemical Substances. In *CRC Handbook of Chemistry and Physics*, 92nd Edition, Haynes, W. M. and Lide, D. R. Eds.; CRC Press: Boca, Raton, FL, 2011, 5-13.
[11] Hydrogen Basics. https://afdc.energy.gov/fuels/hydrogen_basics.html (accessed September 8, 2019).
[12] Hosono, H.; Hayashi, K.; Kamiya, T.; Atou, T. and Susaki, T. New functionalities in abundant element oxides: ubiquitous element strategy. *Sci. Technol. Adv. Mater.* **2011**, *12*, 034303.
[13] Grätzel, M. Photoelectrochemical cells. *Nature* **2001**, *414*, 338-344.
[14] West, A. R. Optical Properties: Luminescence and Lasers. *Solid State Chemistry and its Applications*, 2nd Edition; John Wiley & Sons, Ltd: United Kingdom, 2014; 486.
[15] Cooper, J. K.; Gul, S.; Toma, F. M.; Chen, L.; Liu, Y.-S.; Guo, J.; Ager, J. W.; Yano, J. and Sharp, I. D. Indirect Bandgap and Optical Properties of Monoclinic Bismuth Vanadate. *J. Phys. Chem. C* **2015**, *119*, 2969-2974.
[16] Chatman, S.; Zarzycki, P. and Rossi, K. M. Spontaneous Water Oxidation at Hematite (α-Fe_2O_3) Crystal Faces. *ACS Appl. Mater. Interfaces* **2015**, *7*, 1550-1559.
[17] Young, K. M. H.; Klahr, B. M.; Zandi, O. and Hamann, T. W. Photocatalytic water oxidation with hematite electrodes. *Catal. Sci. Technol.* **2013**, *3*, 1660-1671.
[18] Han, X.; Kuang, Q.; Jin, M.; Xie, Z. and Zheng, L. Synthesis of Titania Nanosheets with a High Percentage of Exposed (001) Facets and Related Photocatalytic Properties. *J. Am. Chem. Soc.* **2009**, *131*, 3152-3153.
[19] Yang, X. H.; Li, Z.; Liu, G.; Xing, J.; Sun, C.; Yang, H. G. and Li, C. Ultra-thin anatase TiO_2 nanosheets dominated with {001} facets: thickness-controlled synthesis, growth mechanism and water-splitting properties. *CrystEngComm* **2011**, *13*, 1378-1383.
[20] Yu, H.; Tian, B. and Zhang, J. Layerd TiO_2 Composed of Anatase Nanosheets with Exposed {001} Facets: Facile Synthesis and Enhanced Photocatalytic Activity. *Chem. Eur. J.* **2011**, *17*, 5499-5502.
[21] Ichimura, A. S.; Mack, B. M.; Usmani, S. M. and Mars, D. G. Direct Synthesis of Anatase Films with ~100% (001) Facets and [001] Preferred Orientation. *Chem. Mater.* **2012**, *24*, 2324-2329.

[22] Cheng, X.-L.; Hu, M.; Huang, R. and Jiang, J.-S. HF-Free Synthesis of Anatase TiO_2 Nanosheets with Largely Exposed and Clean {001} Facets and Their Enhanced Rate Performance As Anodes of Lithium-Ion Battery. *ACS Appl. Mater. Intefaces* **2014**, *6*, 19176-19183.

[23] Guan, L. and Chen, X. Photoexcited Charge Transport and Accumulation in Anatase TiO_2. *ACS Appl. Energy Mater.* **2018**, *1*, 4313-4320.

[24] Diebold, U. The surface science of titanium dioxide. *Sur. Sci. Rep.* **2003**, *48*¸53-229.

[25] Yang, L.; Yu, G.; Ai, X.; Yan, W.; Duan, H.; Chen, W.; Li, X.; Wang, T.; Zhang, C.; Huang, X.; Chen, J.-S. and Zou, X. Efficient oxygen evolution electrocatalysis in acid by a perovskite with face-sharing IrO_6 octahedral dimers. *Nat. Commun.* **2018**, *9*, 5236.

[26] Bard, A. J. and Faulkner, L. R. Photoelectrochemistry and Electrogenerated Chemiluminescence. *Electrochemical Methods – Fundamentals and Applications*, 2nd Edition; John Wiley & Sons, Ltd; United Kingdom, 2001; 749.

[27] Rajeshwar, K. The Depletion Layer. *Fundamentals of Semiconductor Electrochemistry and Photoelectrochemistry*. Wiley-VCH Verlag GmbH & Co. KGaA; published online December 15th, 2007; 10.

[28] Zhu, T.; Chong, M. N.; Chan, E. S. Nanostructured Tungsten Trioxide Thin Films Synthesized for Photoelectrocatalytic Water Oxidation: A Review. *ChemSusChem* **2014**, *7*, 2974-2997.

[29] Hunter, B. M.; Gray, H. B. and Müller, A. M. Earth-Abundant Heterogeneous Water Oxidation Catalysts. *Chem. Rev.* **2016**, *116*, 14120-14136.

[30] Ding, C.; Shi, J.; Wang, Z. and Li, C. Photoelectrocatalytic Water Splitting: Significance of Cocatalysts, Electrolyte, and Interfaces. *ACS Catal.* **2017**, *7*, 675-688.

[31] Roger, I.; Shipman, M. A. and Symes, M. D. Earth-abundant catalysts for electrochemical and photoelectrochemical water splitting. *Nature Reviews Chemistry* **2017**, *1*, Article number: 0003.

[32] Yang, Y.; Niu, S.; Han, D.; Liu, T.; Wang, G. and Li, Y. Progress in Developing Metal Oxide Nanomaterials for Photoelectrochemical Water Splitting. *Adv. Energy Mater.* **2017**, *7*, 1700555.

[33] Peleyeju, M. G. and Arotiba, O. A. Recent trend in visible-light photoelectrocatalytic systems for degradation of organic contaminants in water/wastewater. *Environ. Sci.: Water Res. Technol.* **2018**, *4*, 1389-1411.

[34] Mi, Q.; Zhanaidarova, A.; Brunschwig, B. S.; Gray, H. B. and Lewis, N. S. A quantitative assessment of the competition between water and anion oxidation at WO_3 photoanodes in acid aqueous electrolytes. *Energy Environ. Sci.* **2012**, *5*, 5694-5700.

[35] Mi, Q.; Coridan, R. H.; Brunschwig, B. S.; Gray, H. B. and Lewis, N. S. Photoelectrochemical oxidation of anions by WO_3 in aqueous and nonaqueous electrolytes. *Energy Environ. Sci.* **2013**, *6*, 2646-2653.

[36] Seabold, J. A. and Choi, K.-S. Effect of Cobalt-Based Oxygen Evolution Catalyst on the Stability and the Selectivity of Photo-Oxidation Reactions on a WO_3 Photoanode. *Chem. Mater.* **2011**, *23*, 1105-1112.

[37] Hill, J. C. and Choi, K.-S. Effect of Electrolytes on the Selectivity and Stability of n-type WO_3 Photoelectrodes for Use in Solar Water Oxidation. *J. Phys. Chem. C* **2012**, *116*, 7612-7620.

[38] Huang, J.; Zhang, Y. and Ding, Y. Rationally Designed/Constructed CoO_x/WO_3 Anode for Efficient Photoelectrochemical Water Oxidation. *ACS Catal.* **2017**, *7*, 1841-1845.

[39] Breuhaus-Alvarez, A. G.; DiMeglio, J. L.; Cooper, J. J.; Lhermitte, C. R. and Bartlett, B. M. Kinetics and Faradaic Efficiency of Oxygen Evolution on Reduced H_xWO_3 Photoelectrodes. *J. Phys. Chem. C* **2019**, *123*, 1142-1150.

[40] Matheu, R.; Garrido-Barros, P.; Gil-Sepulcre, M.; Ertem, M. Z.; Sala, X.; Gimbert-Suriñach, C. and Llobet, A. The development of molecular water oxidation catalysts. *Nat. Rev. Chem.* **2019**, *3*, 331-341.

[41] You, B.; Liu, X.; Jiang, N. and Sun, Y. A General Strategy for Decoupled Hydrogen Production from Water Splitting by Integrating Oxidative Biomass Valorization. *J. Am. Chem. Soc.* **2016**, *138*, 13639-13646.

[42] Huang, Y.-B. and Fu, Y. Hydrolysis of cellulose to glucose by solid acid catalysts. *Green Chem.* **2013**, *15*, 1095-1111.

[43] Galaverna, R.; Breitkreitz, M. C. and Pastre, J. C. Converstion of D-Fructose to 5-(Hydroxymethyl)furfural: Evaluating Batch and Continuous Flow Conditions by Design of Experiments and In-Line FTIR Monitoring. *ACS Sustainable Chem. Eng.* **2018**, *6*, 4220-4230.

[44] Taitt, B. J.; Nam, D.-H. and Choi, K.-S. A Comparative Study of Nickel, Cobalt, and Iron Oxyhydroxide Anodes for the Electrochemical Oxidation of 5-Hydroxymethylfurfural to 2,5-Furandicarboxylic Acid. *ACS Catal.* **2019**, *9*, 660-670.

[45] Cha, H. G. and Choi, K.-S. Combined biomass valorization and hydrogen production in a photoelectrochemical cell. *Nature Chem.* **2015**, *7*, 328-333.

[46] Xu, S.; Zhou, P.; Zhang, Z.; Yang, C.; Zhang, B.; Deng, K.; Bottle, S. and Zhu, H. Selective Oxidation of 5-Hydroxymethylfurfural to 2,5-Furandicarboxylic Acid Using O_2 and a Photocatalyst of Co-thioporphyrazine Bonded to g-C_3N_4. *J. Am. Chem. Soc.* **2017**, *139*, 14775-14782.

[47] Battula, V. R.; Jaryal, A. and Kailasam, K. Visible light-driven simultaneous H_2 production by water splitting couple with selective oxidation of HMF to DFF catalyzed by porous carbon nitride. *J. Mater. Chem. A* **2019**, *7*, 5643-5649.
[48] Hun, G.; Jin, Y.-H.; Burgess, R. A.; Dickenson, N. E.; Cao, X.-M. and Sun, Y. Visible-Light Driven Valorization of Biomass Intermediates Integrated with H_2 Production Catalyzed by Ultrathin Ni/CdS Nanosheets. *J. Am. Chem. Soc.* **2017**, *139*, 15584-15587.

Chapter 2 Hydroxyl Radical Suppression during Photoelectrocatalytic Water Oxidation on WO_3 │FeOOH and its Effects on Benzyl Alcohol Oxidation

2.1 Introduction

Hydrogen gas is a renewable energy source that has the potential to lessen the reliance of the global population on fossil fuels. When burned in air, hydrogen gas reacts with oxygen to form water with a release of energy. However, most hydrogen gas currently is produced through the steam reforming process, where natural gas (a fossil fuel) is reacted with steam at high temperatures to generate hydrogen gas as one of the products.[1] Splitting water into its elemental constituents – hydrogen and oxygen gas – is another reaction that yields hydrogen gas a product while also benefitting from have water – an environmentally friendly compound – as its starting material. While water splitting can be achieved through electrolysis, this requires a high potential (and correspondingly, a large energy input) to be applied to the electrochemical system to drive the reaction. The reason the potential required is so high is because the water oxidation half-reaction is kinetically difficult, with four proton-coupled-electron transfer steps required for the reaction to be complete. One way to reduce the potential required for this limiting reaction is through the use of heterogeneous photocatalysts.

Metal oxide semiconductor photocatalysts are often employed for this purpose due to their chemical robustness and their capability to absorb visible light. The energy of the absorbed light helps reduce the applied potential needed to catalyze a reaction. A metal oxide that is commonly used a photocatalyst or a component in photocatalytic systems is tungsten (VI) oxide (WO_3). This metal oxide is unique in its aqueous stability in that it is stable in acidic conditions, ones where

many metal oxides dissolve. This allows for the study of photoelectrocatalytic water oxidation at low pH values. While it is convenient that WO_3 opens up new conditions in which to study water oxidation, the metal oxide catalyst has propensity to be unselective in the oxidation reactions that occur on its surface (i.e. its Faradaic efficiency for water oxidation is less than 100%). This inefficiency is detrimental towards the rate of water oxidation catalysis since not all of the charge being passed is contributing to the desired reaction.

The less than unity Faradaic efficiency for photoelectrocatalytic (PEC) water oxidation on tungsten oxide (WO_3) in acidic aqueous electrolytes is attributed to anion oxidation pathways.[2] Our lab showed that utilizing a WO_3 | FeOOH electrode, made by depositing iron oxyhydroxide onto WO_3, resulted in a high Faradaic efficiency for PEC water oxidation of 95.9 ± 1.6% while improving current stability in 0.1 M pH=4 potassium phosphate buffer.[3] However, adding the FeOOH layer to the WO_3 halved the saturated photocurrent density of the electrode. One of the postulated reasons for this was that the FeOOH layer was preventing a phosphate (the electrolyte anion) oxidation pathway. This hypothesis is consistent with both the lower saturated photocurrent density and higher Faradaic efficiency observed during OER on WO_3 | FeOOH. It was thought that this side reaction on bare WO_3 was either the direct oxidation of phosphate with valence band holes or the indirect oxidation by photogenerated hydroxyl radical (•OH) that reacted with H_2PO^{4-}, HPO_4^{2-}, or PO_4^{3-} to form $P_2O_8^{4-}$ or PO_5^{3-}. In this work, it is shown with a series of radical trap experiments that the hydroxyl radical concentration is indeed suppressed during photoelectrocatalytic water oxidation as a function of FeOOH deposition time on WO_3 | FeOOH electrodes.

The valence band maximum for WO_3 is 3.0 eV vs. NHE, which is more positive than the 2.7 V vs NHE required to oxidize H_2O to •OH.[2,4] Photogenerated holes in WO_3 are therefore

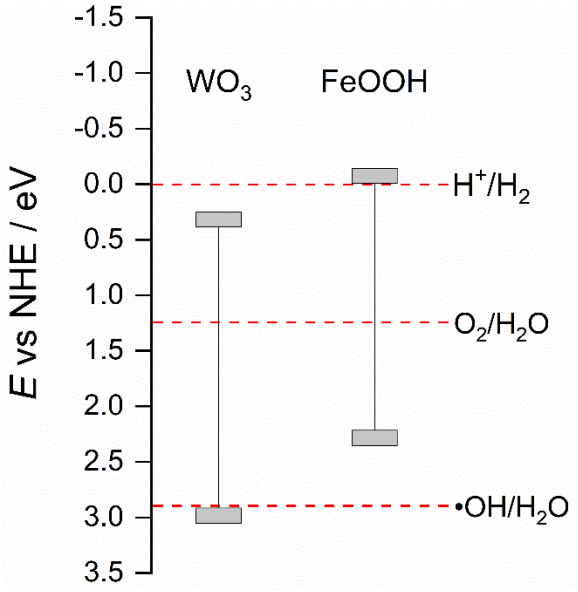

Figure 2.1: Approximate valence and conduction band positions for WO_3 and FeOOH with the redox couples for proton reduction, water oxidation, and hydroxyl radical generation from water.

oxidizing enough to produce •OH from water. Once generated, the highly oxidizing •OH can then go onto make oxygen gas or react with electrolyte anions. The anion oxidation pathway decreases the Faradaic efficiency for water oxidation. One approach of terminating this parasitic reaction is to lower the oxidizing power of the photogenerated holes in WO_3 to values more negative than the potential for hydroxyl radical generation from water. This was achieved in this work by depositing a layer of amorphous FeOOH, which has a valence band maximum of 2.11 eV vs. NHE, onto the surface of WO_3.[5] The holes of an illuminated WO_3 | FeOOH electrode must migrate from the WO_3 to the FeOOH before arriving at the electrode / electrolyte interface where they are now too not sufficiently oxidizing to produce hydroxyl radical from water (Figure 2.1).

2.2 Synthesis and Characterization of WO_3 and WO_3 | FeOOH Photoelectrodes

To synthesize the WO_3 electrodes, a spin-coating method was used. Briefly, a 1:1 H_2O:ethanol solution that was 0.5 M in tungsten from ammonium metatungstate was pipetted onto fluorinated tin oxide (FTO) conductive glass slides (1 x 1.3 cm) and spun at 2500 rpm for 30 seconds. The film was then annealed in an oven at 500 °C for 30 minutes. This spin-coat / anneal

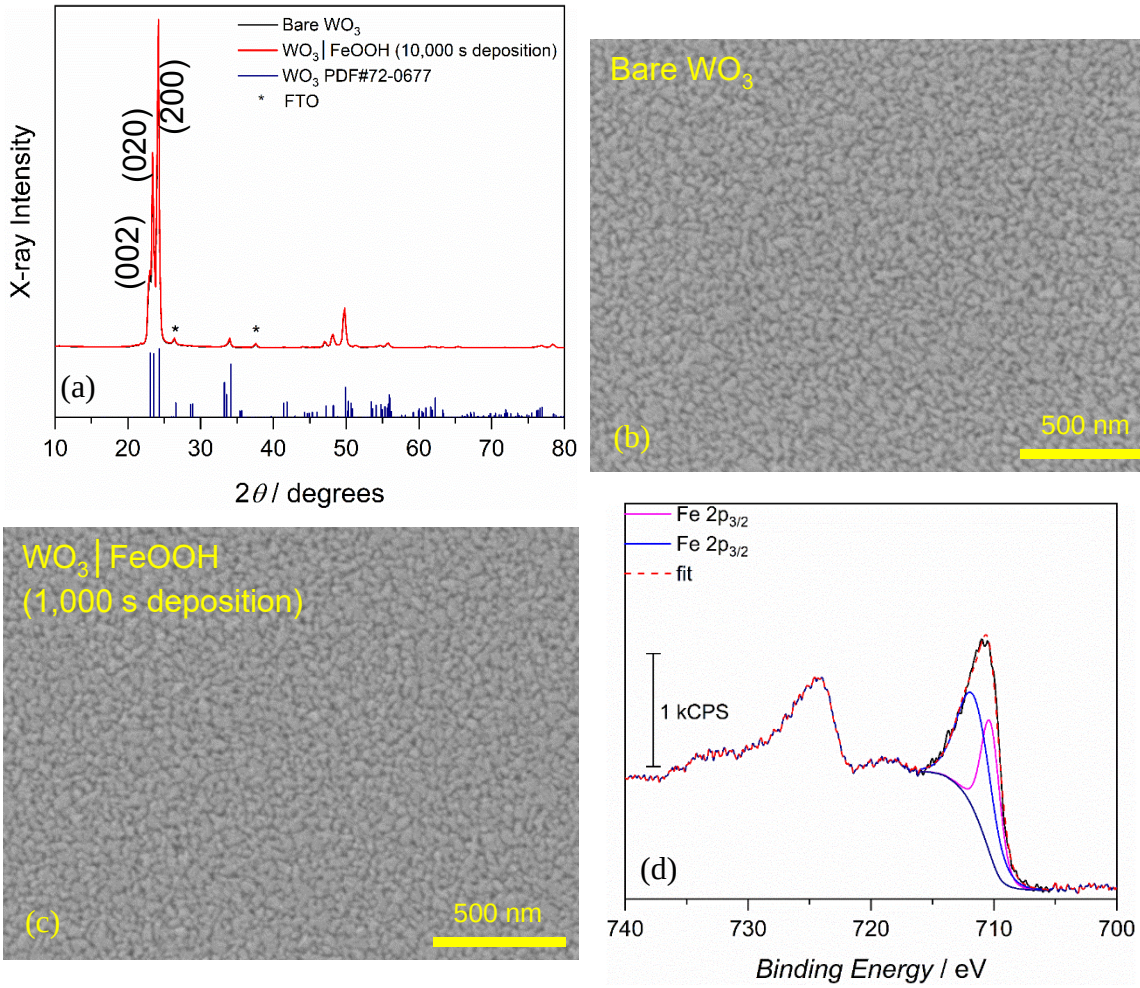

Figure 2.2: Powder X-ray diffractograms of bare WO_3 (black), WO_3 | FeOOH that had undergone an Fe deposition time of 10,000 s (red), a WO_3 reference pattern (navy, PDF#72-0677), and asterisks to represent peaks from the FTO substrate (a). Scanning electron micrographs of bare WO_3 and WO_3 | FeOOH that had undergone a 1,000 s Fe deposition, respectively ((b) and (c)). A fit X-ray photoelectron spectrum (black) of WO_3 | FeOOH that had undergone a 1,000 s Fe deposition with show contributions from two different Fe(III) $2p_{3/2}$ states (pink and blue) and calculated fit (red-dotted line) (d).

process was repeated to apply a total of 10 coats to the electrode. This procedure gave pure WO_3, shown to be crystalline by powder X-ray diffraction (Figure 2.2 (a)). The scanning electron micrographs showed a flat landscape of particles with no regularity in shape with their largest dimension ≤ 100 nm (Figure 2.2 (b)).

The addition of the FeOOH coat was done through photoelectrodeposition. A WO_3 electrode was submerged in an aqueous solution of sodium sulfate and iron sulfate. A constant current experiment was then run under 1 sun illumination for 100, 1,000 or 10,000 seconds with a

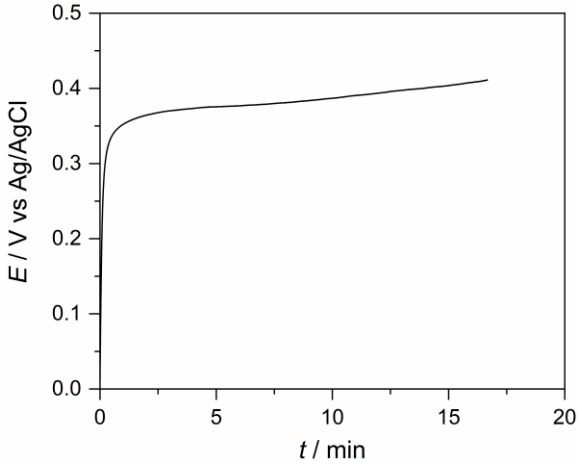

Figure 2.3: Chronopotentiometry experiment on a WO_3 working electrode in a solution of 0.1 M aqueous Na_2SO_4 and 10 mM $FeSO_4$ illuminated by 1 sun. Current passed during experiment was 58 μA • cm^{-2} for 1,000 s.

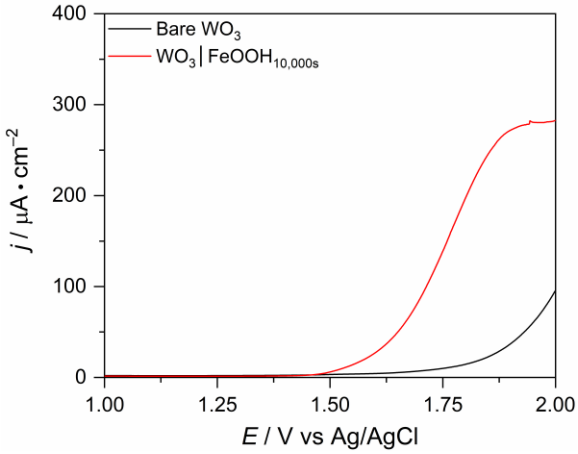

Figure 2.4: Dark linear sweep voltammograms of bare WO_3 (black) and $WO_3 \mid FeOOH_{10,000s}$ (red) in pH=4 0.1 M potassium phosphate buffer. The electrocatalytic capability of FeOOH for water oxidation is demonstrated by the cathodic shift in current onset.

current density of 58 μA • cm^{-2} (Figure 2.3). The iron on the surface could not be detected by XRD (Figure 2.2 (a)). The morphology of the film did not change upon Fe deposition, either (Figure 2.2 (c)). However, XPS showed the presence of iron (III) in the sample (Figure 2.2 (d)). The main peak in the XPS is at 710.8 keV, which is closer to Fe(III) values (e.g. 710.8 ± 0.2 eV for α-Fe_2O_3 and 711.4 ± 0.2 eV for α-FeOOH) than Fe(II) values (e.g. 709.5 ± 0.2 eV for FeO).[6] If any Fe(II) were present in the sample, shoulders would be observed at lower binding energies. However, this is not the case, suggesting that Fe(III) is the only oxidation state of Fe in the sample. While it is difficult to determine the compound responsible for the Fe(III) signal (e.g. FeOOH vs. Fe_2O_3), a dark linear sweep voltammogram of WO_3 compared to $WO_3 \mid FeOOH_{10,000s}$ shows that the Fe(III)-based compound deposited onto the WO_3 is an electrocatalyst for water oxidation given the cathodic shift in the onset of current after iron deposition (Figure 2.4). Since Fe_2O_3 is not an electrocatalyst for water oxidation, these data suggest that the deposited Fe(III)-based material is FeOOH.

2.3 Hydroxyl Radical Suppression on WO_3 | FeOOH during PEC Water Oxidation

To detect •OH during PEC water oxidation, 1 mM coumarin was added to the original 0.1 M potassium phosphate buffer (KP_i). Coumarin serves as a radical trap in these experiments, reacting with •OH to make 7-hydroxycoumarin as one of the reaction products (Figure 2.5). Coumarin has been shown to be an effective •OH trap in photocatalytic experiments on TiO_2 in aqueous solutions.[7] 7- hydroxycoumarin is highly fluorescent and can be identified by its strong emission peak at ~453 nm in pH=4 0.1 M KP_i. To confirm that depositing FeOOH onto WO_3

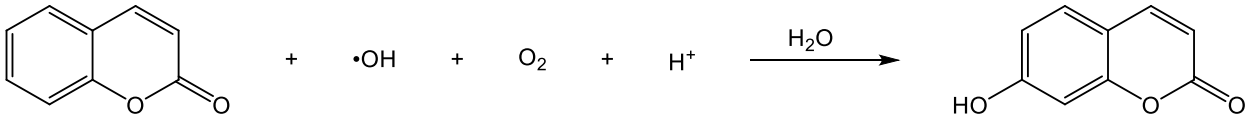

Figure 2.5: Reaction of coumarin with hydroxyl radical to yield 7-hydroxycoumarin, a highly fluorescent molecule. Coumarin was used as the hydroxyl radical trap in water oxidation experiments in this work.

decreases the •OH concentration during PEC water oxidation, extended bulk electrolysis was performed in the presence of 1 mM coumarin at 1.23 V vs RHE with WO_3 | FeOOH electrodes that had undergone different FeOOH deposition times prior to use (100, 1,000, and 10,000 s deposition times). After two Coulombs of charge had been passed during the electrolysis the reaction was stopped and the buffer solution was analyzed by fluorimetry. It was observed that the starting photocurrent density during electrolysis for each film dropped with increasing deposition time (Figure 2.6). This drop in photocurrent density was expected based on results reported from our lab previously, where the saturated photocurrent density dropped by a factor of two upon FeOOH deposition on WO_3.[3] The stability of photocurrent density over the course of the electrolysis increased with increasing deposition time. After the two Coulombs had been passed by each film, the photocurrent densities for the 0, 100, 1,000, and 10,000 s FeOOH depositions had decreased by 25, 20, 15, and 7% with respect to the photocurrent density observed one minutes into the deposition (to avoid photocurrent affect by charging current at the start of the electrolysis), respectfully. The quantity of •OH trapped by coumarin during electrolysis dropped as a function

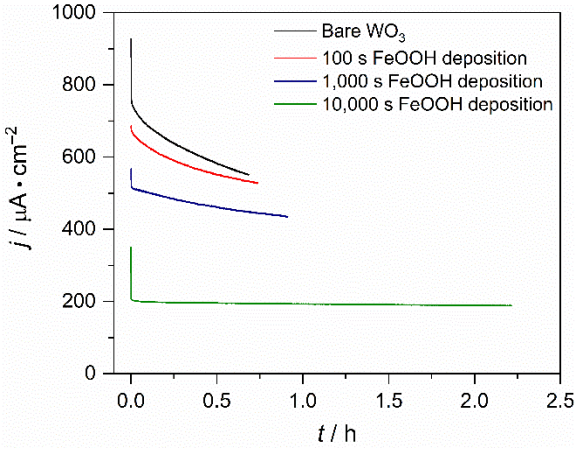

Figure 2.6: Bulk electrolysis photocurrent density traces on WO_3 | FeOOH films at 1.23 V vs RHE. Illuminated by 1 sun irradiation. Buffer = 0.1 M potassium phosphate at pH=4. 1 mM coumarin was included as a hydroxyl radical trap.

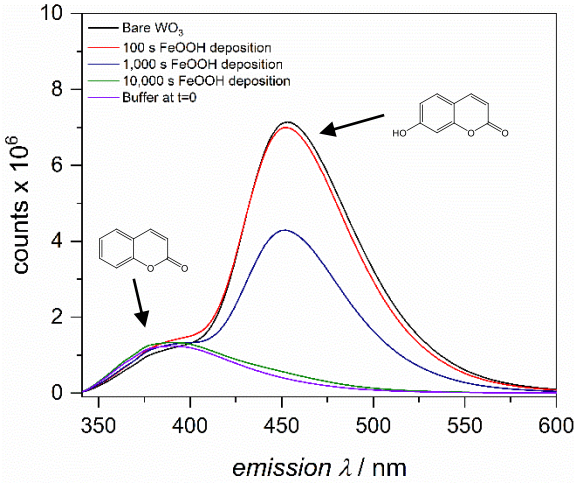

Figure 2.7: Fluorescence emission spectra of the reaction solution after two coulombs of charge had passed during PEC water oxidation on WO_3 | FeOOH films in 0.1 M potassium phosphate buffer at pH=4 with 1 mM coumarin included as a hydroxyl radical trap. The excitation wavelength was 332 nm. The peak at ~360 nm is emitted by the coumarin and the peak at ~453 nm is emitted by 7-hydroxycoumarin.

of increasing FeOOH deposition time (Figure 2.7). The 100 s FeOOH deposition time had little effect on the 7- hydroxycoumarin signal seen in the post-electrolysis solution compared to that observed for the reaction on bare WO_3 (Table 2.1). However, a deposition of 1,000 s significantly reduces the 7-hydroxycoumarin peak intensity, while a 10,000 s deposition results in almost no change in fluorescence when compared to the pre-electrolysis solution. This result is expected since the greater the FeOOH deposition time, the greater the coverage on the electrode. For a 104 s deposition 0.58 C of charged is passed, giving a maximum FeOOH coverage of 6.0 μmol • cm^{-2}.

2.4 Tafel Analysis of PEC Water Oxidation on WO_3 and WO_3 | FeOOH

The change in the quantity hydroxyl radical produced during photoelectrocatalytic water oxidation on WO_3 vs. WO_3 | $FeOOH_{10,000s}$ suggests that the mechanism of water oxidation is different on the surface of these two materials. Tafel analysis was conducted to further

Table 2.1: Effect of FeOOH deposition time on quantity of captured •OH during PEC water oxidation on WO_3 | FeOOH

FeOOH Deposition Time (s)	Decrease in 7-hydroxycoumarin peak intensity at 453 nm (%)
0	0
100	2
1,000	42
10,000	98

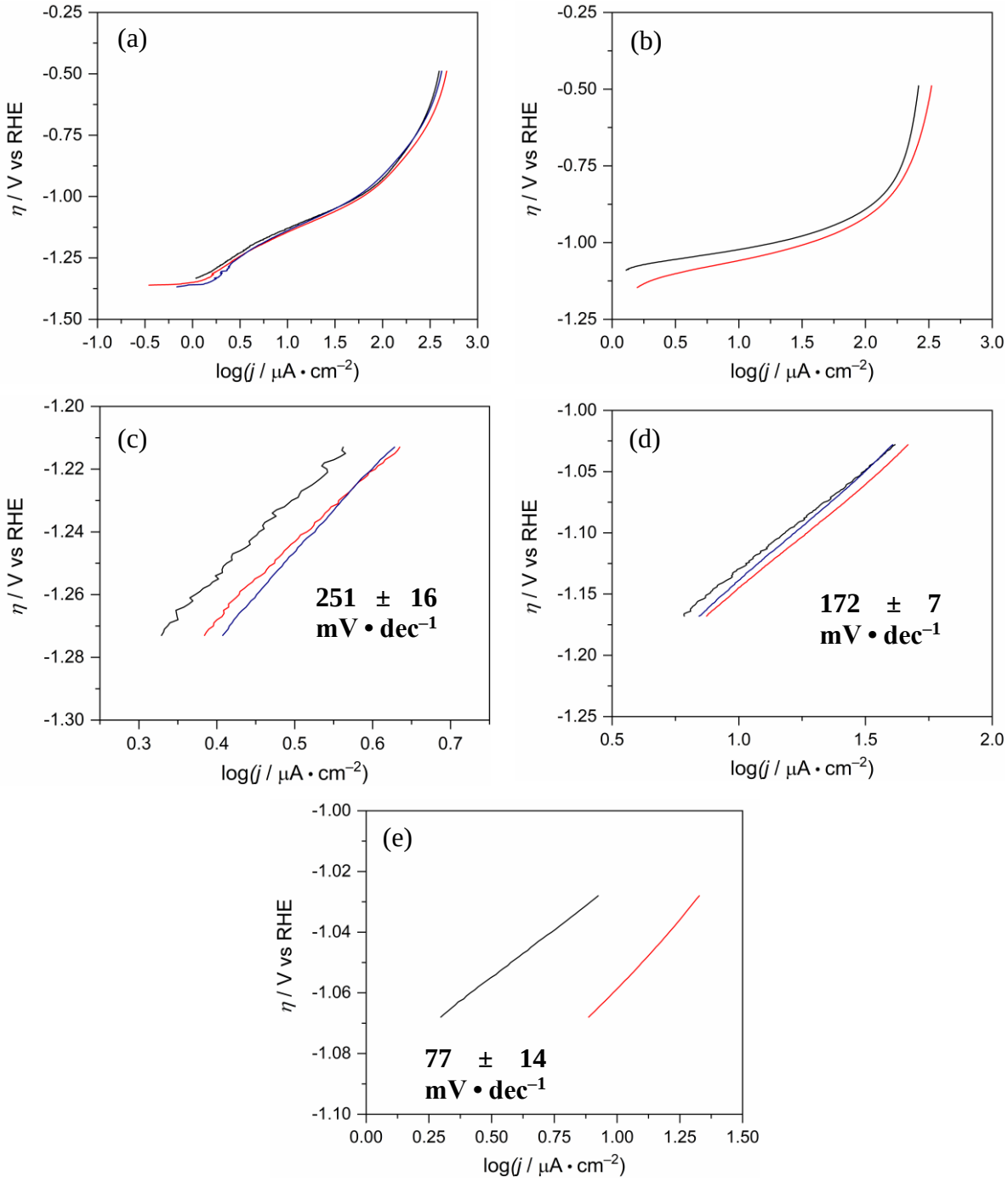

Figure 2.8: Full Tafel plots for (a) bare WO_3 (three trials) and (b) WO_3 | $FeOOH_{10,000s}$ (two trials). Linear Tafel regions for (c) WO_3 from an η of -1.273 to -1.213 V vs. RHE and (d) -1.168 to -1.028 V vs. RHE. Linear Tafel region for (e) WO_3 | $FeOOH_{10,000s}$ from an η of -1.068 to -1.028 V vs. RHE. All Tafel slopes are given as an average of the data shown and are taken from their respective Tafel plots (i.e. slopes in (c) and (d) are taken from (a) and slopes in (e) are taken from (b).

support this observation. Plotting the $\log_{10}$ of the current density vs. overpotential (η) of the reaction (any potential required to drive the reaction greater than the expected potential required

based on thermodynamics) provides a Tafel plot. In this case, η is any potential applied to the system beyond +1.23 V vs. NHE. Data collected for this type of analysis must not be diffusion limited (i.e. the concentration of the reactant at the electrode surface needs to be constant at all applied potentials). In this work, linear sweep voltammetry conducted at a slow scan rate (0.1 mV • cm^{-1}) was the method chosen to acquire this data. The slow scan rate allows for the reactant to constantly diffuse towards the surface faster than it is being depleted by the reaction. Keeping the concentration of reactant constant at the electrode surface is also greatly helped by the fact that the reactant in this case is solvent.

The slopes of the linear regions in Tafel plots provide an idea of how effective a material is at catalyzing a given reaction as well as information about the electron transfer involved in the rate determining step. The shallower the Tafel slope (measured in mV • dec^{-1}, where the dec stands for decade (order of magnitude) of current), the less overpotential required to change the measured current density by an order or magnitude. There are also common Tafel slopes that indicate which electron transfer in the process was rate determining. For example, a Tafel slope of 118 mV • dec^{-1} is suggestive that the first electron transfer of the reaction was rate determining, while a slope of 40 mV • dec^{-1} is indicative of the second electron transfer being rate determining. However, deviations from these predicted Tafel slopes can occur, as they do in this work, making inferences about the rate determining step from these data convoluted.

The shapes of the Tafel plots of WO_3 and $WO_3 \mid FeOOH_{10,000s}$ were different (Figure 2.8 (a) and (b)). That of WO_3 appeared to have two linear regions before diffusion-limited processes take over at higher overpotentials (Figure 2.8 (c) and (d)). However, $WO_3 \mid FeOOH_{10,000s}$ gave a Tafel plot with only one linear region (Figure 2.8 (e)). As a note of clarification, the η values listed on the y-axis of these plots are negative because of the photovoltage at the surface of the

illuminated catalyst. The potential of the photogenerated holes in the valence bands of these catalysts compared to the water oxidation redox couple allow this reaction to take place at potentials below the expected thermodynamic value for this reaction (i.e. 1.23 V vs NHE). This is discussed in detail in chapter 1.4 of this thesis. The first linear region in the WO_3 Tafel plot is smaller than the second and has a much greater slope, suggesting that the rate limited step of this first process is more difficult for WO_3 to catalyze than the second process, which has a smaller Tafel slope over a wider potential range. Neither of these slopes correspond to predicted (e.g. 118 $mV \bullet dec^{-1}$ suggesting the first electron transfer step is rate limiting) Tafel slopes that can be used to help suggest how many electrons transfers preceded the rate limiting step; they are too large. This is a common occurrence for Tafel slopes calculated from water oxidation on metal oxide catalysts, but the Tafel slope values are still valuable as a comparison of these materials' ability to catalyze water oxidation.[8] At 77 ± 14 $mV \bullet dec^{-1}$, the slope for the $WO_3 \mid FeOOH_{10,000s}$ material is much shallower than either observed for bare WO_3. This was expected, as FeOOH has been shown to be an electrocatalyst for water oxidation, which should allow the $WO_3 \mid FeOOH_{10,000s}$ material to more efficient conduct this reaction.[3,9–12] This Tafel slope indicates that the rate of water oxidation on $WO_3 \mid FeOOH_{10,000s}$ is more readily increased by an increase in the applied potential than it is for bare WO_3. However, the Tafel slope observed for $WO_3 \mid FeOOH_{10,000s}$, likes those for WO_3, does not correspond to any value that can shed light on the electron transfer involved in the rate limiting step.

2.5 Photoelectrocatalytic Aqueous Benzyl Alcohol Oxidation on WO_3, $WO_3 \mid FeOOH$, and $WO_3 \mid FeOOH \mid NiOOH$

After observing that FeOOH deposition suppressed •OH formation during water oxidation, it was thought that this •OH deficient environment may be an aqueous environment conducive to

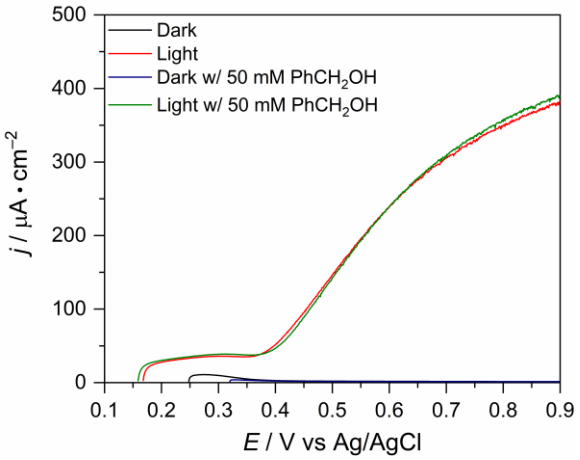

Figure 2.9: Linear sweep voltammograms of pH=4 0.1 M potassium phosphate electrolyte before (dark (black) and illuminated with 1 sun (red)) and after the addition of $PhCH_2OH$ (dark (navy) and illuminated with 1 sun (green)) using a $WO_3 \mid FeOOH_{10,000s}$ working electrode.

organic oxidations. Photocatalytic aqueous selective organic oxidations on metal oxides are typically difficult to achieve, as many metal oxide photocatalysts (including WO_3) have enough oxidizing powder to oxidize water to the highly oxidizing hydroxyl radical, which, in turn, will indiscriminately oxidize organics. While this reactivity can be useful in certain applications, such as organic degradation reactions driven by UV-light illuminated TiO_2 in water, it eliminates any possibility of selective chemistry. As has been demonstrated in this work, different than WO_3 and TiO_2, FeOOH, is incapable of forming hydroxyl radical from water due the location of the valence band being more negative than the redox potential of the hydroxyl radical / water couple. This opens up the possibility of selectivity oxidizing organic substrates with high efficiency. Such reactions would be convenient replacements for water oxidation during efforts to generate hydrogen gas from renewable resources, especially if the starting organic substrates were biomass-derived compounds.

The $WO_3 \mid FeOOH$ photoelectrocatalyst seemed like a reasonable starting point for investigating aqueous alcohol oxidations. Alcohol oxidation was chosen since most biomass-derived compounds are heavily hydroxylated, with the hydroxyl group generally being the most reactive site on those molecules. While benzyl alcohol is not a biomass-derived compound, it was used in this work as a model compound due to its similar functionality to 5-hydroxymethylfurfural, a compound whose oxidation is commonly employed to demonstrate a catalysts capability of oxidizing biomass-derived compounds.[13–19]

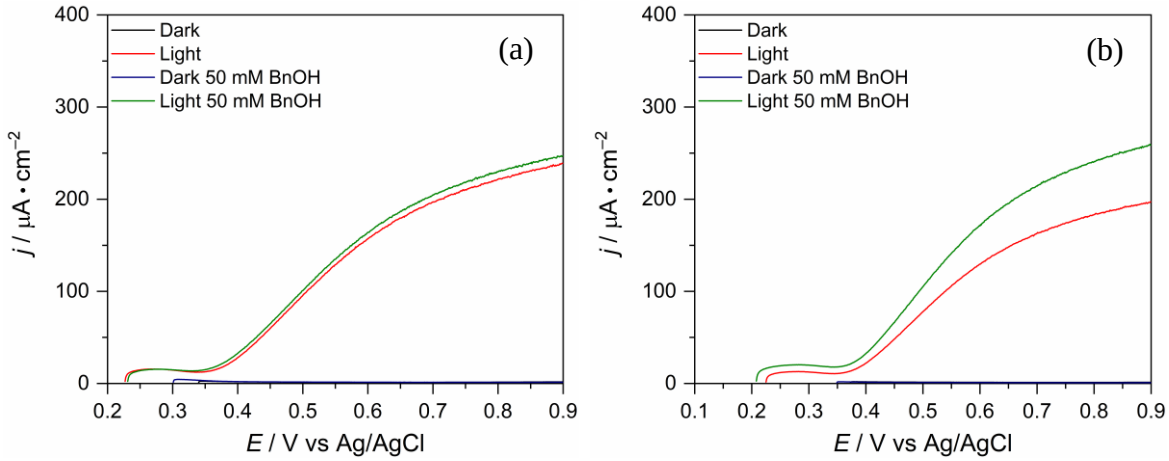

Figure 2.10: Linear sweep voltammograms of pH=4 0.1 M potassium phosphate electrolyte before (dark (black) and illuminated with 1 sun (red)) and after the addition of $PhCH_2OH$ (dark (navy) and illuminated with 1 sun (green)) using a $WO_3 \mid FeOOH_{10,000s} \mid NiOOH_{10,000s}$ working electrode with NiOOH deposited from a pH=5.8 solution (a) or using a $WO_3 \mid FeOOH_{10,000s} \mid NiOOH_{1,000s}$ electrode with NiOOH deposited form a pH=7.0 solution (b).

To begin, a linear sweep voltammograms were run to see any photocurrent density changes upon addition of benzyl alcohol ($PhCH_2OH$) to the electrolyte (Figure 2.9). A working electrode of WO_3 with a 10,000 s deposition of FeOOH was used ($WO_3 \mid FeOOH_{10,000s}$). This electrode was chosen due to the high stability (Figure 2.6) and hydroxyl radical suppression capabilities (Figure 2.7) of this material. However, no difference in photocurrent density onset or magnitude was seen during this experiment. This indicates that it is likely no $PhCH_2OH$ is occurring on the surface of the electrode. Choi et al. have shown that FeOOH is not an electrocatalyst for 5-HMF oxidation in pH=13 aqueous solutions, so while it was thought that the photoelectrocatalytic system could conduct alcohol oxidation in a more acidic environment, the result of a lack of reactivity of $WO_3 \mid FeOOH$ towards $PhCH_2OH$ oxidation came as no surprise.[15] In this same Choi report, however, it was demonstrated that NiOOH was an electrocatalyst for 5-HMF oxidation. This group had also previously shown that a photoelectrode comprised of $BiVO_4$ with a layer of FeOOH followed by NiOOH (in that order) improved the overall photocurrent density while decreasing the overpotential required for PEC water oxidation.[20] This acted as motivation to attempt $PhCH_2OH$ oxidation on a $WO_3 \mid FeOOH \mid NiOOH$ material.

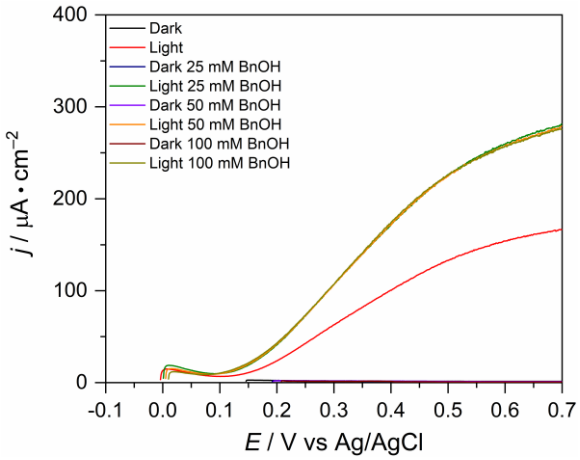

Figure 2.11: Linear sweep voltammograms of pH=7 0.5 M potassium borate electrolyte before (dark (black) and illuminated with 1 sun (red)) and after the addition of increasing concentrations of $PhCH_2OH$ using a $WO_3 \mid FeOOH_{10,000s} \mid NiOOH_{1,000s}$ working electrode.

To deposit NiOOH onto $WO_3 \mid FeOOH_{10,000s}$, an identical procedure was used as to deposit FeOOH onto WO_3, except the Ni was deposited from a solution of $NiSO_4$ and Na_2SO_4. When this electrode was used for $PhCH_2OH$ oxidation, however, the same result was seen as that for the $WO_3 \mid FeOOH_{10,000s}$ electrode – no change in photocurrent density onset or magnitude (Figure 2.10 (a)). However, depositing Ni from a solution that had first had its pH adjusted to 7.0 immediately before deposition resulted in increased photocurrent density magnitude, though the onset of photocurrent was no different before and after the addition of $PhCH_2OH$ (Figure 2.10 (b)). The Ni deposition from the pH~7.0 was only done for 1,000 s since a pH=7 is basic enough to cause slight degradation of the underlying $WO_3 \mid FeOOH$ during deposition. A series of LSVs was then carried out in pH=7.0 0.5 M potassium borate buffer to determine any concentration dependence of $PhCH_2OH$ on the magnitude of photocurrent density. The buffer was switched from pH=4 0.1 M potassium phosphate due to the higher photocurrent densities seen for $WO_3 \mid FeOOH_{10,000s} \mid NiOOH_{1,000s}$ when the NiOOH was deposited from a pH~7.0 solution. The photocurrent density for the LSVs including 25, 50, and 100 mM $PhCH_2OH$ were all above that

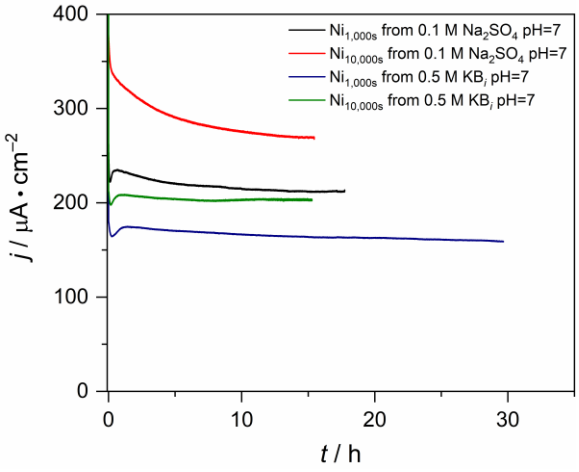

Figure 2.12: Bulk electrolyses of pH=7.0 0.5 M KB_i buffer with 50 mM $PhCH_2OH$. Working electrodes were $WO_3 \mid FeOOH_{1,000s} \mid NiOOH$ electrodes that had their Ni deposited from a 0.1 M Na_2SO_4 / 10 mM 4 solution with its pH adjusted to 7.0 immediately before desposition or from a pH=7 0.5 M KB_i buffer / 10 mM $NiSO_4$ solution at pH=7.0. Ni deposition times were either 1,000 or 10,000 s.

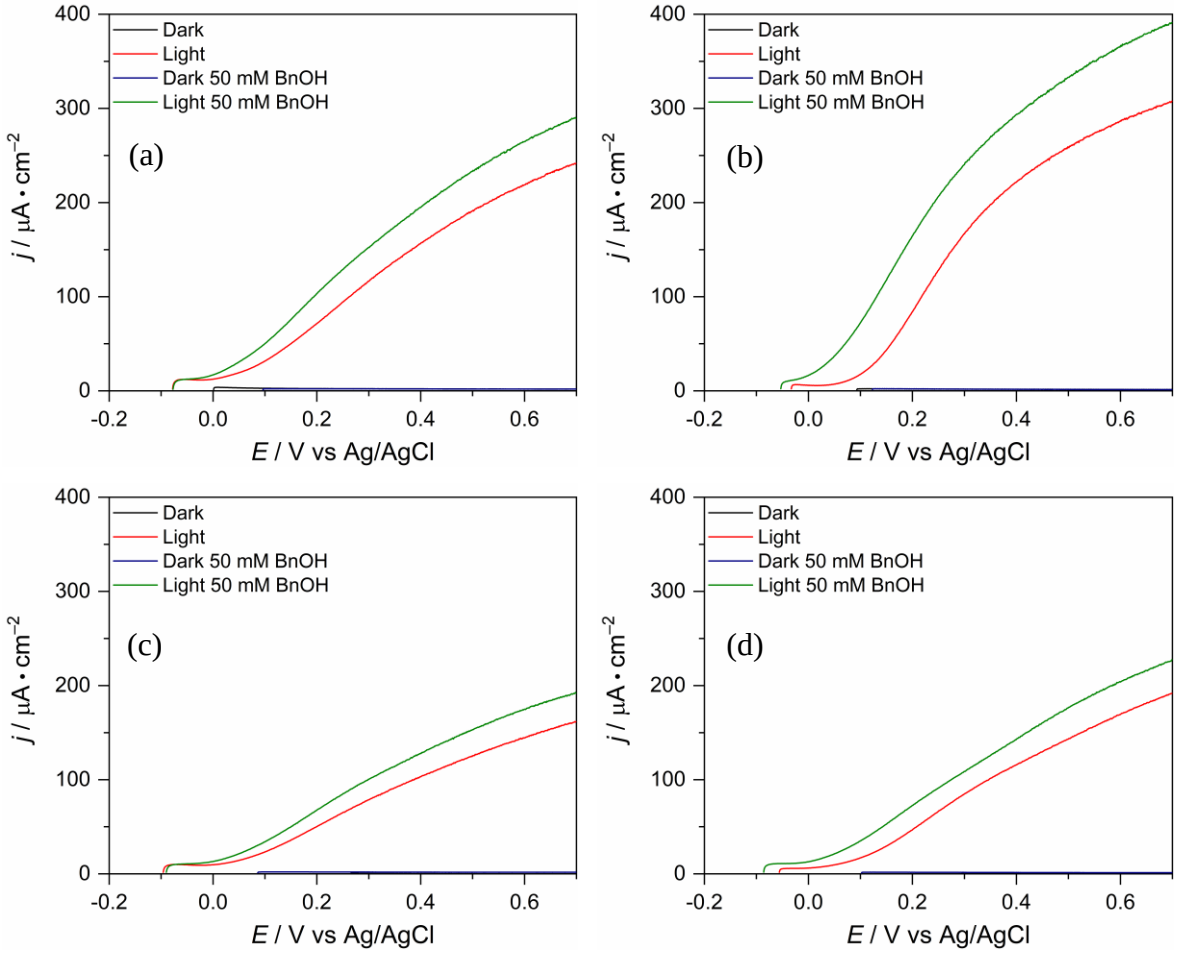

Figure 2.13: Linear sweep voltammograms in 0.5 M pH=7.0 KB_i buffer illuminated by 1 sun using a working electrode of (a) WO_3 | $FeOOH_{1,000s}$ | $NiOOH_{1,000s}$ with Ni deposited from a Na_2SO_4 solution (b) WO_3 | $FeOOH_{1,000s}$ | $NiOOH_{10,000s}$ with Ni deposited from a Na_2SO_4 solution (c) WO_3 | $FeOOH_{1,000s}$ | $NiOOH_{1,000s}$ with Ni deposited from 0.5 M pH=7.0 KB_i buffer and (d) WO_3 | $FeOOH_{1,000s}$ | $NiOOH_{10,000s}$ with Ni deposited from 0.5 M pH=7.0 KB_i buffer. The Na_2SO_4 solutions had their pH adjusted to 7.0 immediately before being used for deposition.

for the LSV run in the absence of $PhCH_2OH$, but there was no increase in the photocurrent density between the LSVs with $PhCH_2OH$ – they were identical (Figure 2.11). This was an indication that photogenerated hole transport from the electrode to the $PhCH_2OH$ was limiting the reaction rate even at 25 mM $PhCH_2OH$.

An issue with the Ni deposition solution was then addressed. While the photocurrent density for $PhCH_2OH$ oxidation increased when the Ni was deposited onto WO_3 | $FeOOH_{10,000s}$ from a Na_2SO_4 solution that had its pH adjusted to 7.0 immediately prior to the deposition, the Na_2SO_4 solution is not a buffer. This means the pH of the solution slowly returned to pH~5.8 over

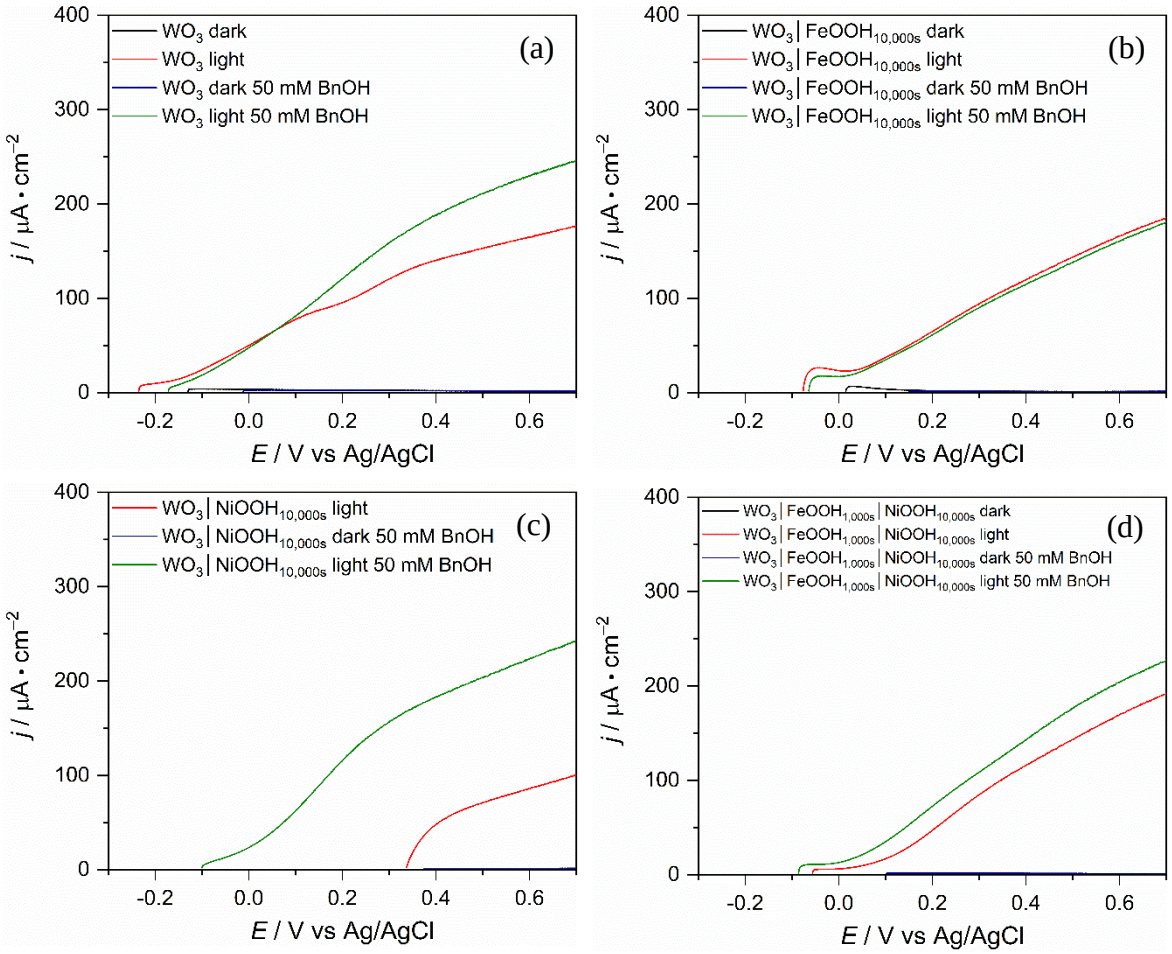

Figure 2.14: Linear sweep voltammograms in 0.5 M pH=7.0 KB_i buffer in the dark and illuminated by 1 sun before and after addition of $PhCH_2OH$ using a working electrode of (a) bare WO_3 (b) $WO_3 \mid FeOOH_{10,000s}$ (c) $WO_3 \mid NiOOH_{10,000s}$ (d) $WO_3 \mid FeOOH_{1,000s} \mid NiOOH_{10,000s}$ with Ni deposited from 0.5 M pH=7.0 KB_i buffer. The dark experiment without $PhCH_2OH$ was omitted from (c) due to the open-circuit potential being more positive than the ending potential for the LSV experiment (i.e. 0.7 V vs Ag/AgCl).

the course of the deposition. Depositing from a buffered pH=7.0 solution is more desirable since it allows deposition from controlled and reproducible conditions. A series of bulk electrolyses were conducted on $WO_3 \mid FeOOH_{1,000s} \mid NiOOH$ films that had Ni deposited from either a Na_2SO_4 solution with its pH adjusted to 7.0 immediately before use for Ni deposition or from a pH=7.0 potassium borate (KB_i) buffer with deposition times of either 1,000 or 10,000 s (Figure 2.12). The Fe deposition was changed to 1,000 s here to expedite experiments. The $WO_3 \mid FeOOH_{1,000s} \mid NiOOH$ films deposited from the Na_2SO_4 solution displayed slightly less stable photocurrent densities than those observed for films with their Ni deposited from KB_i buffer.

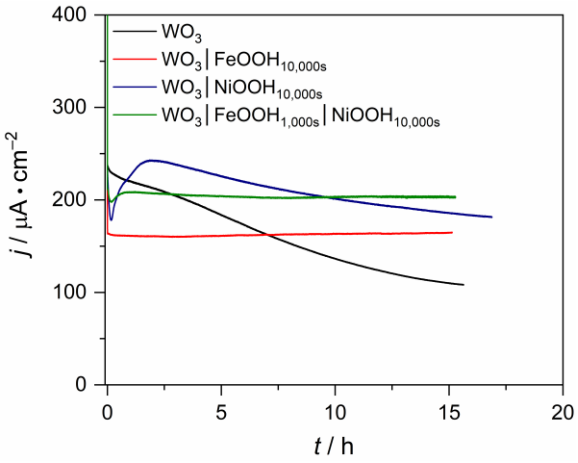

Figure 2.15: Bulk electrolysis experiments conducted in0.5 M pH=7.0 KB_i buffer with 50 mM $PhCH_2OH$ illuminated by 1 sun illumination. Potential held at 1.23 V vs RHE.

Of the two $WO_3 \mid FeOOH_{1,000s} \mid NiOOH$ films with the Ni deposited from KB_i, the 10,000 s deposition time had the higher photocurrent density. All conditions were confirmed to have a rise in photocurrent density upon addition of $PhCH_2OH$ without a significant shift in current onset with LSV experiments (Figure 2.13).

With the conditions for the $WO_3 \mid FeOOH \mid NiOOH$ material decided on to be the $WO_3 \mid FeOOH_{1,000s} \mid NiOOH_{10,000s}$ that had the Ni deposited from KB_i buffer, a comparison of four different working electrode materials was done. The four working electrodes of bare WO_3, $WO_3 \mid FeOOH_{10,000s}$, $WO_3 \mid NiOOH_{10,000}$ and $WO_3 \mid FeOOH_{1,000s} \mid NiOOH_{10,000s}$ were each used for dark and light LSV experiments with added $PhCH_2OH$ (Figure 2.14). The $WO_3 \mid FeOOH_{10,000s}$ electrode was the only material that did not show an increase in photocurrent density upon addition of $PhCH_2OH$. Another notable observation was that the $WO_3 \mid NiOOH_{10,000s}$ was the only electrode that had a significant shift in photocurrent density onset potential after the addition of the $PhCH_2OH$. It also had the highest difference in photocurrent density magnitude between the illuminated experiments with and without $PhCH_2OH$. While these results would suggest $WO_3 \mid NiOOH_{10,000s}$ to be the most suited material for photoelectrocatalytic $PhCH_2OH$ oxidation, the stability of the materials during extended electrolysis needed to be determined to confirm this.

To determine catalyst stability, illuminated bulk electrolysis experiments were run for 15-17 hours under 1 sun illumination (Figure 2.15). The $WO_3 \mid NiOOH_{10,000s}$ material, which showed the most promising photocatalytic LSV data, was not stable during extended electrolysis (Figure

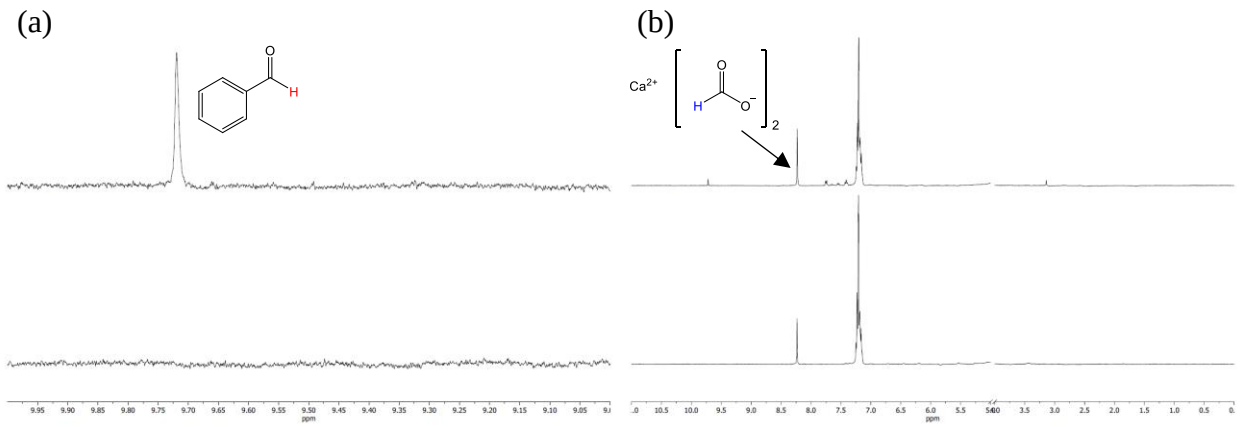

Figure 2.16: Example ^{1}H NMR spectrum used to calculate Faradaic efficiency for the photoelectrocatalytic oxidation of $PhCH_2OH$ to PhCHO (a) zoomed in to show the aldehyde peak of PhCHO and (b) zoomed out to show the full spectrum, including the aldehyde peak for the 10 mM calcium formate standard. Bottom spectra are pre-electrolysis and top spectra are post-electrolysis.

2.14 (c), Figure 2.15). The current was observed to increase for the first ~2 hours but then decreased over the remainder of the experiment. The bare WO_3 was also not stable over the electrolysis, with its photocurrent density decreasing from the beginning of the experiment forward. The materials with an FeOOH coat both displayed stable photocurrent density, with the $WO_3 \mid FeOOH_{1,000s} \mid NiOOH_{10,000s}$ material maintained a photocurrent density about 50 μA • cm^{-2} higher than that for the $WO_3 \mid FeOOH_{10,000s}$.

The Faradaic efficiency for $PhCH_2OH$ oxidation was then determined for the two stable materials (i.e. $WO_3 \mid FeOOH_{10,000s}$ and $WO_3 \mid FeOOH_{1,000s} \mid NiOOH_{10,000s}$) and compared to that for bare WO_3 (Table 2.2). To do this, the working compartment solution was analyzed by ^{1}H NMR after a bulk electrolysis had been run. The aldehyde peak for PhCHO was integrated and compared to the aldehyde peak of a standard 10 mM concentration of calcium formate (Figure 2.16). The Faradaic efficiency values for all materials investigated were between 1.5–2.1%. These low

Table 2.2: Faradaic efficiency of different materials for the photoelectrocatalytic oxidation of $PhCH_2OH$ to PhCHO

Material	Time (h)	Charge Passed (C)	Faradaic Efficiency (%)
Bare WO_3	113.0	407	1.58
$WO_3 \mid FeOOH_{10,000s}$	47.8	62.3	1.62
$WO_3 \mid FeOOH_{1,000s} \mid NiOOH_{10,000s}$	48.8	27.8	2.05

Faradaic efficiency values indicate that the oxyhydroxide materials do not promote the catalysis of $PhCH_2OH$ oxidation. While no O_2 measurements have been conducted, it is hypothesized that the majority of the charge in these experiments went to water oxidation to produce O_2 gas, independent of the material used.

2.6 Conclusions

It was hypothesized that adding a layer of FeOOH to a WO_3 electrode would decrease the quantity of hydroxyl radical generated during photoelectrocatalytic water oxidation on this material. This hypothesis was based on the calculated valence band position of FeOOH (i.e. 2.11 V vs NHE), which is too negative to oxidize water into •OH. Fluorescence measurements of pH=4 potassium phosphate solutions that had undergone PEC water oxidation on $WO_3 \mid FeOOH_{xs}$ (where x = 0, 100, 1,000, and 10,000) revealed that, indeed, the quantity of •OH detected after PEC water oxidation decreased as the photodeposition time of FeOOH increased. While photocurrent density also decreases as the photodeposition time of FeOOH is increased, this is thought to be due, at least in part, to the electrode having increased Faradaic efficiency for water oxidation. This could be confirmed by O_2 measurements of the headspace during PEC water oxidation with a GC-TCD system (TCD = thermal conductivity detector).

Given the lack of •OH detected after PEC water oxidation on $WO_3 \mid FeOOH$ materials, it was hypothesized that this suggested a change in water oxidation mechanism, which would lead to differing Tafel slopes. Since FeOOH has been shown to be an electrocatalyst for water oxidation, it was expected that the $WO_3 \mid FeOOH$ materials would exhibit a shallower Tafel slope than bare WO_3. This expectation was shown to be valid, as the Tafel slopes for WO_3 and $WO_3 \mid FeOOH_{10,000s}$ were found to be 172 ± 7 and 77 ± 14 mV • dec^{-1}, respectively.

Knowing that WO_3 | FeOOH generated less •OH during PEC water oxidation, it was thought that this would lead to a more favorable environment for selectively organic oxidations, which are typically difficult to achieve on metal oxides in aqueous environments due to the generation of •OH on the surface of photoexcited metal oxides that indiscriminately. When no increase in photocurrent density was observed upon addition of benzyl alcohol to LSV experiments, a set of conditions was found to deposit NiOOH onto the WO_3 | FeOOH material that led to an electrode which did demonstrate an increase in photocurrent density upon addition of benzyl alcohol. NiOOH was chosen because it had been reported to be an electrocatalyst for aqueous 5-hydroxylmethylfurfural oxidation (though this chemistry was carried out at pH=13).[15] The WO_3 | $FeOOH_{1,000s}$ | $NiOOH_{10,000s}$ material was shown to give stable photocurrent density over the course of extended electrolysis as well. However, when the Faradaic efficiency for benzyl alcohol photocatalytic oxidation was calculated after extended bulk electrolysis for bare WO_3, WO_3 | $FeOOH_{10,000s}$ and WO_3 | $FeOOH_{1,000s}$ | $NiOOH_{10,000s}$, they were all between 1.5 – 2.1%. These efficiencies show that the metal oxyhydroxide layers do not increase the Faradaic efficiency of bare WO_3 for photocatalytic $PhCH_2OH$ oxidation.

After the lack of reactivity of alcohols observed here, other organic substrates were sought out to act as model compounds for organic oxidations on metal oxides. Amines were chosen, given their amine/imine redox couples are more negative than those for alcohols/aldehydes. Another metal oxide, $CuWO_4$, which absorbs greater wavelengths of light was also chosen as the photoanode of choice. Investigations concerning this chemistry, all of which was moved to nonaqueous conditions and driven by a blue LED illumination source, can be found in Chapter 3 of this thesis.

2.7 Experimental

Materials and Methods

Ammonium metatungstate, poly(ethylene glycol) (M_W = 300 Da), iron (II) sulfate heptrahydrate (ACS reagent, ≥99,0%), , potassium phosphate monobasic (ACS reagent, ≥99.0%), boric acid (ReagentPlus, ≥99.5%), potassium hydroxide (ACS reagent, ≥85%, pellets), were purchased from Sigma-Aldrich. Sodium sulfate decahydrate (Alfa Aesar, 99%), nickel (II) sulfate hexahydrate (99%, for analysis), benzyl alcohol (certified ACS), and benzaldehyde were purchased from Fisher. Deuterium oxide was purchased from Cambridge Isotope Laboratories. The iron (II) sulfate heptahydrate was recrystallized from 0.4 M sulfuric acid at 60 °C. All other chemicals were used as received. All water was filtered through a Millipore filtration system to give water with a resistance of 18.2 MΩ • cm^{-2} before use in experiments. Ag/AgCl reference electrodes were purchased from CHI and were filled with saturated aqueous KCl solution. Silver print was purchased from Jameco. Epoxy was purchased from R.S. Hughes (Loctite Hysol 1C off-white two-part epoxy adhesive - 4 oz kit, part no. 1373425, Henkel). Fluorinated tin oxide coated glass was purchased from Pilkington Glass (TEC 15).

Materials Characterization

Powder x-ray diffraction data were collected on a Panalytical Empyrean diffractometer at a power of 1.8 kW (45 kV, 40 mA) with Cu Kα (λ = 1.5418 nm) radiation. The detector was a X'Celerator Scientific, a position sensitive 1D detector equipped with Bragg-Brentano^{HD} x-ray optic delivering only Kα radiation. Patterns were collected with a sampling step of 0.020 and a scan rate of 0.080°• s^{-1} while spinning at a rate of 0.25 Hz. Scanning electron microscopy was conducted on a JEOL JSM-7800FLV instrument. XPS was collected using a Kratos Axis Ultra X-ray photoelectron

spectrometer. The X-rays used were monochromatic Al Kα X-rays (1486.7 eV) and measurements were performed at an analysis chamber pressure of ≈1×10^{-9} Torr. An electron flood gun was used to compensate for charging during data collection. Casa XPS software was used with a Shirley-type baseline to calculate the peak areas; binding energies were determined by setting adventitious carbon signal to 248.8 eV.

Catalyst Preparation

WO_3 Electrodes

Tungsten oxide (WO_3) films were prepared by spin-coating. First, 2.51 g of ammonium metatungstate was dissolved in 10 mL of Milli-Q water by stirring. This gives a solution that is 0.5 M in tungsten. In a separate beaker, 6.6 g of polyethylene glycol (MW=300) was added and dissolved in 10 mL of 200 proof ethanol by stirring. The polyethylene glycol solution was then added to the ammonium metatungstate solution dropwise, making a colorless and opaque liquid. Once made, this WO_3 precursor was constantly stirred until all films were complete. A volume of 35 µL of the WO_3 precursor solution was pipetted onto a 2.5 cm long x 1.3 cm wide fluorinated tin oxide (FTO) conducting glass slide that were taped off with Scotch tape to have 1 x 1.3 cm of FTO revealed. This were spun at 2500 rpm for 30 seconds. The film was then annealed at 500 °C for 30 minutes. After removing from the oven, the film was allowed to cool for about 15-30 minutes before adding another identical coat. This process was done until 10 total coats had been placed onto the FTO slide. Copper wire was attached to the FTO with silver paint and allowed to dry overnight before placing a glass tube around the copper wire and attaching it to the electrode with epoxy. After the epoxy was added, only the 1 x 1.3 cm area that contained the WO_3 and the 1 x 1.3 cm area on the opposite side (non-conducting side) of the slide were exposed.

WO_3 | FeOOH Electrodes

A volume of 100 mL of 0.1 M aqueous sodium sulfate was added to a quartz window-containing cell. A mass of 278 mg of iron (II) sulfate heptahydrate (recrystallized from 0.4 M aqueous H_2SO_4, heated to 60 °C) was added along with a stir bar. The solution was stirred until the $FeSO_4 \cdot 7H_2O$ had dissolved (occurred readily). A WO_3 electrode was submerged into the solution, with the backside (i.e. non-conductive side) facing a Xenon arc lamp. The light from the lamp passed through an AM1.5G filter before striking the electrode surface with a power density of 100 mW • cm^{-2}. A chronopotentiometry experiment was run with a three-electrode setup (WO_3 = working, Ag/AgCl = reference, graphite rod = counter) over varying time periods (100, 1,000, and 10,000 s) while passing 58 uA • cm^{-2}. This leaves a slightly orange tint on the electrode. After the photoelectrodeposition, the electrode was rinsed with DI water and immediately used for an experiment.

WO_3 | FeOOH | NiOOH Electrodes

A volume of 100 mL of 0.5 M aqueous potassium borate buffer was added to a quartz window-containing cell. A mass of 263 mg of nickel (II) sulfate was added along with a stir bar. The solution was stirred until the $NiSO_4$ had dissolved (occurred readily). A WO_3 | FeOOH electrode was submerged into the solution, with the backside (i.e. non-conductive side) facing a Xenon arc lamp. The light from the lamp passed through an AM1.5G filter before striking the electrode surface with a power density of 100 mW • cm^{-2}. A chronopotentiometry experiment was run with a three-electrode setup (WO_3 = working, Ag/AgCl = reference, graphite rod = counter) over varying time periods while passing 58 uA • cm^{-2}. After the photoelectrodeposition, the electrode was rinsed with DI water and immediately used for an experiment.

Photoelectrocatalytic Measurements

All electrochemistry was conducted on a CHI660 potentiostat. All experiments were illuminated with a xenon lamp irradiation source that passed through an AM1.5G filter and struck the backside of the working electrode with a power density of 100 mW • cm^{-2}. A silver wire in saturated KCl was used as the Ag/AgCl reference electrode. A graphite rod was used as the counter electrode. Photoelectrodepositions of FeOOH and NiOOH were carried out in a glass one-compartment cell that had a quartz window. All linear sweep voltammetry and bulk electrolysis measurements were done in a two-compartment glass cell with a quartz window on the working compartment and a Nafion membrane separating the two compartments. All linear sweep voltammetry was conducted with a scan rate of 10 mV • s^{-1}. The open circuit potential was always used as the starting potential. The sensitivity of the potentiostat was set to 10^{-3} amperes on the CHI software. Bulk electrolysis experiments were always run at an applied potential of 1.23 V vs RHE. The electrolyte used was either pH=4.0 0.1 M aqueous potassium phosphate buffer or pH=7.0 0.5 M aqueous potassium borate buffer. The pH=4 0.1 M potassium phosphate buffer was made by adding 6.805 g of potassium phosphate monobasic to 500 mL of Millipore water and stirred until dissolved to give 0.1 M KH_2PO_3. Then concentrated phosphoric acid was added dropwise until the pH decreased to 4.0. The pH=7.0 potassium borate buffer was made by adding 6.185 g of boric acid to 500 mL of Millipore water and stirred until dissolved to give 0.5 M boric acid. Then pellets of potassium hydroxide were added until the pH increased to 7.0. The volumes of buffer used were 16 mL in the working compartment and 8 mL in the counter compartment.

Fluorescence Measurements

Fluorescence spectroscopy was carried out on a PTI Quanta Master using a Xe arc lamp irradiation source. The irradiation slit width was 5 nm and the emission slit width was 3 nm. The excitation wavelength was 332 nm. Emission spectra were collected from 325 to 600 nm. Sample containers were quartz glass cuvettes.

Photoelectrocatalytic Experiments for Hydroxyl Radical Detection

All photoelectrocatalytic experiments for hydroxyl radical detection during PEC water oxidation were carried out in 0.1 M pH=4 aqueous potassium phosphate buffer with 1 mM coumarin included. Bulk electrolysis and linear sweep voltammetry experiments carried out with WO_3 | FeOOH electrodes were done so using WO_3 | FeOOH electrodes that had just undergone the FeOOH photoelectrodeposition. A two-compartment cell was used for all bulk electrolysis and linear sweep voltammetry experiments. The two compartments were held together by a C-clamp, with an o-ring and piece of Nafion in between them. The WO_3 working and Ag/AgCl reference electrodes were in one compartment, while the graphite rod counter was in the opposite compartment. Two linear sweep voltammetry experiments were always run prior to any bulk electrolysis. One was first done in the dark followed by one during illumination by 1 sun irradiation (i.e. 100 mW • cm^{-2} of light passed through an AM1.5G filter) from the open circuit potential to 0.9 V vs. Ag/AgCl (1.33 V vs. RHE). Before a bulk electrolysis was started, the solution in the working compartment was placed into a quartz cuvette and fluorescence spectroscopy was run on the sample. This solution was added back to the working side of the two-compartment cell before the bulk electrolysis was started. All bulk electrolyses were conducted with stirring and held at 0.797 V vs Ag/AgCl (1.23 V vs. RHE) while being irradiated by 1 sun illumination. Once 2

coulombs of charge had been passed, the experiment was stopped, and fluorescence spectroscopy was run on a portion of the solution in the working compartment.

Tafel Measurements

Tafel slopes were calculated from data collected during linear sweep voltammetry experiments. These LSVs were conducted much slower than other LSVs conducted in this work, being set to 0.1 $mV \bullet s^{-1}$. This slow scan rate is to allow for the rate of the reaction taking place at the electrode surface to be limited by charge transfer between substrate and the electrode, instead of diffusion of substrate to the electrode surface, for as long as possible. As with other LSVs, the open circuit potential was chosen as the starting potential and the two-compartment cell housed the reactions as they took place under 1 sun of illumination. The solution was also stirred during the LSVs to ensure enough substrate reaches the surface to avoid the reaction from becoming diffusion limited.

Faradaic Efficiency of Photoelectrocatalytic $PhCH_2OH$ Oxidation

A bulk electrolysis was run in the two-compartment cell with 16 mL of 0.5 M pH=7.0 potassium borate buffer added to the working side and 8 mL added to the counter side. Next, 84 µL of benzyl alcohol was added with a micropipette to the working side and 42 µL to the counter side. The solutions of both compartments were stirred until the benzyl alcohol dissolved, giving 50 mM in both sides. The benzyl alcohol did not dissolve immediately; it took 5-10 minutes to go into solution. Once dissolved the stir bar was removed from the counter compartment (the one in the working compartment was left there). The cell was then illuminated with 100 $mW \bullet cm^{-1}$ of light from a Xe arc lamp filtered by an AM1.5G filter. The solution was stirred and then the bulk electrolysis experiment was started. The applied potential for all bulk electrolysis experiments

done here was 1.23 V vs RHE. These experiments were run for various amounts of time, with the goal of passing enough charge to allow for detection of benzaldehyde by ^{1}H NMR. Once enough charge had been passed, the experiment was stopped. A volume of 540 µL of the working solution was added with a micropipette to an NMR tube that contained 60 µL of a standard solution of 100 mM calcium formate in D_2O. The D_2O was used in this case to allow for proper locking and shimming of the NMR magnet. All ^{1}H NMR experiments were carried out on a Varian MR400 NMR spectrometer equipped with a Varian 5 mm Dual Broadband probe. All NMR data processed in MestReNova software. An example calculation for the charge passed by the WO_3 | $FeOOH_{1,000s}$ | $NiOOH_{10,000s}$ material (Table 2.2) is below.

$$Faradaic\ efficiency = \frac{n \times N \times F}{Q}$$

n is the number of electrons required for the process (*n* = 2 for $PhCH_2OH$ oxidation)

N is the quantity of product detected after catalysis has been stopped

F is the Faraday constant (i.e. 96,485.3365 Coulombs of charge / mol of electrons)

Q is the total charge passed during the experiment.

To calculate the FE of $PhCH_2OH$ oxidation from the ^{1}H NMR data, the absolute area of the BnAld peak was compared to the absolute area of the calcium formate peak divided by two (there are two formates per one calcium, so this peak represents the signal from two protons). The charge passed during the bulk electrolysis was 27.8 C.

First, the number of moles of electrons passed during the experiment is calculated by multiplying the charge passed in Coulombs by Faraday's constant.

$$(27.8C)\left(\frac{1\ mol\ e^-}{96{,}485.34\ C}\right) = 2.88\ \times 10^{-4}\ mol\ e^-\ passed\ during\ the\ experiment$$

The absolute peak area of the calcium formate peak is 1842.57, which divided by two is 921.285. The absolute peak area of the BnAld peak is 15.87. The concentration of benzaldehyde in the NMR sample can be calculated from these data.

$$\left(\frac{10\ mM}{921.285}\right) = \left(\frac{x\ mM}{15.87}\right)$$

$$x = 0.172\ mM\ PhCHO\ in\ the\ NMR\ sample$$

Taking into account the dilution of the NMR sample from 540 µL to 600 µL by the addition of the 60 µL of 100 mM calcium formate in D_2O we get the concentration of the solution in the working compartment of the photoelectrochemical cell.

$$(0.172\ mM\ PhCHO)\left(\frac{600\ \mu L}{540\ \mu L}\right) = 0.191\ mM\ PhCHO\ in\ PEC\ cell$$

Now, considering that 2 moles of electrons are required to oxidize 1 mole of $PhCH_2OH$ to 1 mole of PhCHO we get the below equation to solve for the number of electrons that went into PhCHO production. The volume of 15.46 mL (the working compartment volume) is used instead of 16.00

mL because a volume of 540 µL was taken out of the working compartment to run a pre-electrolysis NMR, which was never returned to the working compartment.

$$\left(\frac{0.000191\ mol\ PhCHO}{1000\ mL}\right)\left(\frac{2\ mol\ e^-}{1\ mol\ PhCHO}\right)(15.46\ mL) = 5.91 \times 10^{-6}\ mol\ e^-\ to\ PhCHO$$

Finally, the number of electrons that went PhCHO generation are divided by the total number of electrons passed to give the Faradaic efficiency for PhCHO production.

$$\frac{5.91\ \times 10^{-6} mol\ e^-\ towards\ PhCHO}{2.88 \times 10^{-4} mol\ e^-\ passed\ total} = 2.05\%\ Faradaic\ Efficiency$$

2.7 References

[1] Hydrogen Basics. https://afdc.energy.gov/fuels/hydrogen_basics.html (accessed September 8, 2019).

[2] Mi, Q.; Zhanaidarova, A.; Brunschwig, B. S.; Gray, H. B.; and Lewis, N. S. A quantitative assessment of the competition between water and anion oxidation at WO_3 photoanodes in acidic aqueous electrolytes. *Energy Environ. Sci.* **2012**, *5*, 5694-5700.

[3] Lhermitte, C. R.; Verwer, J. G.; and Bartlett, B. M. Improving the stability and selectivity for the oxygen-evolution reaction on semiconducting WO_3 photoelectrodes with a solid-state FeOOH catalyst. *J. Mater. Chem. A* **2016**, *4*, 2960-2968.

[4] Wardman, P. Reduction Potentials of One-Electron Couples Involving Free Radicals in Aqueous Solution. *J. Phys. Chem. Ref. Data* **1989**, *18*, 1637-1755.

[5] Yan, J.; Li, P.; Ji, Y.; Bian, H.; Li, Y. and Liu, S. Earth-abundant elements doping for robust and stable solar-driven water splitting by FeOOH. *J. Mater. Chem. A* **2017**, *5*, 21478-21485.

[6] Grosvenor, A. P.; Kobe, B. A.; Biesinger, M. C. and McIntyre, N. S. Investigation of multiplet splitting of Fe 2p XPS spectra and bonding in iron compounds. *Surf. Interface Anal.* **2004**, *36*, 1564-1574.

[7] Zhang, J. and Nosaka, Y. Mechanism of the OH Radical Generation in Photocatalysis with TiO_2 of Different Crystalline Types. *J. Phys. Chem. C* **2014**, *118*, 10824-10832.

[8] Huynh, M.; Ozel, T.; Liu, C.; Lau, E. C. and Nocera, D. G. Design of template-stabilized active and earth-abundant oxygen evolution catalysts in acid. *Chem. Sci.* **2017**, *8*, 4779-4794.

[9] Huang, J.; Ding, Y.; Luo, X. and Feng, Y. Solvation effect promoted formation of p-n junction between WO_3 and FeOOH: A high performance photoanode for water oxidation. *J. Catal.* **2016**, *333*, 200-206.

[10] Kwong, W. L.; Lee, C. C. and Messinger, J. Transparent Nanoparticulate FeOOH Improves the Performance of a WO_3 Photoanode in a Tandem Water-Splitting Device. *J. Phys. Chem. C* **2016**, *120*, 10941-10950.

[11] Ge, G.; Liu, M.; Liu, C.; Zhou, W.; Wang, D.; Liu, L. and Ye, J. Ultrathin FeOOH nanosheets as an efficient cocatalyst for photocatalytic water oxidation. *J. Mater. Chem. A* **2019**, *7*, 9222-9229.

[12] Zhang, B.; Wang, L.; Zhang, Y.; Ding, Y. and Bi, Y. Ultrathin FeOOH Nanolayers with Abundant Oxygen Vacancies on $BiVO_4$ Photoanodes for Efficient Water Oxidation. *Angew. Chem. Int. Ed.* **2018**, *57*, 2248-2252.
[13] You, B.; Liu, X.; Jiang, N. and Sun, Y. A General Strategy for Decoupled Hydrogen Production from Water Splitting by Integrating Oxidative Biomass Valorization. *J. Am. Chem. Soc.* **2016**, *138*, 13639-13646.
[14] Galaverna, R.; Breitkreitz, M. C. and Pastre, J. C. Converstion of D-Fructose to 5-(Hydroxymethyl)furfural: Evaluating Batch and Continuous Flow Conditions by Design of Experiments and In-Line FTIR Monitoring. *ACS Sustainable Chem. Eng.* **2018**, *6*, 4220-4230.
[15] Taitt, B. J.; Nam, D.-H. and Choi, K.-S. A Comparative Study of Nickel, Cobalt, and Iron Oxyhydroxide Anodes for the Electrochemical Oxidation of 5-Hydroxymethylfurfural to 2,5-Furandicarboxylic Acid. *ACS Catal.* **2019**, *9*, 660-670.
[16] Cha, H. G. and Choi, K.-S. Combined biomass valorization and hydrogen production in a photoelectrochemical cell. *Nature Chem.* **2015**, *7*, 328-333.
[17] Xu, S.; Zhou, P.; Zhang, Z.; Yang, C.; Zhang, B.; Deng, K.; Bottle, S. and Zhu, H. Selective Oxidation of 5-Hydroxymethylfurfural to 2,5-Furandicarboxylic Acid Using O_2 and a Photocatalyst of Co-thioporphyrazine Bonded to g-C_3N_4. *J. Am. Chem. Soc.* **2017**, *139*, 14775-14782.
[18] Battula, V. R.; Jaryal, A. and Kailasam, K. Visible light-driven simultaneous H_2 production by water splitting couple with selective oxidation of HMF to DFF catalyzed by porous carbon nitride. *J. Mater. Chem. A* **2019**, *7*, 5643-5649.
[19] Hun, G.; Jin, Y.-H.; Burgess, R. A.; Dickenson, N. E.; Cao, X.-M. and Sun, Y. Visible-Light Driven Valorization of Biomass Intermediates Integrated with H_2 Production Catalyzed by Ultrathin Ni/CdS Nanosheets. *J. Am. Chem. Soc.* **2017**, *139*, 15584-15587.
[20] Kim, T. W. and Choi, K.-S. Nanoporous $BiVO_4$ Photoanodes with Dual-Layer Oxygen Evolution Catalysts for Solar Water Splitting. *Science* **2014**, *343*, 990-994.

Chapter 3 Photoelectrocatalytic Oxidation of Amines on $CuWO_4$

3.1 Introduction

Looking towards renewable starting materials for water oxidation, biomass seems appealing due to the many hydroxyl groups on these compounds that could be oxidized. However, these compounds, such as lignin and cellulose, are not water soluble. They are also difficult to oxidize selectively due to their varying size and structure, making the generation of a useful product from their oxidation a challenge. While the task of achieving selective oxidation of these biomass compounds is being undertaken,[1–4] they are poor starting materials when viewed as a replacement for water oxidation in the oxidation half-reaction of water splitting. These compounds can be broken down into more manageable lower molecular weight compounds, which are better suited for this application. For example, cellulose can be broken down into its C6 sugar constituents, glucose and fructose, which can undergo triple dehydration to yield 5-hydroxymethylfurfural (5-HMF). This biomass-derived compound can undergo multiple oxidation reactions that result in 2,5-furandicarboxylic acid (FDCA), a compound recognized by the U.S. Department of Energy as one of the top 12 sugar-derived building block chemicals that "could serve as an economic driver for a biorefinery." [5] The oxidation of 5-HMF to FDCA results in the generation of one free proton, making this reaction capable of generating the protons necessary for proton reduction to get H_2 gas.

This reaction is an example of how organic substrates could act as a favorable substitute for water in the oxidation half-reaction of water splitting. As discussed in the introduction to this

thesis, metal oxides can act as visible-light absorbing photocatalysts for oxidation reactions. To investigate organic oxidations on metal oxides electrodes, I chose copper (II) tungstate ($CuWO_4$) as the metal oxide catalyst. This material has been a focus of the Bartlett lab for many years, where it has mainly been utilized as a water oxidation photoelectrocatalyst.[6–11] The decision was made to continue to use this material as a photoelectrocatalyst (as opposed to a photocatalyst) since this allows for only oxidation reactions to take place at the working $CuWO_4$ electrode. The photoexcited electrons of the $CuWO_4$ are attracted to the counter electrode *via* an applied potential where they are used to conduct reduction reactions.

For this work, beginning with 5-HMF as the starting compound was too ambitious because of the dual functionality of the substrate (both an aldehyde and alcohol) combined with the fact that alcohol oxidation is more thermodynamically difficult than amine oxidation. While it would be ideal to oxidize 5-HMF to FDCA with 100% selectivity in water, a simpler substrate was chosen to begin work on oxidizing organic substrates on visible light-absorbing metal oxide semiconductors – amine oxidation in acetonitrile solvent, with a focus on benzylamine. Benzylamine is more electron rich than alcohols and are therefore expected to require less positive potentials (i.e. less driving force) to be oxidized. Acetonitrile was chosen as the solvent due to the high quantities of it is capable of solubilizing and its high oxidative stability (stable out to ~3 V vs RHE). If these reactions were conducted in water, water oxidation could contend as a competing reaction, interfering with the investigation of how organic substrates are oxidized, but since acetonitrile is unreactive out to such high potentials, no reactions are expected to occur between $CuWO_4$ and the solvent.

3.2 Synthesis and Characterization of $CuWO_4$ Photoelectrodes

A spray pyrolysis method was used to synthesize $CuWO_4$ films. A solution 10 mM in Cu^{2+} (using $CuCl_2$) and 2 mM in HCl (added to prevent the copper from precipitating) was added to a solution 10 mM in W^{6+} (using ammonium metatungstate that was then sprayed onto fluorinated tin oxide glass (FTO) slides that were being heated by a hot plate. These sprays form a film of amorphous material according to the hypothesized reaction (3.1.1).

$$12CuCl_{2(aq)} + (NH_4)_6H_2W_{12}O_{40(aq)} + 8H_2O_{(l)} \rightarrow 12CuWO_{4(s)} + 6NH_{3(g)} + 24HCl_{(g)} \qquad (3.1.1)$$

After 100 sprays, the films were placed into a furnace to anneal the material to crystalline $CuWO_4$ (Figure 3.1 (a)). The crystalline $CuWO_4$ has a morphology consisting of 100-200 nm particles (Figure 3.1 (b)). After the annealing process, a piece of copper wire was attached to the remaining clean FTO section of the slide with conductive silver paint and epoxy was applied to complete the electrode (Figure 3.1 (c)). The epoxy was placed on the electrode to allow for a 1 x 1 cm^2 area of $CuWO_4$ to be exposed.

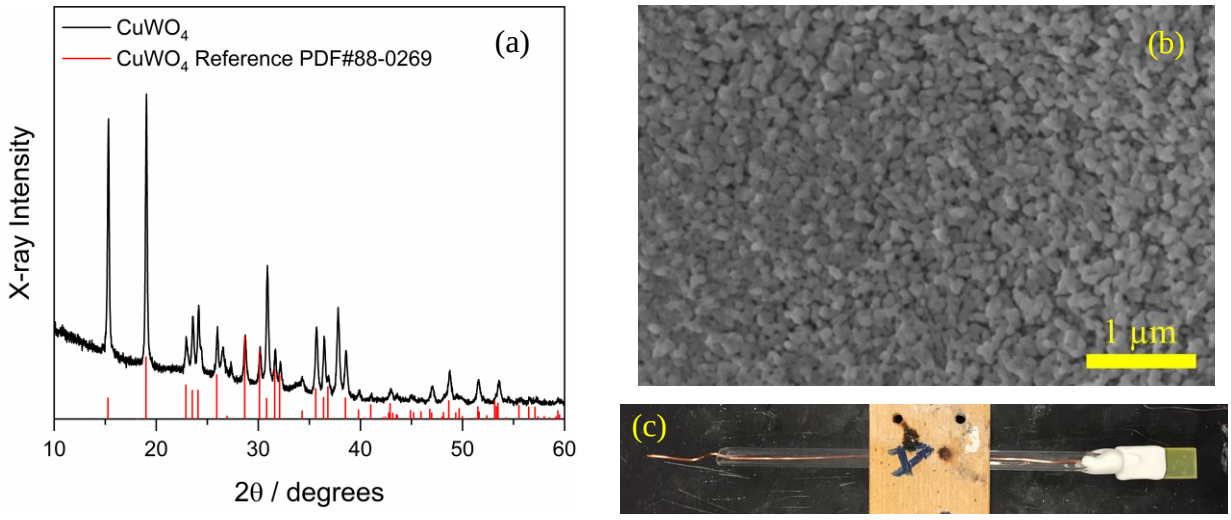

Figure 3.1: (a) Powder X-ray diffractogram and (b) scanning electron microscope image of an annealed $CuWO_4$ film. Red lines in the diffractogram represent a calculated reference pattern for $CuWO_4$. (c) Photograph of completed $CuWO_4$ electrode.

3.3 Photoelectrocatalytic Oxidation of Benzylamine on $CuWO_4$ Photoelectrodes

All oxidations were carried out in a two-compartment cell (Figure 3.2). The working electrode was a $CuWO_4$ film that was illuminated from the backside of the electrode. It was reported by our lab that WO_3 films displayed a higher photocurrent when illuminated from the backside when compared to frontside illuminated films, which is why backside illumination was used in the experiments in this work.[12] Reactions were conducted in acetonitrile (MeCN) solvent with a concentration of 100 mM tetrabutylammonium hexafluorophosphate ($TBAPF_6$) as the electrolyte and 500 mM benzylamine ($BnNH_2$) as the amine to be oxidized. The reference electrode was a silver wire in 100 mM $TBAPF_6$ in MeCN with 10 mM $AgNO_3$. Using the $Ag/AgNO_3$ couple as a reference is common in nonaqueous electrochemistry. A platinum mesh was used as the counter electrode. Three strips of blue LEDs were used as the light source, with the cell being placed as close to them as possible for a power density at the working electrode of ~30-45 $mW \bullet cm^{-2}$. These have a peak wavelength of 465 nm, which does overlap with the absorbance spectrum of $CuWO_4$ (Figure 3.3). This light source is therefore capable of exciting electrons from the valence band to the conduction band of $CuWO_4$, allowing the material to act as a photoelectrocatalyst.

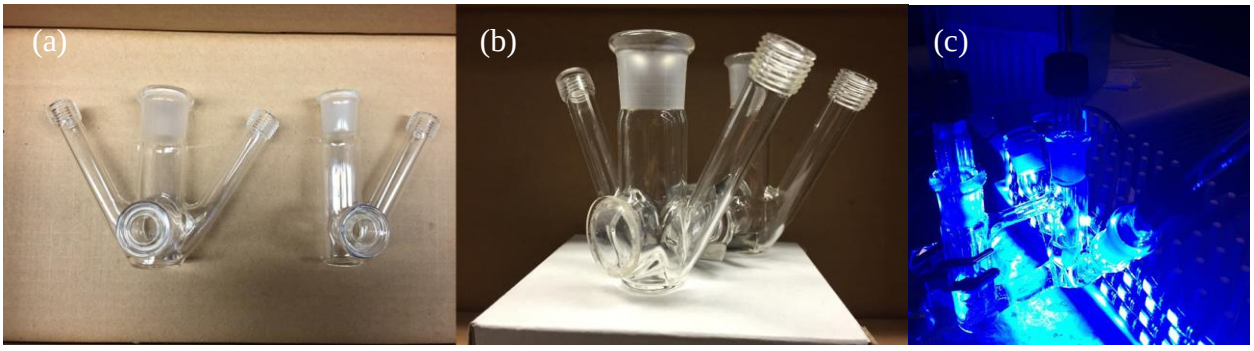

Figure 3.2: Photographs of the two-compartment cell with a quartz window used for photoelectrocatalytic amine oxidations (a) with both compartments separated (working electrode and reference electrode are placed in the left compartment, the counter electrode is placed in the right compartment) (b) with both compartments joined with a c-clamp and o-ring, with a piece of Nafion in between and (c) under operation in front of blue LEDs.

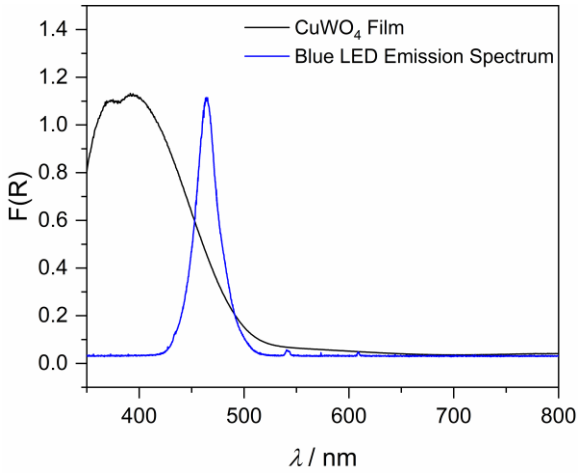

Figure 3.4: Diffuse reflectance spectrum of a $CuWO_4$ film (black) demonstrating an onset of absorbance just below above 500 nm overlaid with the emission spectrum of the blue LEDs (blue) used as the light source for all photoelectrochemical experiments in this work.

It is important that the electrolyte is stable under operating conditions. This was confirmed for the MeCN/$TBAPF_6$ by performing linear sweep voltammetry (LSV) on the electrolyte solution. There is no onset of current in the dark in the scanned window from open circuit potential (OCP, the potential at which no current is flowing) to 0.8 V vs Ag/$AgNO_3$. Current is observed in for the electrolyte when illuminated, with the onset of current occurring at around 1.0 V vs Ag/$AgNO_3$. When 500 mM $BnNH_2$ is added and an LSV is run in the dark, no current is observed until just under 0.5 V vs Ag/$AgNO_3$. This is expected in the dark, as the concentration of valence band holes is still low. Upon illumination, this concentration increases, and the bands bend in such a way that there is a driving force for the holes to be transferred into solution. This transfer occurs through the oxidation of $BnNH_2$. This can be seen in the LSV, where the onset starts at much more negative potentials (slightly more negative than –

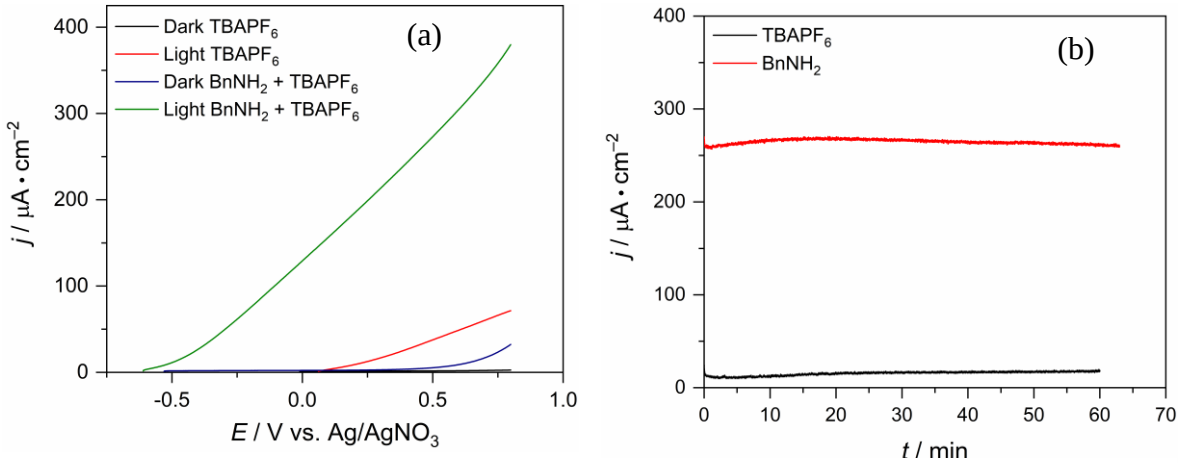

Figure 3.3: Linear sweep voltammograms (a) and bulk electrolysis traces (b) of MeCN/$TBAPF_6$ electrolyte and $BnNH_2$ solutions. The total current passed for the electrolyte only bulk electrolysis in (b) is 3% of that observed for the bulk electrolysis conducted in the presence of 500 mM $BnNH_2$. The applied potential for the bulk electrolysis was 0.4 V vs Ag/$AgNO_3$.

0.5 V vs $Ag/AgNO_3$) than in any of the other experiments. These LSV data demonstrate that $CuWO_4$ is a photoelectrocatalyst for $BnNH_2$ oxidation in nonaqueous conditions.

To obtain the Faradaic efficiency of $BnNH_2$ oxidation on $CuWO_4$, a bulk electrolysis experiment was conducted (Figure 3.4 (b)). In this experiment, a constant potential is held while the current is measured. The solution is stirred during this experiment so that there is always substrate near the surface to react (i.e. the rate of the reaction is not diffusion-limited). The potential chosen for the electrolysis was 0.4 V vs $Ag/AgNO_3$ because the photocurrent observed during the bulk electrolysis of solely electrolyte is low (3%) compared to the photocurrent observed when the 500 mM $BnNH_2$ is added. The photocurrent was stable over the course of the electrolysis in both cases, suggesting that $CuWO_4$ is stable under these conditions. The expected oxidation reaction, based off previous literature, was expected to be $BnNH_2$ being oxidized by 2 e^- to form *N*-benzylidenebenzylamine (*N*-BB, Figure 3.5).[13–16]

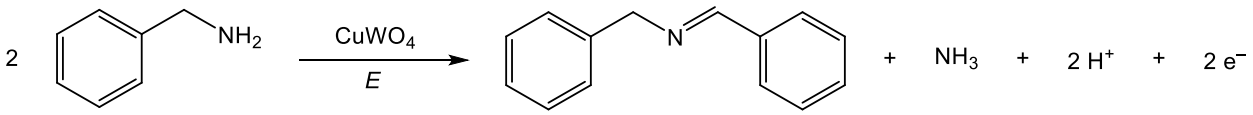

Figure 3.5: The $BnNH_2$ oxidation half-reaction expected to occur at the $CuWO_4$ working electrode during illumination and an applied positive bias.

After one Coulomb of charge had passed during the bulk electrolysis the reaction was stopped. A ^1H NMR spectrum was then collected with 1 mM of dichloromethane as the internal standard (Figure 3.6). Since the reaction was not conducted with deuterated MeCN, solvent suppression was carried out to allow for data analysis. The *N*-BB product was indeed observed and was obtained with 75 ± 16% Faradaic efficiency over two trials. The formation of *N*-BB was also verified with the use of a gas chromatography – mass spectrometry (GC-MS). Since salts are not recommended for injection into GC-MS instruments, an aliquot of the sample was prepared for

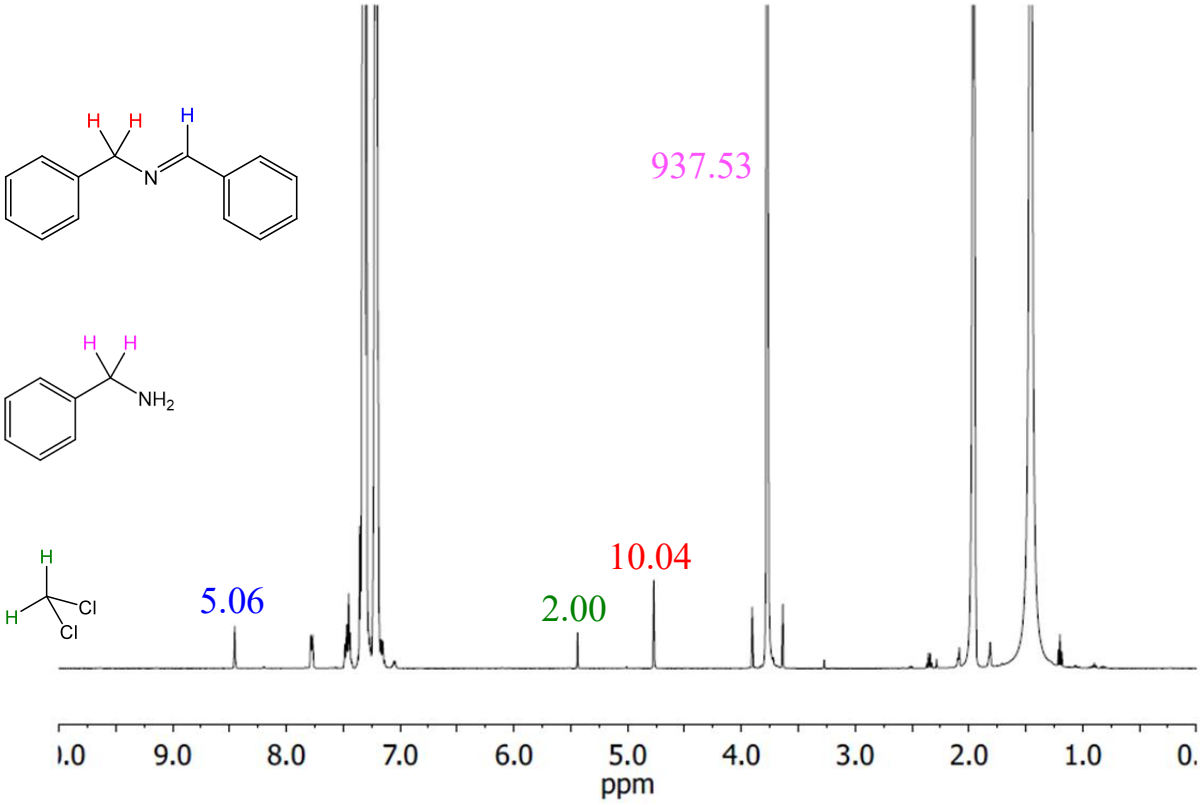

Figure 3.6: ^{1}H NMR spectrum of a post-electrolysis solution of 500 mM $BnNH_2$ in 100 mM $TBAPF_6$ in MeCN where $CuWO_4$ was employed as the photoelectrocatalyst and 1.0 C of charge had passed. Each integration value is colored corresponding to the proton(s) it represents in the structures on the left.

GC-MS injection using the following method: diethyl ether was added to the solution aliquot to cause the $TBAPF_6$ to precipitate. The solid $TBAPF_6$ was filtered and then the aliquot was extracted 3x with diethyl ether to remove the products out of the acetonitrile layer (the compounds are more soluble in ether than acetonitrile). These extractions were combined and then the diethyl ether was removed with a rotary evaporator. Acetonitrile was then added to the resulting oil. A portion of this solution was then diluted with more MeCN and injected into the GC-MS (Figure 3.7). The GC-MS trace showed only two compounds, which were both identified by the GC-MS software and control experiments to be the $BnNH_2$ starting material and the *N*-BB product.

Another way to verify stability of the $CuWO_4$ electrode was to run post-electrolysis LSV experiments. Any major changes in the current response would be indicative of changes to the electrode material (e.g. degradation) during the electrolysis. The data for the post-electrolysis LSV

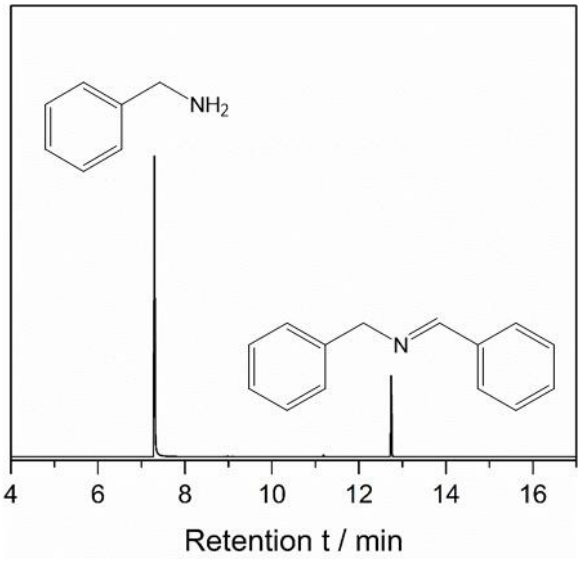

Figure 3.7: GC-MS trace of a post-electrolysis solution of 500 mM $BnNH_2$ in 100 mM $TBAPF_6$ in MeCN where $CuWO_4$ had been employed as the photoelectrocatalyst and 1.0 C of charge had passed.

experiments do not substantially differ from those taken pre-electrolysis, further supporting the stability of the $CuWO_4$ during photoelectrocatalytic oxidation reactions (Figure 3.8). While the photocurrent in the post-electrolysis LSV in the presence of $BnNH_2$ is slightly higher than that for the pre-electrolysis solution, and the photocurrent in the pre-electrolysis LSV with only electrolyte is slightly higher than that for the post-electrolysis solution, this can likely be due to minor differences in power density experienced by the electrode.

3.4 Photoelectrocatalytic Oxidation of *N*-methylbenzylamine on $CuWO_4$ Photoelectrodes

After demonstrating that $CuWO_4$ is a photoelectrocatalyst for nonaqueous benzylamine oxidation, observing how the reaction rate, Faradaic efficiency, and selectivity would change upon addition of a methyl group to the nitrogen of $BnNH_2$ was pursued. It was hypothesized that addition of the methyl group on *N*-methylbenzylamine (*N*-$MeBnNH_2$) could hinder the reaction rate due to adding some bulk near onto the nitrogen, whose one electron oxidation is thought to be the rate determining step in $BnNH_2$ oxidation, while also giving rise to the possibility of different oxidation products due to the

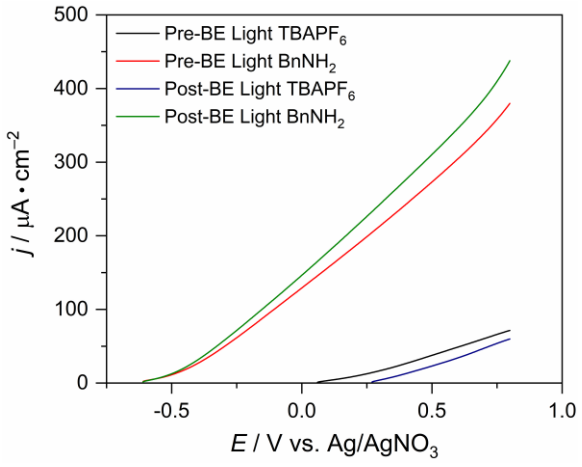

Figure 3.8: Illuminated pre- and post-bulk electrolysis (Pre-BE and Post-BE) linear sweep voltammograms of a $CuWO_4$ electrode in 100 mM $TBAPF_6$ in MeCN with 500 mM $BnNH_2$. The bulk electrolysis conducted in between the LSV experiments passed 1.0 C at 0.4 V vs $Ag/AgNO_3$ under illumination.

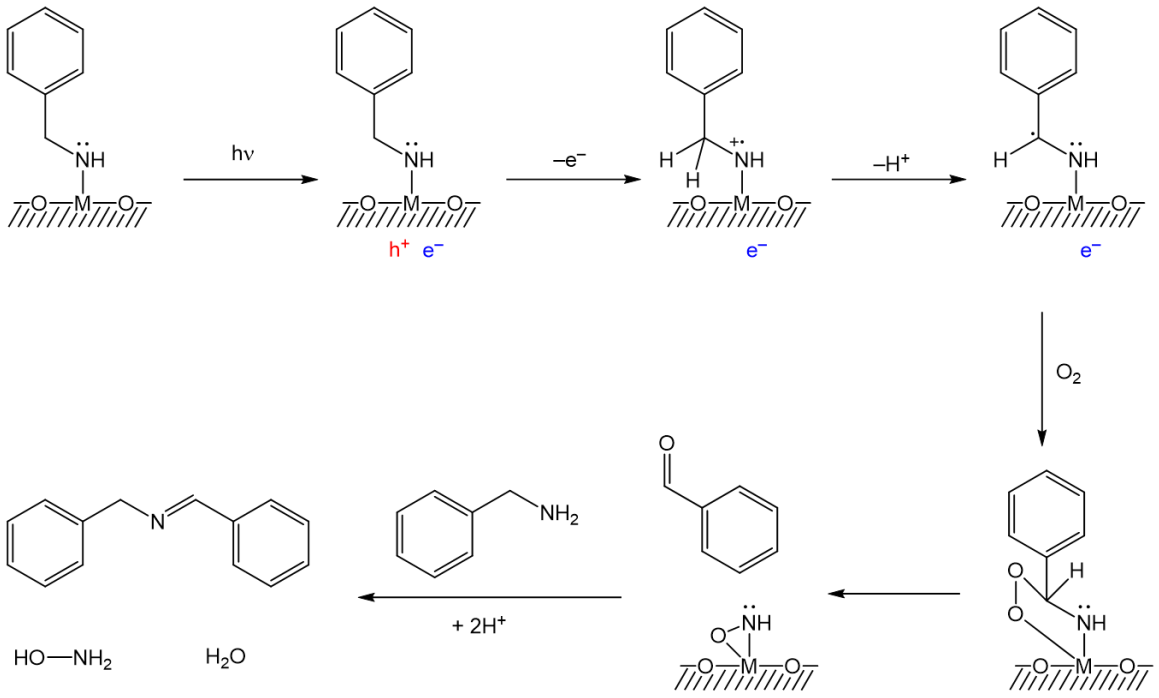

Figure 3.9: Proposed photocatalytic oxidation mechanism of $BnNH_2$ on a metal oxide surface. After $BnNH_2$ adsorbs to the catalyst surface, the first step is the absorption of light by the metal oxide, creating an electron (e^-) and hole (h^+) pair. The hole oxidizes the nitrogen atom of the $BnNH_2$ by one electron, generating a nitrogen radical cation. This makes the neighboring benzylic hydrogen atoms more acidic. One is abstracted, leaving behind a neutral nitrogen atom and a neutral carbon-centered radical at the benzylic position. Next, O_2 binds to the carbon-centered radical and the metal. This forms a five-membered ring intermediate that has its oxygen-oxygen bond and metal nitrogen bond broken and replaced with an oxygen-nitrogen bond and oxygen-carbon bond. This releases benzaldehyde into solution, which can then undergo a condensation reaction with a $BnNH_2$ molecule to generate the *N*-BB product.

abstractable hydrogens on this methyl group. The reason these methyl hydrogens are important is because after the first and rate-determining step in the proposed mechanism for $BnNH_2$ oxidation on metal oxides (a one electron oxidation of the nitrogen) the abstraction of a benzylic hydrogen follows (Figure 3.9).[16] With both the benzylic and methyl positions to abstract hydrogens from, it is possible that multiple products would result if both pathways are accessible. The acidity of the benzylic protons is much higher than the methyl protons due to the resonance stabilization of the neutral carbon-centered radical by the neighboring phenyl group and nitrogen atom. A radical on the methyl group would have no stabilization other than resonance with the neighboring nitrogen atom. Further instability of the methyl carbon-centered radical is incurred due to it being a primary carbon-centered radical (secondary or tertiary radicals are more stable).

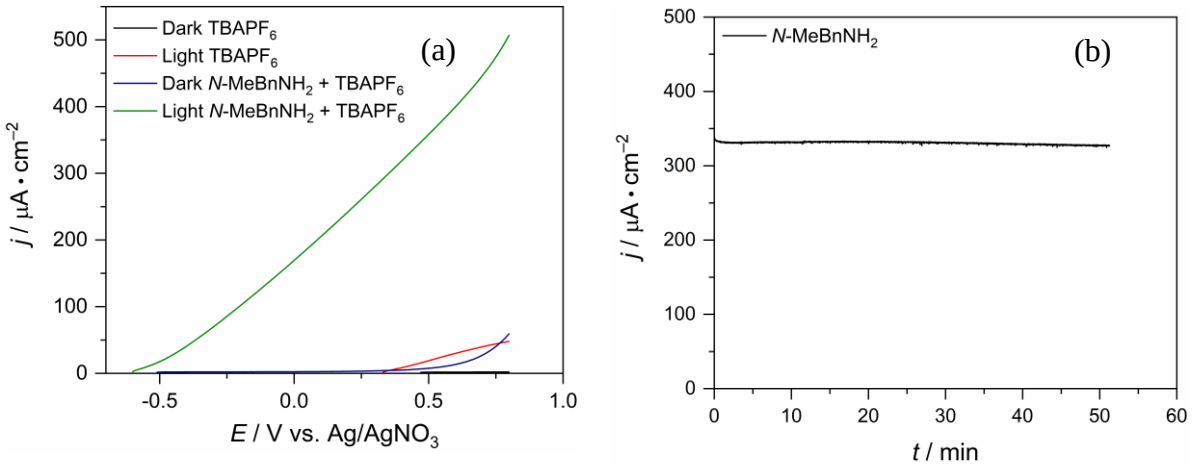

Figure 3.10: Linear sweep voltammograms (a) and bulk electrolysis traces (b) of MeCN/$TBAPF_6$ electrolyte and 500 mM *N*-$MeBnNH_2$ solutions. Bulk electrolysis conducted under blue LED illumination at 0.4 V vs $Ag/AgNO_3$.

The LSV traces for *N*-$MeBnNH_2$ are similar to those for $BnNH_2$ (Figure 3.10 (a)). With the highest photocurrent and most negative onset of photocurrent for the illuminated solution with 500 mM *N*-$MeBnNH_2$, $CuWO_4$ was demonstrated to be a photoelectrocatalyst for *N*-$MeBnNH_2$ oxidation. The onset of the photocurrent was importantly no different than that seen for $BnNH_2$ oxidation (~ –0.60 V vs $Ag/AgNO_3$), which demonstrates that the kinetics of *N*-$MeBnNH_2$ oxidation are not hindered by the methyl group present on the nitrogen. It was hypothesized that the steric bulk of this methyl group would slow the oxidation rate compared to $BnNH_2$, but the LSV data show that this hypothesis was incorrect. The illuminated bulk electrolysis experiment (Figure 3.10 (b)) showed stable photocurrent over the ~55 minutes it took to pass one Coulomb of charge. The solution from a bulk electrolysis run at 0.2 V vs $Ag/AgNO_3$ (to ensure no electrolyte oxidation) until 12.7 C had been passed (to ensure that products generated at slower rates had higher concentrations) exhibited signals for five different products in the GC-MS trace (Figure 3.11). Benzaldehyde, *N*-BB, and toluene were present in the largest quantities, while there were small concentrations of *N*,*N*-dimethylbenzylamine (the *N*-methylated starting material) and *N*-methyl-1-phenylmethanimine (the dehydrogenated starting material with a double bond between the nitrogen and benzylic carbon). Other than toluene, all of these products can be accounted for

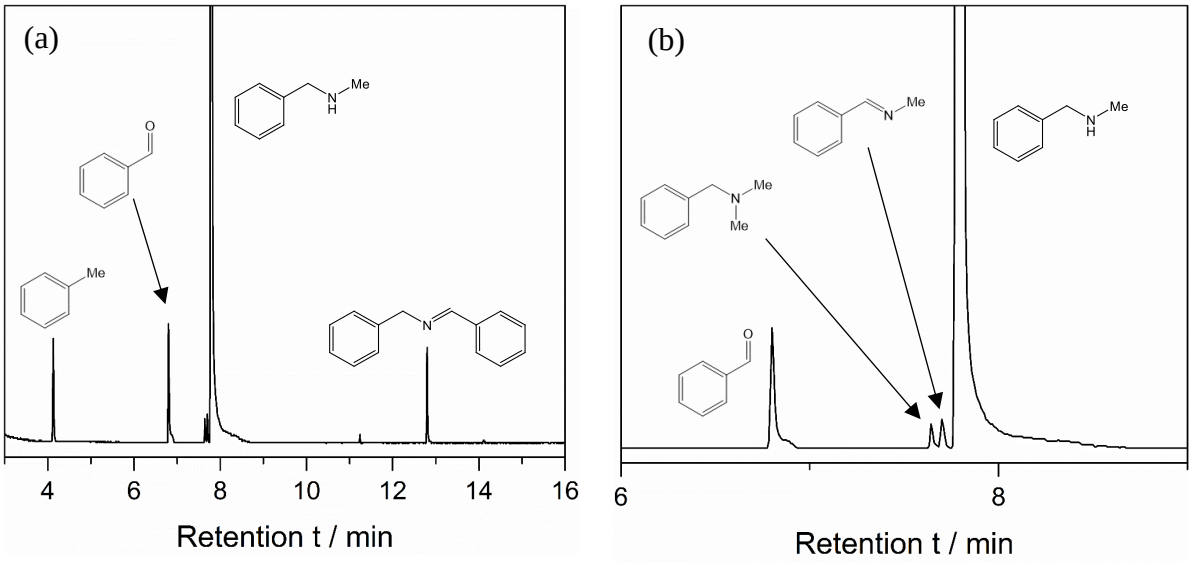

Figure 3.11: GC-MS trace of a post-electrolysis solution of 500 mM *N*-MeBnNH$_2$ in 100 mM TBAPF$_6$ in MeCN where CuWO$_4$ had been employed as the photoelectrocatalyst and 12.7 C of charge had passed after applying a potential of 0.2 V vs Ag/AgNO$_3$ for the necessary time (a). Minor products are more clearly exhibited when zooming in between retention times 6-9 minutes (b).

by considering both the abstraction of a benzylic proton or terminal methyl proton as part of the reaction mechanism and how these products could react with each other (Figure 3.12). If a hydrogen is abstracted from the benzylic position then the *N*-methyl-1-phenylmethanimine is made, which is seen at a retention time of about 7.8 minutes, eluting just before the starting material. This reacts further to gives benzaldehyde (seen at a retention time of about 6.8 minutes) and methylamine (not seen in the GC-MS trace, likely due to elution with the solvent on account of its low molecular weight). If a proton is abstracted from the terminal methyl position, then the products are formaldehyde and BnNH$_2$. The BnNH$_2$ can then react with the benzaldehyde made from the other

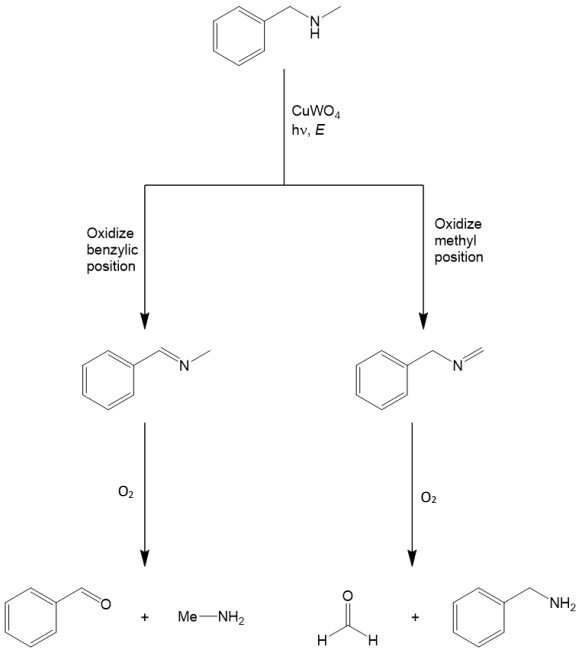

Figure 3.12: Two different routes in the photoelectrocatalytic oxidation of *N*-MeBnNH$_2$, with the left route undergoing proton abstraction from the benzylic position and the right route going through a proton abstraction of the terminal methyl group. These two different imines react with O$_2$ to give different products.

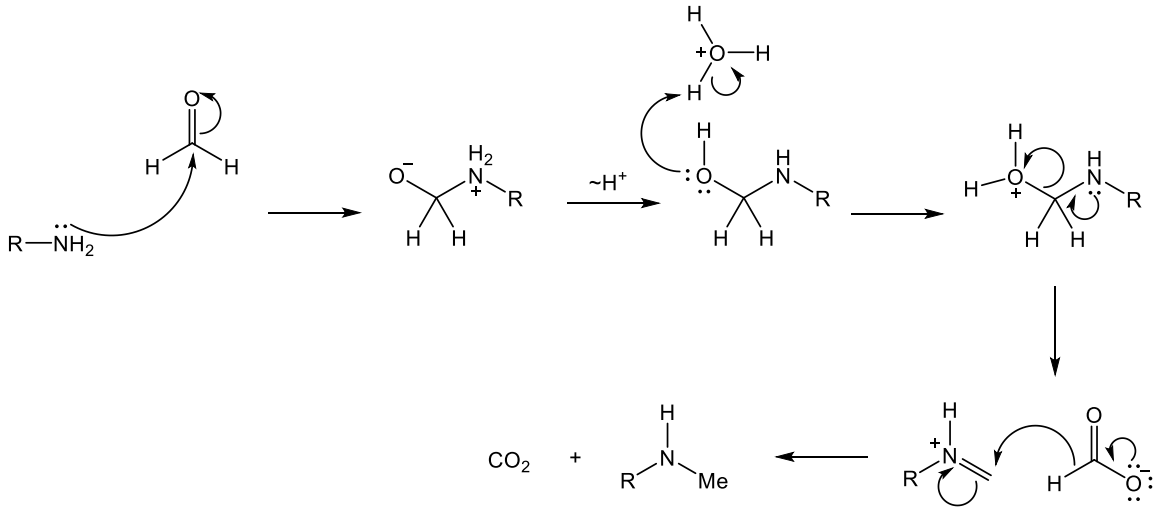

Figure 3.13: Example of an Eschweiler-Clarke reaction transforming a primary amine into a methylated secondary amine.

reaction pathway to give *N*-BB, which is seen in the GC-MS trace at a retention time of about 12.9 minutes. Finally, the *N*,*N*-dimethylbenzylamine can be accounted for by considering a possible Eschweiler-Clarke reaction (Figure 3.13). In this reaction, a primary or secondary amine reacts with first, formaldehyde, and second, formic acid, which gives a methylated amine. While no formic acid was seen in the GC-MS trace, it is possible that formic acid is produced by the oxidation of formaldehyde at the electrode and is then immediately used for this reaction. Metal oxides have been shown to oxidize formaldehyde selectively to formic acid, though in air at >100 °C and in the gas phase.[17–20]

The high quantity of toluene observed in the GC-MS is unable to be explained at this time. There has been a report, however, that toluene was the main by-product detected in the di-methlyation of benzylamine with formaldehyde – a reaction that is likely occurring during the photoelectrocatalytic oxidation of *N*-MeBnNH$_2$ given the *N*,*N*-dimethylbenzylamine detected by GC-MS after electrolysis.[21] While the mechanism for the formation of toluene was not outlined in this report, a similar reaction could be occurring in the photoelectrochemistry on $CuWO_4$ to generate toluene as a major reaction product.

3.5 Conclusions

It has been demonstrated that $CuWO_4$ can act as a photoelectrocatalyst for nonaqueous benzylamine and *N*-methylbenzylamine oxidation. The $CuWO_4$ electrodes, synthesized by a spray pyrolysis method, maintained stable photocurrent over the course of all bulk electrolysis experiments conducted, demonstrating their stability under photooxidative conditions. The onset for $BnNH_2$ oxidation photocurrent occurs at a potential ~700 mV more negative than electrolyte oxidation, allowing for electrolysis experiments to be carried out with no competing electrolyte oxidation. This is not always the case with metal oxides, as WO_3 has been shown to oxidize many common aqueous electrolyte anions during water oxidation, giving rise to unavoidable parasitic reactions.[22,23] The only product observed by both GC-MS and ^{1}H NMR was *N*-benzylidenebenzylamine, which was the expected product based on reports of benzylamine oxidation on other metal oxides.[13–16] The Faradaic efficiency for $BnNH_2$ photoelectrocatalytic oxidation on $CuWO_4$ was 75 ± 16%.

There were five products observed from *N*-$MeBnNH_2$ oxidation. With the second step of the oxidation mechanism being the abstraction of a proton from a neighboring carbon, the addition of a methyl group on the nitrogen adds a second position from which to abstract protons at this point in the mechanism. This leads to two different reaction pathways taken after the initial one electron oxidation of the nitrogen atom. Products from both pathways were observed, though products representing the pathway taken after abstraction of a proton from the methyl position were observed in lower concentrations. Notably, the onset of photocurrent for *N*-$MeBnNH_2$ oxidation is nearly identical to that of that seen for $BnNH_2$ oxidation. This means that the extra steric bulk added by the methyl group of *N*-$MeBnNH_2$ did not hinder the kinetics of oxidation.

Overall, this was a promising venture into organic oxidations on $CuWO_4$ – a catalyst used by the Bartlett lab nearly exclusively for water oxidation up until these experiments. After seeing the much more negative onset of photocurrent for amine oxidation compared to electrolyte oxidation, the next step was to remove the external potential source and attempt organic oxidations photocatalytically on $CuWO_4$ powders. Is an external positive bias required to carry out photocatalytic oxidations on $CuWO_4$? If not, what are the rate and selectivity of $BnNH_2$ oxidation on $CuWO_4$ powders? How recyclable are these powders during photocatalysis? These are questions that were inspired by this work and are answered in Chapter 4 of this thesis.

3.6 Experimental

Materials and Methods

Benzylamine (99%), *N*-benzylidenebenzylamine (99%), copper (II) chloride, and sodium hydroxide (ACS reagent, ≥97.0%) were purchased from Sigma-Aldrich. Acetonitrile (Certified ACS), dichloromethane (Certified ACS), ethanol (200 proof), ammonium metatungstate (Strem Chemical, 99.9%+%-W), *N*-methylbenzylamine (97%), silver nitrate Alfa Aesar, ACS, 99.9% metals basis), and hydrochloric acid (Certified ACS Plus, 36.5 to 38.0%) were purchased from Fisher. Tetrabutylammonium hexafluorophosphate (>98.0%) was purchased from TCI. Silver print was purchased from Jameco. Epoxy was purchased from R.S. Hughes (Loctite Hysol 1C off-white two-part epoxy adhesive - 4 oz kit, part no. 1373425, Henkel). Acetonitrile-d_3 was purchased from Cambridge Isotope Laboratories. Benzylamine was vacuumed distilled over NaOH and stored on sieves under N_2. The $TBAPF_6$ was recrystallized from 200 proof ethanol. All other reagents were used as received. Fluorinated tin oxide coated glass was purchased from Pilkington Glass (TEC 15). Blue LEDs were ordered from Creative Lighting Solutions (sapphire blue flex LED strip 5050 – high density – 12VDC, part #CL-FRS5050-12WP-12V). $Ag/AgNO_3$

nonaqueous reference electrodes with Teflon tips were purchased from CHI and filled with 100 mM $TBAPF_6$ and 10 mM $AgNO_3$ in acetonitrile. Platinum 52mesh was purchased from Sigma-Aldrich.

Materials Characterization

Powder X-ray diffraction data were collected on a Bruker D8 Advance diffractometer equipped with a graphite monochromator, a Lynx-Eye detector, and parallel beam optics using Cu Kα radiation (λ=1.54184 Å). Patterns were recorded at a step size of 0.02° per step at a scan rate of 0.25 s per step. This XRD was not equipped with a sample spinner. A Zeiss LEO 1455VP scanning electron microscope was used to image the films at a working distance of 5 mm. A Varian Cary 5000 spectrophotometer equipped with an external integration sphere accessory was used for UV-vis measurements. Spectra were collected in reflectance mode and transformed into absorbance using the Kubelka-Monk function. Barium sulfate was used as a 100% reflectance standard.

$CuWO_4$ Photoelectrode Preparation

A spray pyrolysis method was used to synthesize $CuWO_4$ films. A solution 10 mM in Cu^{2+} (using $CuCl_2$) and 2 mM in HCl was added to a solution 10 mM in W^{6+} (using ammonium metatungstate that was then sprayed onto fluorinated tin oxide glass (FTO) slides 1 cm in width and approximately 2.5 cm in length. The HCl is included to prevent the precipitation of copper. These slides were on a hot plate set to 275 °C and had part of their FTO sides covered such that some of the FTO was left clean. Having a portion of the slide left as clean FTO is necessary so that a copper wire can be attached to the slide later. The spray was applied in 1 s pulses that were swept horizontally over the FTO to achieve an even coat. Nitrogen was used as the carrier gas for

the spray. In between each 1 s pulse of spray application there was a 5 s delay to allow for solvent evaporation before the next spray was started. After 100 sprays, the films were placed into a furnace, heated to 550 °C (ramp times up to 550 °C and down to room temperature were 1 hour each), and held for 1 hour to anneal the material to crystalline $CuWO_4$. After the annealing process, a piece of copper wire was attached to the remaining clean FTO section of the slide with conductive silver paint. The silver paint was allowed to dry overnight before a glass rod was placed over the copper wire and attached to the slide with epoxy to complete the electrode (Figure 3.1 (c)). The epoxy was placed on the electrode to allow for a 1 x 1 cm^2 area of $CuWO_4$ to be exposed.

Photoelectrocatalytic Reactions

All electrochemistry was conducted on a CHI660 or CHI1000 potentiostat. All electrochemical reactions were carried out in a two-compartment cell with a working compartment side that had a quartz window. A Nafion membrane was c-clamped between the two compartments. Photoelectrocatalytic experiments were illuminated with three blue LED strips (λ_{max}=465 nm) with a power density of 30-45 mW • cm^{-2}. The LED strips were held up by wrapping them around a test tube rack. The quartz window of the photoelectrochemical cell was placed up against the LEDs to achieve this power density. The open circuit potential was used as the starting potential for all linear sweep voltammetry experiments. The electrolyte in all experiments was 100 mM $TBAPF_6$ in acetonitrile. The working electrode was always $CuWO_4$, the reference was a silver wire placed in 100 mM $TBAPF_6$ in acetonitrile with 10 mM $AgNO_3$, and the counter was platinum mesh. All linear sweep voltammograms were collected at a scan rate of 20 mV • s^{-1} with the CHI software set to a sensitivity of 10^{-3} amperes. All bulk electrolysis experiments were run at either 0.4 or 0.2 V vs $Ag/AgNO_3$. The amine concentration in all experiments was 500 mM. All GC-MS data were

collected on a Shimadzu QP-2010 GC-MS. Sample injection volumes of 5 µL were used. The column attached to the instrument was a DB-5 ms column with a length of 30 m, a thickness of 0.25 µm, and a diameter of 0.25 mm. The temperature for GC-MS runs was started at 50 °C, held for 3 minutes, then ramped up to 300 °C at a rate of 20 °C • min^{-1}, and then held for 10 minutes before ending the run.

Faradaic Efficiency Measurements for $BnNH_2$ Oxidation

A bulk electrolysis experiment was allowed to run until 1 Coulomb of charge had passed. Then 540 µL of the working compartment solution was placed in an NMR tube that contained 60 uL of a standard solution of 10 mM dichloromethane in acetonitrile (giving a final concentration of 1 mM DCM in the NMR sample). Solvent suppression was used when collecting the ^{1}H NMR spectrum. Next, the integration value for the DCM was compared to that for both the benzylic protons and imine proton on *N*-BB. See the experimental section in Chapter 2 of this thesis for an example calculation. ^{1}H NMR data were collected on a Varian MR400 NMR spectrometer equipped with a Varian 5 mm PFG AutoX Dual Broadband probe. All NMR data was processed in MestReNova software.

3.7 References

[1] Li, C.; Zhao, X.; Wang, A.; Huber, G. W. and Zhang, T. Catalytic Transformation of Lignin for the Production of Chemicals and Fuels. *Chem. Rev.* **2015**, *115*, 11559-11624.

[2] Coseri, S.; Biliuta, G. and Simionescu, B. C. Selective oxidation of cellulose, mediated by *N*-hydroxyphthalimide, under a metal-free environment. *Polym. Chem.* **2018**, *9*, 961-967.

[3] Bosque, I.; Magallanes, G.; Rigoulet, M.; Kärkäs, M. D. and Stephenson, C. R. J. Redox Catalysis Facilitates Lignin Depolymerization. *ACS Cent. Sci.* **2017**, *3*, 621-628.

[4] Magallanes, G.; Kärkäs, M. D.; Bosque, I.; Lee, S.; Maldonado, S. and Stephenson, C. R. J. Selective C–O Bond Cleavage of Lignin Systems and Polymers Enabled by Sequential Palladium-Catalyzed Aerobic Oxidation and Visible-Light Photoredox Catalysis. *ACS Catal.* **2019**, *9*, 2252-2260.

[5] Werpy, T. and Pertersen, G. *Top Value Added Chemicals from Biomass: Volume I – Results of Screening for Potential Candidates from Sugars and Synthesis Gas*; DOE/GO-102004-1992; U.S. Department of Energy: Oak Ridge, TN, 2004.

[6] Yourey, J. E. and Bartlett, B. M. Electrochemical Deposition and Photoelectrochemistry of $CuWO_4$, a Promising Photoanode for Water Oxidation. *J. Mater. Chem.* **2011**, *21*, 7651-7660.
[7] Yourey, J. E.; Kurtz, J. B. and Bartlett, B. M. Water Photooxidation on a $CuWO_4$-WO_3 Composite Electrode in the Presence of $[Fe(CN)_6]^{3-}$: toward Z-scheme Water Splitting at Zero Bias. *J. Phys. Chem. C* **2012**, *116*, 3200-3205.
[8] Yourey, J. E.; Kurtz, J. B.; Bartlett, B. M. Structure, Optical Properties, and Magnetism of the Full $Zn_{1-x}Cu_xWO_4$ ($0 < x < 1$) Composition Range. *Inorg. Chem.* **2012**, *51*, 10394-10401.
[9] Yourey, J. E.; Pyper, K. J.; Kurtz, J. B.; Bartlett, B. M. Chemical Stability of $CuWO_4$ for Photoelectrochemical Water Oxidation. *J. Phys. Chem. C.* **2013**, *117*, 8708-8718.
[10] Pyper, K. J.; Yourey, J. E.; Bartlett, B. M. Reactivity of $CuWO_4$ in Photoelectrochemical Water Oxidation is Dictated by a Mid-gap Electronic State. *J. Phys. Chem. C.* **2013**, *117*, 24726-24732.
[11] Lhermitte, C. R.; Bartlett, B. M. Advancing the Chemistry of $CuWO_4$ for Photoelectrochemical Water Oxidation. *Acc. Chem. Res.* **2016**, *49*, 1121-1129.
[12] Lhermitte, C. R.; Verwer, J. G.; Bartlett, B. M. Improving the Stability and Selectivity for the Oxygen-Evolution Reaction on Semiconducting WO_3 Photoelectrodes with a Solid-State FeOOH Catalyst. *J. Mater. Chem. A* **2016**, *4*, 2960-2968.
[13] Furukawa, S.; Ohno, Y.; Shishido, T.; Teramura, K. and Tanaka, T. Reaction Mechanism of Selective Photooxidation of Amines over Niobium Oxide: Visible-Light-Induced Electron Transfer between Absorbed Amine and Nb_2O_5. *J. Phys. Chem. C* **2013**, *117*, 442-450.
[14] Furukawa, S.; Ohno, Y.; Shishido, T.; Teramura, K. and Tanaka, T. Selective Amine Oxidation Using Nb_2O_5 Photocatalyst and O_2. *ACS Catal.* **2011**, *1*, 1150-1153.
[15] Yuan, B.; Chong, R.; Zhang, B.; Li, J.; Liu, Y. and Li, C. Photocatalytic aerobic oxidation of amines to imines on $BiVO_4$ under visible light irradiation. *Chem. Commun.* **2014**, *50*, 15593-15596.
[16] Lang, X.; Ji, H.; Chen, C.; Ma, W. and Zhao, J. Selective Formation of Imines by Aerobic Photocatalytic Oxidation of Amines on TiO_2. *Angew. Chem. Int. Ed.* **2011**, *50*, 3934-3937.
[17] Popova, G. Y.; Andrushkevich, T. V.; Semionova, E. V.; Chesalov, Y. A.; Dovlitova, L. S. Rogov, V. A. and Parmon, V. N. Heterogeneous selective oxidation of formaldehyde to formic acid on V/Ti oxide catalysts: The role of vanadia species. *J. Mol. Catal. A: Chem.* **2008**, *283*, 146-152.
[18] Danilevich, E. V.; Popova, G. Y.; Andrushkevich, T. V.; Chesalov, Y. A.; Kaichev, V. V.; Saraev, A. A. and Plyasova, L. M. Preparation, active component and catalytic properties of supported vanadium catalysts in the reaction of formaldehyde oxidation to formic acid. *Stud. Surf. Sci. Catal.* **2010**, *175*, 463-466.
[19] Ai, M. The Reaction of Formaldehyde on Various Metal Oxide Catalysts. *J. Catal.* **1983**, *83*, 141-150.
[20] Danilevich, E. V.; Popova, G. Y.; Andrushkevich, T. V.; Kaichev, V. V.; Danilova, I. G.; Chesalov, Y. A.; Rogov, V. A.; Bukhtiyarov, V. I. and Parmon, V. N. Selective oxidation of formaldehyde to formic acid over supported vanadia catalysts. *Appl. Catal. A: General* **2014**, *475*, 98-108.
[21] Volf, J.; Matějovič, K. and Petrisko, M. Reductive Methylation of Benzylamine with Formaldehyde on Raney Ni and Pd/C Catalysts. *Chem. Listy* **2000**, *94*, 456-458.
[22] Mi, Q.; Zhanaidarova, A.; Brunschwig, B. S.; Gray, H. B. and Lewis, N. S. A quantitative assessment of the competition between water and anion oxidation at WO_3 photoanodes in acid aqueous electrolytes. *Energy Environ. Sci.* **2012**, *5*, 5694-5700.
[23] Mi, Q.; Coridan, R. H.; Brunschwig, B. S.; Gray, H. B. and Lewis, N. S. Photoelectrochemical oxidation of anions by WO_3 in aqueous and nonaqueous electrolytes. *Energy Environ. Sci.* **2013**, *6*, 2646-2653.

Chapter 4 $CuWO_4$ as a Photocatalyst for Room Temperature Aerobic Benzylamine Oxidation

Portions of this chapter have been published:

Proctor, A. D.; Panuganti, S. and Bartlett, B. M. $CuWO_4$ as a Photocatalyst for Room Temperature Aerobic Benzylamine Oxidation. *Chem. Commun.* **2018**, *54*, 1101-1104.

4.1 Introduction

Using light and molecular oxygen as a means to carry out organic oxidation reactions is receiving greater attention in the aim to increase their atom- and energy-efficiency. Many carbon-carbon and carbon-nitrogen bond forming reactions have been catalyzed by organic[1] and transition metal[2,3] photoredox catalysts. Although the design principles are worthy of exploration, there are factors that limit the feasibility of introducing these catalysts in large-scale applications. Most organic photocatalysts absorb only ultraviolet light, making the reactions more energy intensive. Visible light absorbing transition metal catalysts require expensive metals, most commonly ruthenium or iridium. Also, both catalyst types are used for homogeneous reactions, which makes their separation from the solution-phase product difficult. Metal oxides, on the other hand, are inexpensive, very stable, visible light responsive, and easily filtered from the product. Many metal oxides have recently shown promise as photocatalysts in organic reactions.[4–12]

Our group and others have shown that copper (II) tungstate ($CuWO_4$) can carry out visible light driven photoelectrocatalytic water oxidation,[13–20] and the previous chapter in this thesis demonstrated that $CuWO_4$ can act as a photoelectrocatalyst for benzylamine oxidation, but its propensity to catalyze controlled organic oxidations *photocatalytically* has been unexplored. A

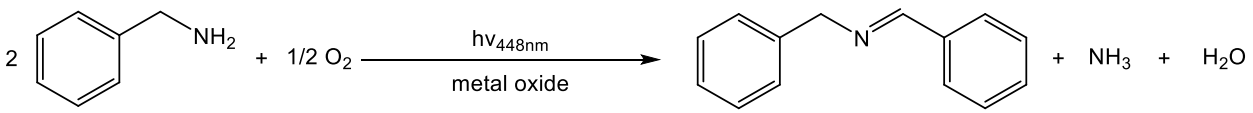

Figure 4.1: The balanced reaction for the photocatalytic oxidation of benzylamine on a metal oxide photocatalyst conducted in air with acetonitrile solvent.

typical dye degradation reaction has been reported[21] but dye degradation reactions are not concerned with the selective formation of products, as they have multiple oxidation and reduction pathways that lead to degradation. Here, the first example of photocatalytic benzylamine ($BnNH_2$) oxidation to *N*- benzylidenebenzylamine (*N*-BB) under aerobic conditions in acetonitrile (MeCN) is reported (Figure 4.1).

As discussed in the introduction of the previous chapter, $BnNH_2$ is being used as a starting substrate to investigate organic oxidations on visible-light-absorbing metal oxides with the goal of navigating towards methods to oxidize biomass-derived substrates, such as 5-hydroxymethylfurfural (5-HMF). Oxidation of these compounds include the release of protons, which can be reduced to form hydrogen gas as a product, which is a valuable energy source. The oxidation product of the biomass-derived substrate also yields a more valuable product than its starting material. For example, 5-HMF can be oxidized to its dicarboxylic acid, which can be used as a monomer for a variety of polymers. Biomass-derived compounds are generally heavily hydroxylated, with the one-electron oxidation of the hydroxyl groups on these compounds being the rate determining step of the oxidation. Beginning with benzylamine allows for the investigation of the one-electron oxidation of heteroatoms, but with nitrogen being less electronegative, it presents itself as a more thermodynamically facile oxidation. These $BnNH_2$ oxidation reactions were carried out in MeCN to avoid competing water oxidation.

Benzylamine is a model substrate to investigate the photocatalytic reactivity of $CuWO_4$ in organic oxidations for two reasons: 1) the standard electrode potential of this reaction is 0.86 V vs NHE in acetonitrile,[22] which is well above the valence band maximum of $CuWO_4$ (2.8 V vs RHE

in water[15]) and 2) this particular photocatalytic reaction has also been reported on other metal oxides ($BiVO_4$[5], Nb_2O_5[9,23], Ta_2O_5[24], and TiO_2[8,25,26]), where molecular oxygen acts as the sacrificial oxidant. There is therefore precedent that metal oxides can carry out proton-coupled-electron-transfer redox half reactions. Oxygen reduction should be feasible for the photogenerated electrons of $CuWO_4$ since the reduction potential for O_2 to H_2O in acetonitrile (1.61 V vs NHE[27]) should be much more positive than the conduction band minimum for $CuWO_4$ (~0.4 V vs NHE in water[15]). Here, the reactivity of $CuWO_4$ is compared to that of the ternary metal oxide $BiVO_4$ using a custom-built blue LED reactor. $BiVO_4$ was chosen as a comparison due to its relatively more common utilization as a photocatalyst.

4.2 Custom LED Reactor Details

The LED reactor was designed by multiple members of the lab and ultimately constructed by Andrew Breuhaus-Alvarez of the Bartlett group. The main body was cut from a block of aluminum metal. The three pieces of the body served different purposes. The bottom held the five LED chips. The chips were made by soldering a royal blue LUXEON Rebel High Power LED (purchased from Mouser Electronics, Mouser Part#: 997-LXML-PR02-A900) onto a SinkPAD-II Luxeon Rebel Star printed circuit board (Part#: 1903). These LEDs have an emission with a λ_{max} of about 448 nm (Figure 4.2). The electrical connections were soldered on and then the LED array attached to the bottom aluminum plate with liquid electrical tape (North American®). Each portion of the aluminum body had three small holes drilled in them, two on one side and one on the opposite side. This is to allow three brass rods to be inserted, which hold the three pieces together.

Figure 4.2: Assembly of the custom LED photoreactor. (a-b) Positioning of the rubber septa that the brass rods rest on. (c-d) Placement of the bottom aluminum piece containing the LED chips. The green substance is liquid electrical tape. (e-f) Placement of the 2nd aluminum piece. O-rings surround each of the openings in this piece, which is where the bottoms of the reaction vials and final aluminum piece of the reactor sit. (g-h) The fully assembled photoreactor. (i-j) Placement of 4 mL dram vials into the reactor with and without LEDs turned on. (k) An assembled LED chip, with the LUXEON Rebel LED bulb soldered onto the center of a SinkPAD-II Luxeon Rebel Star printed circuit board.

Once the brass rods were placed in the bottom piece (set on top of rubber septa to raise the assembly slightly off of the stir plate), the second piece of the aluminum body was put on. This second piece has holes in it to allow for the light from the LEDs to shine up to hit the bottom of 4 mL dram vials that hold reactions. O-rings are placed around these holes so that when the dram vials are placed inside the top portion of the body, they are not directly touching the aluminum of the second piece.

This is to prevent heat transfer from the 2nd piece (which may heat up after being illuminated by the high-power LEDs) to the reaction vials.

The third piece was then place on the o-rings resting on the 2nd aluminum piece. This piece is tall enough to fully surround an inserted dram vial. This allows for light that is not absorbed by the photocatalyst to reflect off of the sides of the aluminum body, giving the photocatalyst more chances to absorb the light. The height of this piece allows the light to be used as efficiently as possible. A fan, placed to the side of the assembly, was then turned on to maintain airflow through the designed gaps to keep the LED reactor and the reactions it held cool. Monitoring the temperature of a 2 mL volume of acetonitrile over 3 hours showed the temperature rose from room temperature to 28-29 °C in the first 30 minutes and remained in this range for the next 2.5 hours. The bottom of a dram vial in this setup experiences ~200 $mW \bullet cm^{-2}$ of power density from the blue LEDs.

4.3 Synthesis and Characterization of $CuWO_4$ and $BiVO_4$ Powders

Both $CuWO_4$ and $BiVO_4$ powders were prepared by solid-state syntheses; full experimental details are continued in the experimental section at the end of this chapter. Briefly, wolframite $CuWO_4$ was synthesized by grinding CuO and WO_3 powders for 10 minutes with a mortar and pestle and heating in an oven at 800 °C for 6 hours. Monoclinic scheelite $BiVO_4$ was prepared by the same method, but using $Bi(NO_3)_3 \bullet 5H_2O$ and NH_4VO_3 as the precursors heated to 500 °C for 6 hours. Each synthesis gave aggregates of 1-5 μm particles (Figure 4.3 (a) and (b)) with similar surface areas (1.8 m^2g^{-1} for $CuWO_4$ and 1.3 m^2g^{-1} for $BiVO_4$; obtained by BET analysis of N_2 sorption isotherms). The powder XRD patterns show single phase crystalline wolframite $CuWO_4$ and monoclinic scheelite $BiVO_4$ (Figure 4.3 (c) and (d)). This is especially important for the monoclinic scheelite $BiVO_4$, as tetragonal phase impurities were a concern during synthesis, as the

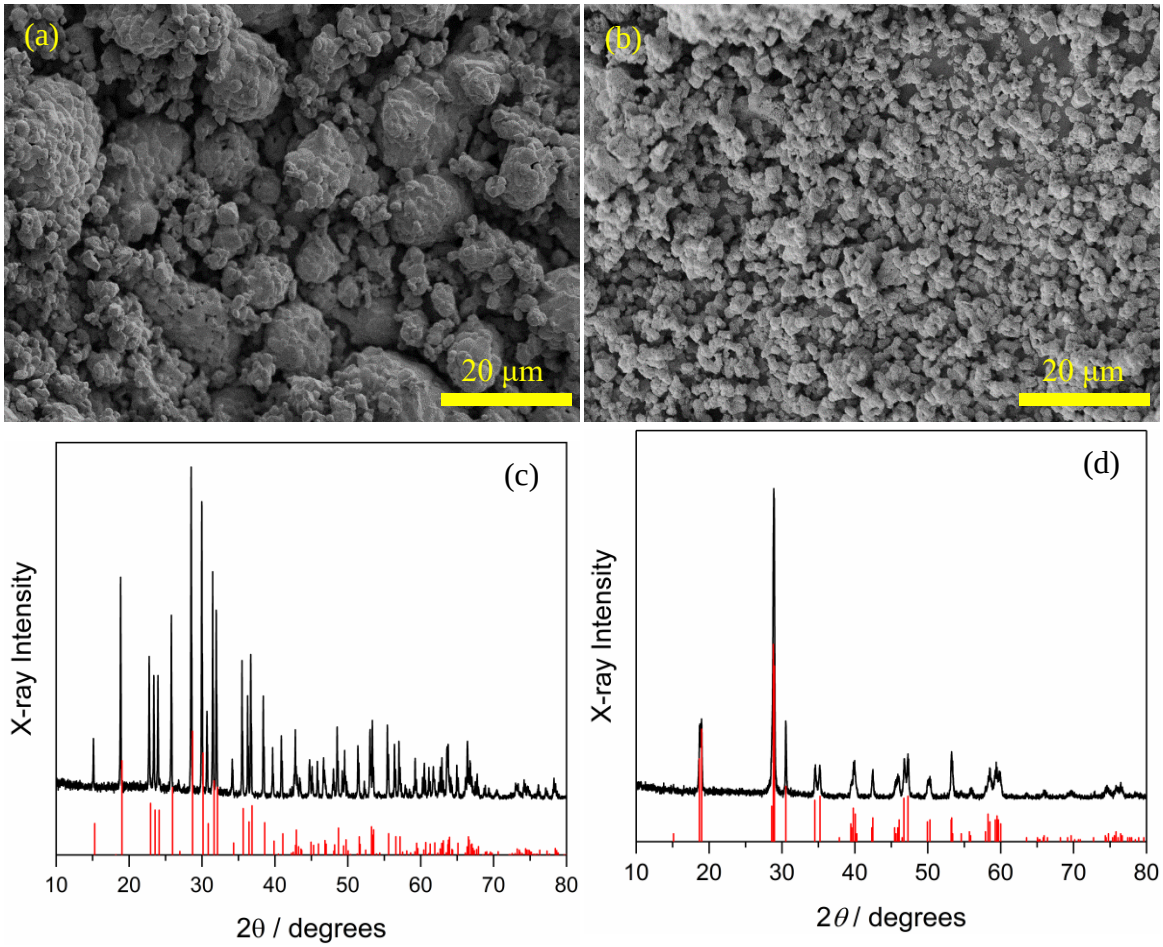

Figure 4.3: Scanning electron micrographs of as-synthesized (a) $CuWO_4$ and (b) $BiVO_4$. Powder X-ray diffraction patterns (black) of as-synthesized $CuWO_4$ (c) and $BiVO_4$ (d). Reference patterns (red) included are ICSD#24339 for $CuWO_4$ and ICSD#31550 for $BiVO_4$.

tetragonal phase has consistently shown to be a slower photocatalyst when compared to the monoclinic scheelite phase.[28]

4.3 Rate Analysis of Photocatalytic Benzylamine Oxidation on $CuWO_4$ and $BiVO_4$

To conduct photocatalytic $BnNH_2$ oxidation, 2 mL of a 250 mM $BnNH_2$ solution in MeCN was added to a 2 mL dram vial with a stir bar and 20 mg of metal oxide catalyst. A rubber septum was placed on the vial. A syringe with a balloon attached to it was filled with oxygen, a needle attached to it, and the needle placed into the septum. This allows for a constant atmosphere of oxygen in the reaction vial. The dram vial was then placed into the photoreactor where it was illuminated from the bottom and stirred during the entire course of the reaction.

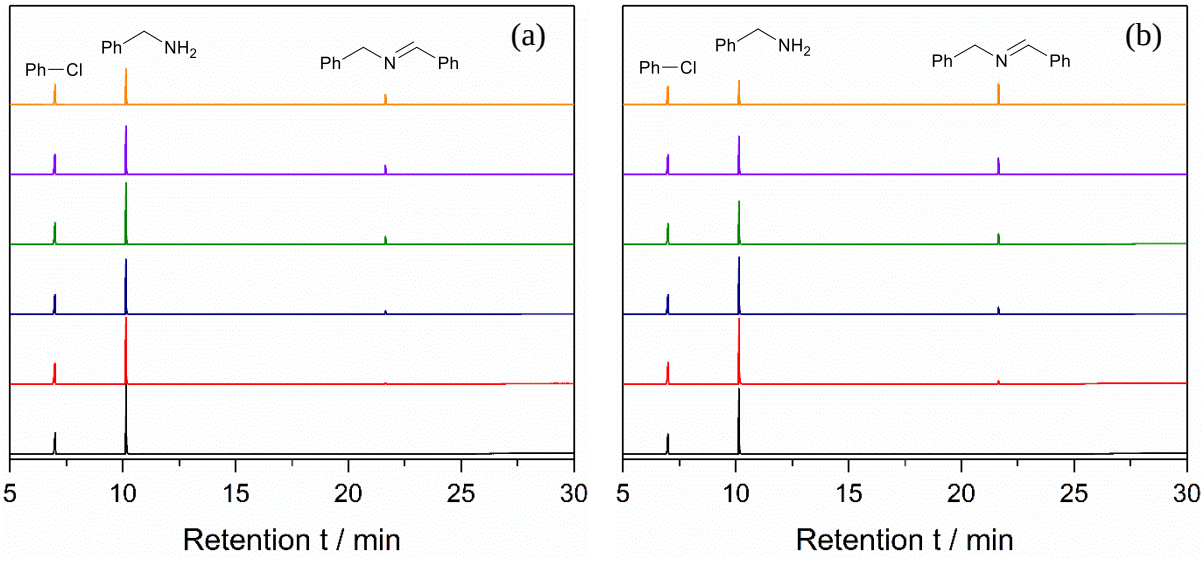

Figure 4.4: GC-FID traces of the photochemical oxidation of benzylamine on (a) $CuWO_4$ and (b) $BiVO_4$ at times 0 h (black), 12 h (red), 24 h (navy), 36 h (green), 48 h (violet), and 60 h (orange).

A gas chromatograph with an equipped flame ionization detector (GC-FID) was used to analyze the rate of $BnNH_2$ oxidation. Every 12 hours, a 10 µL aliquot of reaction was taken and put into a GC vial containing 990 µL of 1.01 mM chlorobenzene (Ph-Cl). This would give a concentration of 2.5 mM starting $BnNH_2$ and 1 mM Ph-Cl. The Ph-Cl was an external standard used for GC-FID. The GC-FID was calibrated for $BnNH_2$ and *N*-BB with 1 mM Ph-Cl prior to the reactions. The GC traces show that, as the time allowed for the reactions to proceed increased, the peak area of the benzylamine peak at a retention time of about 10 minutes decreased while a new peak at around 23 minutes, verified to be *N*-BB, grew in (Figure 4.4). Three trials of this reaction were conducted for both $CuWO_4$ and $BiVO_4$ (Table 4.1, Table 4.2 and Figure 4.5).

Table 4.1: Values calculated for the decrease in $BnNH_2$ concentration over time during the photocatalytic oxidation on $CuWO_4$

Time (h)	Trial 1 [$BnNH_2$] (mM)	Trial 2 [$BnNH_2$] (mM)	Trial 3 [$BnNH_2$] (mM)
0	248	245	249
12	225	218	229
24	209	211	213
36	207	195	203
48	173	174	187
60	166	149	164

Table 4.2: Values calculated for the decrease in $BnNH_2$ concentration over time during the photocatalytic oxidation on $BiVO_4$

Time (h)	Trial 1 [$BnNH_2$] (mM)	Trial 2 [$BnNH_2$] (mM)	Trial 3 [$BnNH_2$] (mM)
0	263	265	270
12	230	217	229
24	207	206	198
36	164	178	163
48	146	147	138
60	104	111	98

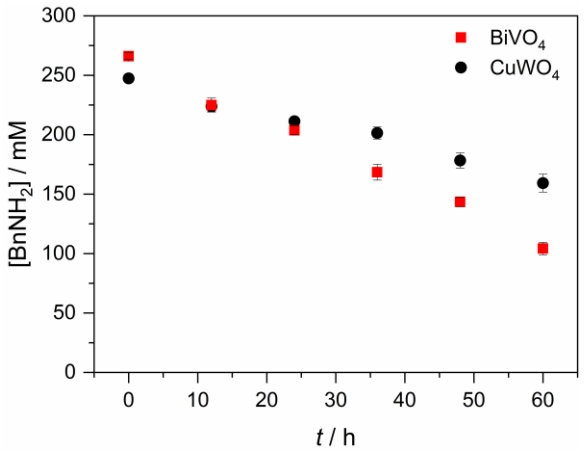

Figure 4.6: Decrease in benzylamine concentration over the course of its photochemical oxidation on $CuWO_4$ (black circles) and $BiVO_4$ (red squares). Values averaged over three trials.

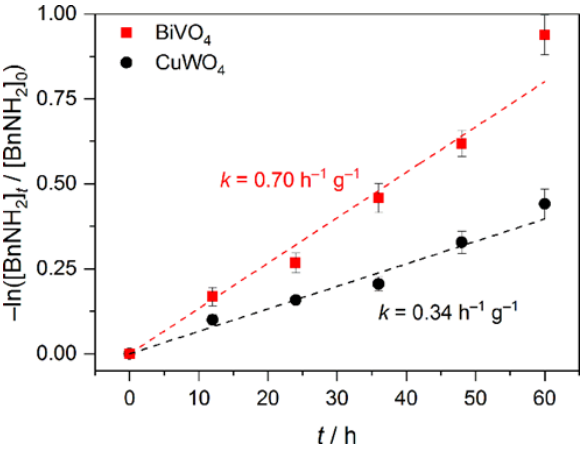

Figure 4.5: First-order rate plot for the photocatalytic oxidation of $BnNH_2$ on $CuWO_4$ and $BiVO_4$.

When the $-\ln([BnNH_2]_t / [BnNH_2]_0)$ was plotted vs time (where $[BnNH_2]_t$ is the $BnNH_2$ concentration at time t in mM and $[BnNH_2]_0$ is the starting $BnNH_2$ concentration), the data formed straight lines for both $CuWO_4$ and $BiVO_4$ reactions (Figure 4.6). These data suggest that $BnNH_2$ oxidation is first order in $BnNH_2$ concentration when catalyzed by both $CuWO_4$ and $BiVO_4$. The slope of each line represented the observed rate constant for $BnNH_2$ photocatalytic oxidation on each metal oxide.

The rate constant for $CuWO_4$ is 0.34 $h^{-1}g^{-1}$, only half of that observed on $BiVO_4$ (0.70 $h^{-1}g^{-1}$). The difference in $CuWO_4$ and $BiVO_4$ rate can be partially explained by differences in their electronic properties; namely their visible light induced electronic transitions and the existence of potential charge recombination sites in $CuWO_4$. Although the lowest energy band transitions for

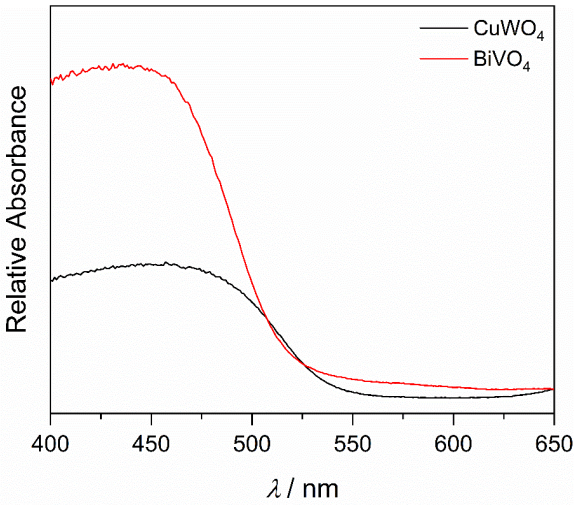

Figure 4.7: Diffuse reflectance spectra of as-synthesized $CuWO_4$ (black) and $BiVO_4$ (red).

both wolframite $CuWO_4$ and monoclinic scheelite $BiVO_4$ are indirect, $BiVO_4$ has a direct transition at ~0.2 eV greater than its band gap.[29] Photogenerated holes in $CuWO_4$ provide a greater oxidative driving force than in $BiVO_4$ (valence band maxima of 2.6 and 2.2 V vs NHE for $CuWO_4$ and $BiVO_4$, respectively), but the larger absorption coefficient imparted to $BiVO_4$ by this direct transition (as can be seen in the diffuse reflectance absorption spectrum, Figure 4.7) could explain the faster rate for $BnNH_2$ oxidation. While the charge carrier mobilities have not been reported for $CuWO_4$, it is plausible that the localized nature of $dx^2–y^2$ electrons in Jahn-Teller distorted Cu^{2+} can act as a trap state for this material, leading to surface charge recombination.[30] This distortion is not present in monoclinic scheelite $BiVO_4$.

To verify that the overall rate was not limited by oxygen reduction, the rates of $BnNH_2$ oxidation on $CuWO_4$ with and without deposited platinum on the catalyst surface were calculated and compared. The platinum was photodeposited onto $CuWO_4$ from a solution of hexachloroplatinic acid illuminated by a Xe-Hg lamp. Measurements by ICP showed that the Pt/$CuWO_4$ catalyst was 0.1 weight% platinum. Platinum (the metal of choice for the cathode in fuel cells where it catalyzes O_2 reduction)[31] facilitates the transfer of photoexcited

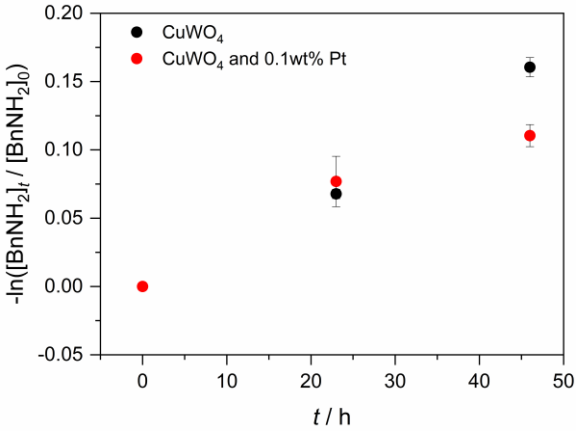

Figure 4.8: First order rate plot of the photocatalytic oxidation of $BnNH_2$ on $CuWO_4$ and Pt/$CuWO_4$. Each point is an average of two experiments.

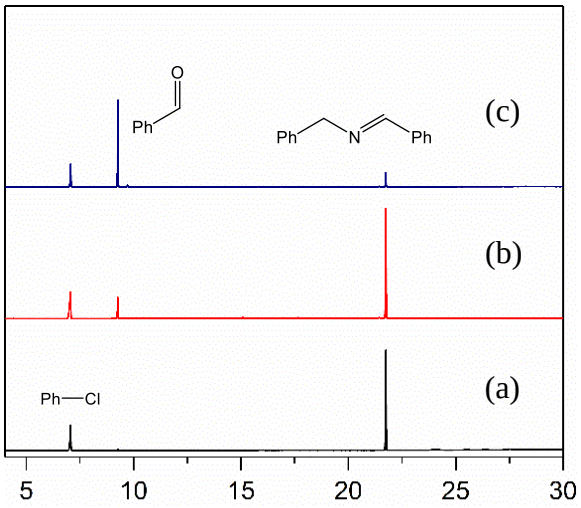

Figure 4.9: Photocatalytic oxidation of *N*-BB to benzaldehyde. GC-FID trace of (a) 5 mM *N*-BB in MeCN (b) post-photolysis solution of reaction containing $CuWO_4$ and (c) post-photolysis solution of reaction containing $BiVO_4$. Reaction conditions: 20 mg of catalyst, 2 mL of 5 mM *N*-BB in MeCN, blue LED, O_2 atmosphere, 24 h.

electrons from the conduction band of $CuWO_4$ to the O_2 in solution. If O_2 reduction was the limiting reaction in the catalytic process, then adding Pt to the surface of the catalyst would lead to an increase in overall reaction rate. The rate constants for $BnNH_2$ for the $CuWO_4$ and $Pt/CuWO_4$ are near identical at 0.290 h^{-1} g^{-1} and 0.235 h^{-1} g^{-1}, respectively (Figure 4.8). With no increase in the rate constant upon addition of Pt to the surface of the $CuWO_4$ photocatalyst, O_2 was confirmed to not limit the rate of $BnNH_2$ oxidation.

4.4 Chemoselectivity of Photocatalytic Benzylamine Oxidation on $CuWO_4$ and $BiVO_4$

To probe the chemoselectivity for photocatalytic *N*-BB formation on both $CuWO_4$ and $BiVO_4$, the reaction was allowed to proceed until high conversion (>90%) of $BnNH_2$ was achieved (Table 4.3). The times required for each catalyst to attain this were varied due to the differences in kinetics presented above. Reactions were not allowed to reach 100% conversion because, if

Table 4.3 Selectivity of the photocatalytic oxidation of $BnNH_2$ on $CuWO_4$ and $BiVO_4$ for *N*-BB formation at high conversion

Entry	Conditions	Time (h)	Conversion (%)	Selectivity for *N*-BB (%)
1	$CuWO_4$	180	93	99
2[a]	$CuWO_4$	24	15	N/A
3	$BiVO_4$	130	91	98
4[a]	$BiVO_4$	24	23	N/A
5	No catalyst	24	0	N/A
6	$CuWO_4$, dark	24	0	N/A
7	$BiVO_4$, dark	24	0	N/A
8[b]	$CuWO_4$, O_2-free	24	0	N/A
9[b]	$BiVO_4$, O_2-free	24	0	N/A

Reaction conditions: Blue LED illumination (λ_{max} = 448 nm, 200 mW/cm^2), 20 mg of catalyst, volume of 2 mL of 250 mM $BnNH_2$ in acetonitrile capped with O_2 balloon. Conversions determined by gas chromatography using chlorobenzene as an internal standard. Selectivity was determined by ^{1}H NMR. [a]The selectivity at 24 hours was not determined. [b]Reactions degassed and run under N_2 atmosphere.

illuminated beyond the time necessary to reach 100% conversion, the *N*-BB product begins to convert to benzaldehyde. This side reaction occurs on both $CuWO_4$ and $BiVO_4$; after stirring a solution of *N*-BB under blue light and O_2 in the presence of catalysts, benzaldehyde was indeed detected by GC-FID (Figure 4.9). The reason no benzaldehyde is observed before the complete consumption of $BnNH_2$ is because any benzaldehyde generated from overoxidation of *N*-BB during the reaction will immediately condense with $BnNH_2$ starting material still present in solution to form more *N*-BB.

Nearly identical selectivity of both $CuWO_4$ (99%) and $BiVO_4$ (98%) for *N*-BB formation was observed (Table 4.3 entries **1** and **3**). These chemoselectivity values were determined by ^1H NMR. The only difference in reaction setup was the use of deuterated MeCN instead of protonated MeCN as the solvent. The $BnNH_2$ conversion was monitored by GC-FID for reactions as described in Chapter 4.3 until greater than 90% conversion was achieved. The catalyst was filtered from the catalyst and 500 µL of the filtered solution was added to an NMR tube containing 100 µL of 0.6 M dichloromethane (DCM) in deuterated MeCN. This gives a solution 0.1 M in DCM, which was used as the standard. The catalyst was conducted over four trials each for both $CuWO_4$ and $BiVO_4$ Table 4.4, Table 4.5, and Figure 4.10). The $BnNH_2$ concentration was determined by integration of its benzylic proton peaks and the *N*-BB concentration was determined by integration of both the

benzylic protons and imine proton. The *N*-BB concentrations determined from each signal were then averaged to arrive at the final *N*-BB concentration. This agrees with previous reports of

Table 4.4 Determined concentrations of $BnNH_2$ and *N*-BB by ^1H NMR after photocatalytic oxidation on $CuWO_4$. The *N*-BB concentration was calculated using both the benzylic protons and imine proton. An internal standard of 0.1 M dichloromethane was used.

Concentration	Trial 1	Trial 2	Trial 3	Trial 4
$BnNH_2$ (mM)	35	18	16	30
N-$BB_{benzylic}$ (mM)	97	106	105	102
N-BB_{imine} (mM)	96	106	108	104

Table 4.5 Determined concentrations of $BnNH_2$ and *N*-BB by ^1H NMR after photocatalytic oxidation on $BiVO_4$. The *N*-BB concentration was calculated using both the benzylic protons and imine proton. An internal standard of 0.1 M dichloromethane was used.

Concentration	Trial 1	Trial 2	Trial 3	Trial 4
$BnNH_2$ (mM)	28	26	22	33
N-$BB_{benzylic}$ (mM)	114	116	123	120
N-BB_{imine} (mM)	115	118	123	121

the photocatalytic oxidation of $BnNH_2$ on metal oxides.[5,8,9,23–26] A series of control reactions demonstrate that the metal oxide, light, and oxygen are required to carry out the reaction; removing the catalyst results in no conversion upon illuminating the $BnNH_2$ solution (Table 4.3 entry **5**); neither catalyst performs $BnNH_2$ oxidation in the dark (Table 4.3 entries **6** and **7**); no conversion occurs when O_2 (the sacrificial oxidant) was replaced with N_2 (Table 4.3 entries **8** and **9**).

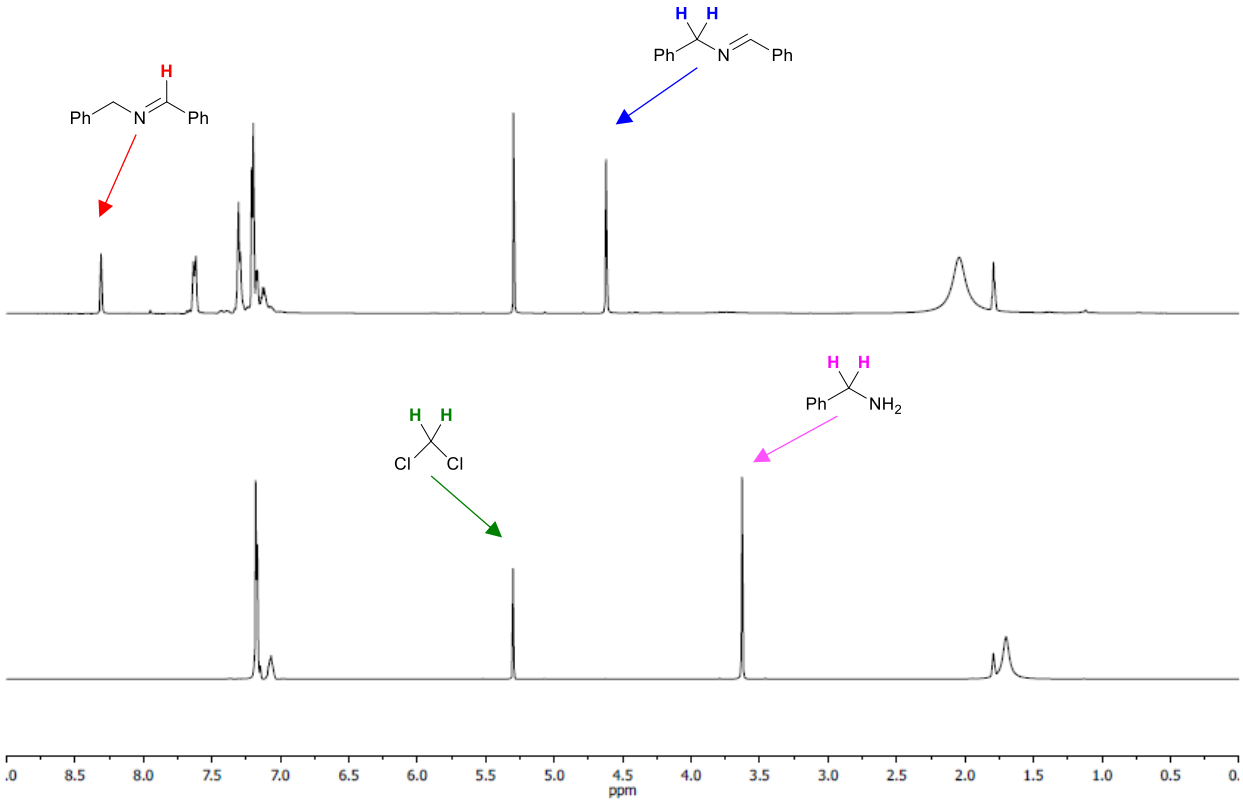

Figure 4.10: ^1H NMR spectra of 250 mM $BnNH_2$ solution pre-photolysis (bottom) and the reaction solution after 93% conversion of the benzylamine has been achieved after photochemical oxidation by $CuWO_4$ (top).

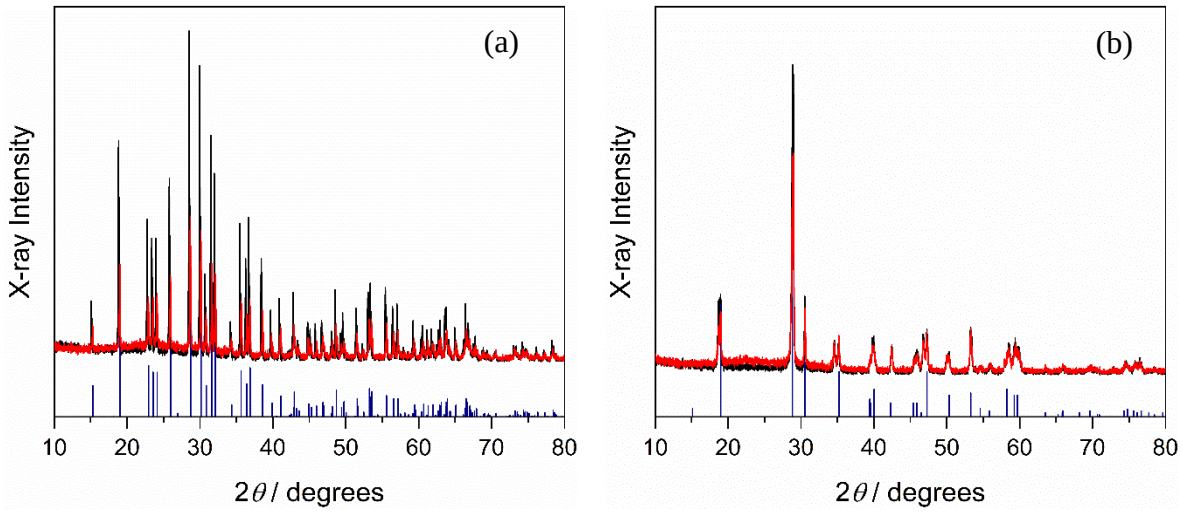

Figure 4.11: X-ray diffractograms of (a) $CuWO_4$ and (b) $BiVO_4$. Patterns were obtained for the as-synthesized powders (black) and for the catalyst collected after benzylamine oxidation (red). Reference patterns (navy) included are ICSD#24339 for $CuWO_4$ and ICSD#31550 for $BiVO_4$.

After photocatalytic reactions were complete, the oxide materials were washed with fresh MeCN, dried, and characterized. The X-ray diffractograms remained unchanged and no introduction of any surface functionality on either catalyst after the reaction was observed by IR spectroscopy (Figure 4.11 and Figure 4.12). As shown by SEM imaging, the catalysis causes the $CuWO_4$ to become less aggregated than the as-synthesized powder, but minor roughening of both the $CuWO_4$ and $BiVO_4$ surfaces was the only other change imparted to the powder by the reaction

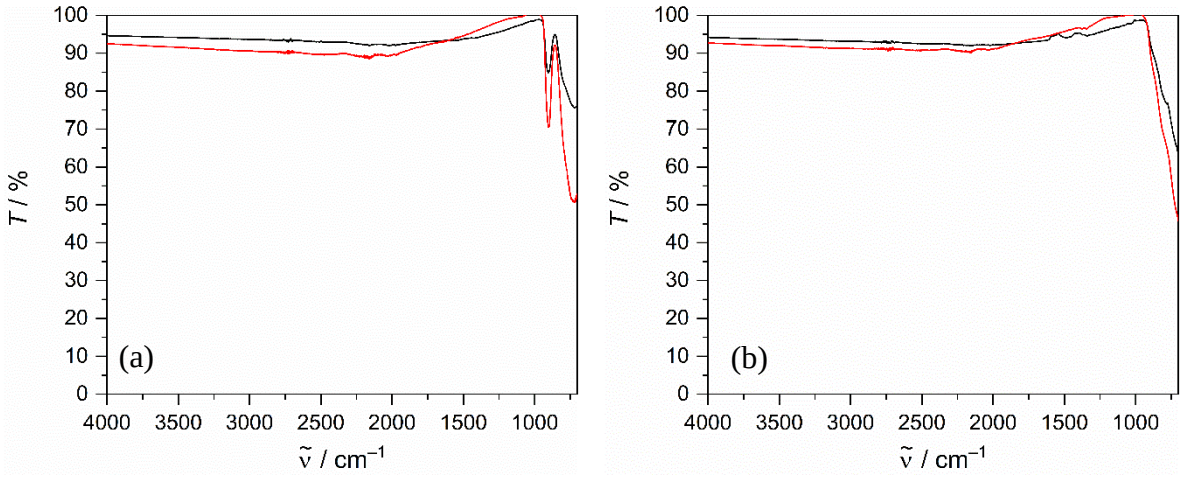

Figure 4.12: IR spectra of (a) $CuWO_4$ and (b) $BiVO_4$. Spectra were collected for the as-synthesized powders (black) and for the catalyst collected after benzylamine oxidation (red).

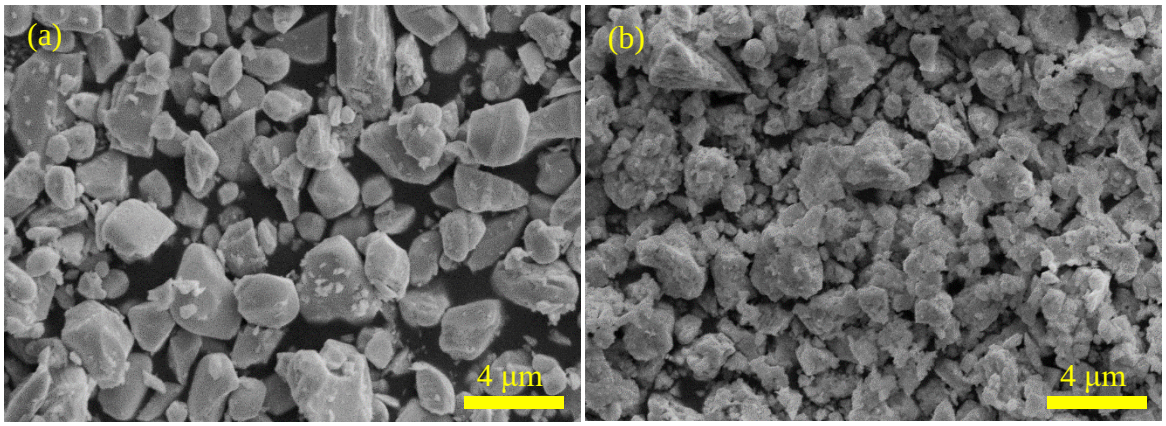

Figure 4.13: Scanning electron micrographs of (a) $CuWO_4$ and (b) $BiVO_4$ after being used for photocatalytic $BnNH_2$ oxidation carried out to over 90% conversion.

(Figure 4.13). These physical changes are attributed to the mechanical forces arising from stirring the reaction.

4.5 Recyclability of $CuWO_4$ and $BiVO_4$ for the Photocatalytic Oxidation of Benzylamine

The recyclability of $CuWO_4$ and $BiVO_4$ was also investigated by carrying out five successive $BnNH_2$ oxidation reactions on the same batch of each catalyst. Each set of five successive reactions had four trials completed for each catalyst. Given the robustness of metal oxide catalysts and that no major changes were seen in the characterization data of either $CuWO_4$ or $BiVO_4$, it was expected that these catalysts would be recyclable for this reaction. "Recyclable" in this discussion means that the same batch of catalyst would be capable of carrying out multiple successive reactions without losing any activity for the reaction (i.e. the rate of each successive reaction would be identical to those before it). The recyclability experiments showed similar conversions of $BnNH_2$ over all reactions conducted for both $CuWO_4$ and $BiVO_4$ (Figure 4.14). Each

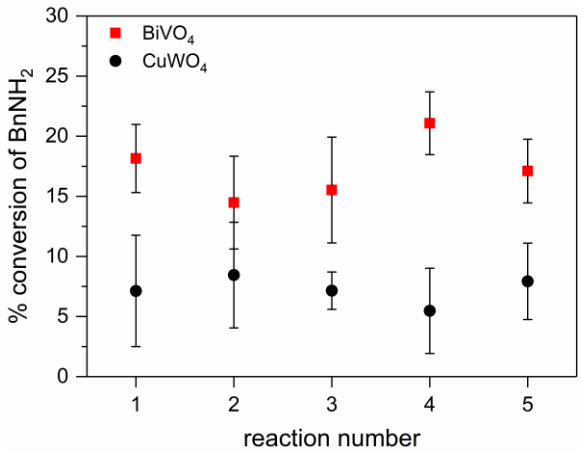

Figure 4.14: Recyclability of $CuWO_4$ (black circles) and $BiVO_4$ (red squares) for the photocatalytic oxidation of $BnNH_2$. The same batch of catalyst was used for each successive reaction. Each point is an average of four trials.

Table 4.6 The percent of the total quantity of catalyst detected as dissolved metal detected by ICP-MS measurements of post-photolysis solutions of successive photocatalytic oxidations of $BnNH_2$ to *N*-BB with the same batch of catalyst

Catalyst	Metal	Reaction Number (% of Total Catalyst Detected as Dissolved Metal)				
		1	2	3	4	5
$CuWO_4$	Cu	0.02	0.02	0.02	0.01	0.02
	W	0	0	0	0	0
$BiVO_4$	Bi	0	0	0	0	0
	V	0.01	0.01	0.01	0.01	0.01

reaction solution was also analyzed by inductively coupled plasma – mass spectrometry (ICP-MS) to check for dissolved metal content. Little to no metal content was expected to be in solution since no change in characterization data was observed between the pre- and post-photolysis particles. This prediction was confirmed, as only minute quantities of copper and vanadium (i.e. at most 0.02% of the total catalyst added to the reaction) were detected as dissolved metal (Table 4.6). Tungsten and bismuth were not detected. The similarities between the as-synthesized powders and post-photolysis powders, the steadiness of the reaction rate over 60 hours, combined with the high recyclability of these catalysts, demonstrates the stability of these materials towards photooxidative conditions.

4.6 Conclusions

This results in this chapter represent the first example of an aerobic photocatalytic amine oxidation on $CuWO_4$. Both $CuWO_4$ and $BiVO_4$ displayed ≥98% yield for generating *N*-benzylidenebenzylamine, with $BiVO_4$ catalyzing the reaction at about twice the rate. Both catalysts are recyclable for this reaction and do not degrade over the course of photocatalysis. This work serves as a starting point for the investigation of controlled photocatalytic oxidations of organic substrates on $CuWO_4$. Selectively generating useful aldehyde and ketone synthetic precursors from alcohols while avoiding stoichiometric oxidants would be useful. It would also be appealing to use $CuWO_4$ or other metal oxides in the oxidation of biomass-derived compounds. These hydroxylated compounds generally have proton-coupled oxidation reactions, which leads to many of them

generating protons as products. These protons could then be reduced to generate hydrogen gas as a fuel while oxidizing the biomass-derived compound to a more useful synthetic starting material. Notably, the overoxidation of *N*-BB observed in this work would not be a concern when oxidizing some important biomass-derived compounds. For example, the oxidation of 5-hydroxymethylfurfural to its fully oxidized dicarboxylic acid (not stopping at the dialdehyde) is actually desirable since the dicarboxylic acid can serve as a monomer for many polymer syntheses.

4.7 Experimental

Materials and Methods

Benzylamine (99%), *N*-benzylidenebenzylamine (99%), chlorobenzene (99+%, for spectroscopy), copper (II) oxide, tungsten oxide, and bismuth nitrate pentahydrate were purchased from Sigma-Aldrich. Acetonitrile (Certified ACS), dichloromethane (Certified ACS), ethanol (200 proof), and ammonium metavanadate were purchased from Fisher. Acetonitrile-d_3 was purchased from Cambridge Isotope Laboratories. Benzylamine was vacuumed distilled over NaOH and stored on sieves under N_2. All other reagents were used as received. Nylon syringe filters (25 mm, 0.2 μm membrane) were purchased from VWR or Macherey-Nagel.

Catalyst Preparation

Copper tungstate was synthesized by grinding a 1:1 mole ratio of copper (II) oxide (0.51 g) and tungsten oxide (1.49 g) in a mortar and pestle for 15 minutes followed by heating in a muffle furnace at 800 °C for 6 hours. The oven temperature ramped up to and down from 800 °C at a rate of 10 °C • min^{-1}. Bismuth vanadate was synthesized by grinding a 1:1 mole ratio of ammonium metavanadate (0.500 g) and bismuth (III) nitrate pentahydrate (2.07 g) for 15 minutes. This was heated in a muffle furnace at 500 °C for 6 hours. The oven temperature ramped up to and down

from 500 °C at a rate of 10 °C • min^{-1}. Both $CuWO_4$ and $BiVO_4$ were placed in a 12 mL polypropylene centrifuge with 7 mL of Milli-Q (18.2 MΩ•cm^{-1}) water and vortexed for about 30 seconds before centrifuging at 3500 rpm for 5 minutes. The water was then decanted and the process was repeated twice more. The powder was then washed three times with ethanol before drying overnight in a vacuum oven at 60 °C. Platinum was deposited onto $CuWO_4$ through a photodeposition method. To do this, 500 mg of $CuWO_4$ was added to a cell with a quartz window. To this, 20 mL of water and 13 mg of chloroplatinic acid was added. The solution was purged with N_2 for 30 minutes. Next, the cell (with the suspension stirring) was illuminated with irradiation from a Xe-Hg arc lamp with a power density of 500 mW•cm^{-2} at the front of the cell for 3 hours. The lamp was then turned off, 500 mg of hydroquinone was added to the cell, and the cell was purged for 15 minutes with N_2 before the lamp was turned on again. The solution was stirred and illuminated overnight. The lamp was turned off and the solution was allowed to stir for 30 minutes in the dark before removing the suspension from the cell and placing it into a 50 mL centrifuge tube. The suspension was centrifuged, decanted, and washed three times with Millipore water. The washed powder was then dried overnight in a vacuum oven set to 60 °C before using for catalysis.

Photocatalytic Reactions

All photocatalytic reactions were carried out in a custom-built aluminum LED assembly (Figure S1). Royal blue LEDs (λ_{max} = 448 nm) with a power rating of 1.03 W were purchased from Mouser Electronics (Mouser Part#: 997-LXML-PR02-A900). Reactions contained 20 mg of catalyst, 2 mL of substrate solution, and were run in 4 mL dram vials that had their flat bottoms visible to the LEDs while receiving a power density of 200 mW • cm^{-2}. Reactions were capped with rubber septa, kept under O_2 using a balloon, and stirred for an hour in the dark before having an aliquot

taken out to determine the initial concentration of benzylamine in each solution (procedure for making GC samples is described below). The reactions were then illuminated. For reactions run under N_2, the solutions had N_2 bubbled through them during the one hour of stirring in the dark. They were then run under an N_2 atmosphere for the rest of the experiment. A concentration of 250 mM benzylamine was used as the starting concentration of benzylamine for kinetics and selectivity experiments. Aliquots of 10 μL were taken out for each time point (every 12 hours for 60 hours) of the kinetics experiments. These were added to a GC vial that contained 990 μL of a 1.01 mM solution of chlorobenzene in acetonitrile. Conversion data for three reactions were collected and averaged for each catalyst. Reactions were analyzed by gas chromatography with a flame ionization detector. These were then converted to first order rate plots. GC-FID analysis was conducted on a Trace 1310 GC-FID system with a TG-5MS Amine column. Argon was used as the carrier gas. The heating method used for analysis was to ramp from 40 °C to 300 °C at a rate of 10 °C • min^{-1} and hold at 300 °C for 10 minutes before cooling. Before NMR analysis each reaction was filtered through a nylon syringe filter to remove the catalyst. A volume of 500 μL of the filtered reaction solution was added to an NMR tube that contained 100 μL of a 0.6 M dichloromethane internal standard solution in acetonitrile-d_3. Selectivity data for four reactions was collected and averaged for each catalyst. The concentration of *N*-BB was calculated using both the imine and benzylic protons and averaged. ^{1}H NMR data was collected on a Varian MR400 NMR spectrometer equipped with a Varian 5 mm PFG AutoX Dual Broadband probe. All NMR data was processed in MestReNova software.

Materials Characterization

The post-photolysis powders were washed with acetonitrile by adding the powder and 7 mL of acetonitrile to a 12 mL polypropylene centrifuge tube and vortexing for about 30 seconds before centrifuging at 3500 rpm for 5 minutes. This was decanted and repeated twice more. The powders were then dried in a vacuum oven at 60 °C overnight. Powder x-ray diffraction data were collected on a Panalytical Empyrean diffractometer at a power of 1.8 kW (45 kV, 40 ma) with Cu Kα (λ = 1.5418 nm) radiation. The detector was a X'Celerator Scientific, a position sensitive 1D detector equipped with Bragg-Brentano^{HD} x-ray optic delivering only Kα radiation. Patterns were collected with a sampling step of 0.020 and a scan rate of 0.080°• s^{-1} while spinning at a rate of 0.25 Hz. A Zeiss LEO 1455VP scanning electron microscope at an accelerating voltage of 10 kV and working distance of 5 mm was used for imaging the catalysts. SEM samples were sputter-coated with gold with a Cressington 108auto sputter coater for eight seconds prior to imaging. BET surface areas of the catalysts were obtained using nitrogen adsorption measurements on a Quantachrome NOVA4200e. A Varian Cary 5000 spectrophotometer equipped with an external diffuse reflectance accessory was used for UV-vis measurements. Spectra were collected in reflectance mode and transformed into absorbance using the Kubelka-Monk function. Barium sulfate was used as a 100% reflectance standard. Infrared spectroscopy was conducted using a Thermo Scientific Nicolet iS50 FT-IR with an ATR attachment.

Catalyst Recyclability and Metal Leaching

Multiple photocatalytic oxidations of benzylamine were done with the same batch of catalyst to determine recyclability of both $CuWO_4$ and $BiVO_4$. Dissolved metal content in each successive reaction solution was also determined. The method used for carrying out these photocatalytic reactions is identical to that described above. Each reaction was illuminated for 24 hours. After

this illumination time, the reactions were centrifuged for 10 minutes at 2500 rpm and 500 μL was removed. This was filtered through a nylon syringe filter and diluted with aqueous HNO_3 / 0.01% TritonX-100 to give a solution 0.5% in reaction solution by volume. This was used for ICP-MS analysis of the dissolved metal content in the post-photolysis solution. All ICP-MS measurements were conducted on a PerkinElmer NexION 2000 ICP-MS instrument. The conversion of benzylamine in each reaction was determined with GC as it was with the kinetics experiments described above. The reaction then had the majority of the remaining solution removed with a pipet, being careful to not remove any catalyst. A volume of 2 mL of acetonitrile was added to the dram vial. This was stirred for 5 minutes in the dark before being centrifuged. The solution was again removed, and a new volume of acetonitrile was added. This washing procedure was repeated four times. The catalyst was then put in a vacuum oven at 50 °C to dry overnight. This catalyst was then used in further photocatalytic oxidation reactions of benzylamine. Four trials of five successive reactions were conducted for each catalyst.

4.8 References

[1] Romero, N. A. and Nicewicz, D. A. Organic Photoredox Catalysis. *Chem. Rev.* **2016**, *116*, 10075-10166.
[2] Narayanam, J. M. R. and Stephenson C. R. J. Visible light photoredox catalysis: applications in organic synthesis. *Chem. Soc. Rev.* **2011**, *40*, 102-113.
[3] Shaw, M. H.; Twilton, J. and MacMillan D. W. C. Photoredox Catalysis in Organic Chemistry. *J. Org. Chem.* **2016**, *81*, 6898-6926.
[4] Adolph, C. M.; Werth, J.; Selvaraj, R.; Wegnener, E. C. and Uyeda, C. Dehydrogentative Transformations of Imines Using a Heterogeneous Photocatalyst *J. Org. Chem.* **2017**, *82*, 5959-5965.
[5] Yuan, B.; Chong, R.; Zhang, B.; Li, J.; Liu, Y. and Li C. Photocatalytic aerobic oxidation of amines to imines on $BiVO_4$ under visible light irradiation. *Chem. Commun.* **2014**, *50*, 15593-15596.
[6] Kirsch, H. Semiconductor Photocatalysis for Chemoselective Radical Coupling Reactions. *Acc. Chem. Res.* **2017**, *50*, 1002-1010.
[7] Wada, E.; Takeuchi, T.; Fujimura, Y.; Tyagi, A.; Kato, T. and Yoshida, H. Direct cyanomethylation of aliphatic and aromatic hydrocarbons with acetonitrile over a metal loaded titanium oxide photocatalyst. *Catal. Sci. Technol.* **2017**, *7*, 2457-2466.
[8] Lang, X.; Ma, W.; Chen, C.; Ji, H. and Zhao, J. Selective Aerobic Oxidation Mediated by TiO_2 Photocatalysis. *Acc. Chem. Res.* **2014**, *47*, 355-363.
[9] Furukawa, S.; Ohno, Y.; Shishido, T.; Teramura, K. and Tanaka, T. Reaction Mechanism of Selective Photooxidation of Amines over Niobium Oxide: Visible-Light-Induced Electron Transfer between Adsorbed Amine and Nb_2O_5. *J. Phys. Chem. C* **2013**, *117*, 442-450.

[10] Hou, T.; Luo, N.; Li, H.; Heggen, M.; Lu, J.; Wang, Y. and Wang, F. Yin and Yang Dual Characters of CuO_x Clusters for C−C Bond Oxidation Driven by Visible Light. *ACS Catal.* **2017**, *7*, 3850-3859.
[11] Zavahir, S.; Xiao, Q.; Sarina, S.; Zhao, J.; Bottle, S.; Wellard, M.; Jia, J.; Jing, L.; Huang, Y.; Blinco, J.P.; Wu, H. and Zhu, H.-Y. Selective Oxidation of Aliphatic Alcohols using Molecular Oxygen at Ambient Temperature: Mixed-Valence Vanadium Oxide Photocatalysts. *ACS Catal.* **2016**, *6*, 3580-3588.
[12] Pitre, S. P.; Yoon, T. P.; and Scaiano, J. C. Titanium dioxide visible light photocatalysis: surface association enables photocatalysis with visible light irradiation. *Chem. Commun.* **2017**, *53*, 4335-4338.
[13] Lhermitte, C. R. and Bartlett B. M. Advancing the Chemistry of $CuWO_4$ for Photoelectrochemical Water Oxidation. *Acc. Chem. Res.* **2016**, *49*, 1121-1129.
[14] Yourey, J. E.; Pyper, K. J.; Kurtz, J. B. and Bartlett, B. M. Chemical Stability of $CuWO_4$ for Photoelectrochemical Water Oxidation. *J. Phys. Chem. C* **2013**, *117*, 8708-8718.
[15] Pyper, K. J.; Yourey, J. E. and Bartlett, B. M. Reactivity of $CuWO_4$ in Photoelectrochemical Water Oxidation Is Dictated by a Midgap Electronic State. *J. Phys. Chem. C* **2013**, *117*, 24726-24732.
[16] Gao, Y. and Hamann, T. W. Quantitative hole collection for photoelectrochemical water oxidation with $CuWO_4$. *Chem. Commun.* **2017**, *53*, 1285-1288.
[17] Guo, W.; Duan, Z.; Mabayoje, O.; Chemelewski, W. D.; Xiao, P.; Henkelman, G.; Zhang, Y. and Buddie M. C. J. Improved Charge Carrier Transport of Hydrogen-Treated Copper Tungstate: Photoelectrochemical and Computational Study. *Electrochem. Soc.* **2016**, *163*, H970-H975.
[18] Wen, Y.; Chen, F.; Zhao, F.; Han, N. and Yanguang, L. $CuWO_4$ Nanoflake Array-Based Single-Junction and Heterojunction Photoanodes for Photoelectrochemical Water Oxidation. *ACS Appl. Mater. Interfaces* **2016**, *8*, 9211-9217.
[19] Yourey, J. E. and Bartlett, B. M. Electrochemical Deposition and Photoelectrochemistry of $CuWO_4$, a Promising Photoanode for Water Oxidation.*J. Mater. Chem.* **2011**, *21*, 7651-7660.
[20] Gao, T. and Hamann, T. W. Elucidation of $CuWO_4$ Surface States During Photoelectrochemical Water Oxidation. *J. Phys. Chem. Lett.* **2017**, *8*, 2700-2704.
[21] Limin, L.; Liu, H.; Tian, Y.; Hao, Q.; Liu, C.; Wang, W. and Xie, X. Fabrication of novel $CuWO_4$ hollow microsphere photocatalyst for dye degradation under visible-light irradiation. *Mater. Lett.* **2016**, *182*, 302-304.
[22] Ohkubo, K.; Nanjo, T. and Fukuzumi, S. Photocatalytic Electron-Transfer Oxidation of Triphenylphosphine and Benzylamine with Molecular Oxygen via Formation of Radical Cations and Superoxide Ion. *Bull. Chem. Soc. Jpn.* **2006**, *79*, 1489-1500.
[23] Furukawa, S.; Ohno, Y.; Shishido, T.; Teramura, K. and Tanaka, T. Selective Amine Oxidation Using Nb_2O_5 Photocatalyst and O_2. *ACS Catal.* **2011**, *1*, 1150-1153.
[24] Seisenbaeva, G. A.; Cojocaru, B.; Jurca, B.; Tiseanu, C.; Jean-Marie, N.; Kessler, Parvulescu, V. I. Mesoporous Tantalum Oxide Photocatalyst: Structure and Activity Evaluation. *Chemistry Select* **2017**, *2*, 421-427.
[25] Bu, J.; Fang, J.; Leow, W. R.; Zheng, K. and Chen, X. Single-crystalline rutile TiO_2 nano-flower hierarchical structures for enhanced photocatalytic selective oxidation from amine to imine. *RSC Adv.* **2015**, *5*, 103895-103900.
[26] Zavahir, S. and Zhu, H. Visible Light Induced Green Transformation of Primary Amines to Imines Using a Silicate Supported Anatase Photocatalyst. *Molecules* **2015**, *20*, 1941-1954.
[27] Pegis, M. L.; Roberts, J. A. S.; Wasylenko, D. J.; Mader, E. A.; Appel, A. M. and Mayer, J. M. Standard Reduction Potentials for Oxygen and Carbon Dioxide Couples in Acetonitrile and *N*,*N*-Dimethylformamide. *Inorg. Chem.* **2015**, *54*, 11883-11888.
[28] Fan, H.; Jiang, T.; Li, H.; Wang, D.; Wang, L.; Zhai, J.; He, D.; Wang, P. and Xie, T. Effect of $BiVO_4$ Crystalline Phases on the Photoinduced Carriers Behavior and Photocatalytic Activity. *J. Phys. Chem. C* **2012**, *116*, 2425-2430.
[29] Cooper, J. K.; Gul, S.; Toma, F. M.; Chen, L.; Liu, Y.-S.; Guo, J.; Ager, J. W.; Yano, J. and Sharp, I. D. Indirect Bandgap and Optical Properties of Monoclinic Bismuth Vanadate. *J. Phys. Chem. C* **2015**, *119*, 2969-2974.
[30] Yourey, J. E.; Kurtz, J. B. and Bartlett, B. M. Structure, Optical Properties, and Magnetism of the Full $Zn_{1-x}Cu_xWO_4$ ($0 \leq x \leq 1$) Composition Range. *Inorg. Chem.* **2012**, *51*, 10394-10401.
[31] Stephens, I. E. L.; Bondarkenko, A. S.; Gronbjerg, U.; Rossmeisl; J. and Chorkendorff, I. Understanding the electrocatalysis of oxygen reduction on platinum and its alloys. *Energy Environ. Sci.* **2012**, *5*, 6744-6762.

Chapter 5 Photocatalytic Oxidation of Alcohols on Various Metal Oxide Powders

5.1 Introduction

As discussed in previous introduction sections to chapters in this thesis, pairing proton reduction (to generate hydrogen gas, a clean burning fuel), with an organic oxidation instead of water oxidation has the possibility of increasing the overall rate of hydrogen production while also generating a soluble oxidation product that is more economically valuable than its reduced form. Using a biomass-derived compound as the starting material would make this process based on renewable materials. These biomass-derived compounds are heavily hydroxylated, so if photocatalytically oxidizing these on metal oxides is a goal, then investigating the oxidation of a model alcohol starting material is a first step into understanding the feasibility of reaching the goal. Earlier in this thesis (Chapter 2), efforts towards benzyl alcohol oxidation photoelectrocatalytically on WO_3 and $WO_3 \mid FeOOH \mid NiOOH$ were discussed. The low Faradaic efficiencies of these reactions prompted a movement away from alcohols and towards easier-to-oxidize amine starting compounds on $CuWO_4$ as a first attempt at exploring the catalytic activity of this ternary metal oxide towards organic oxidations. This chapter now moves back to alcohol oxidations on metal oxides. First, the photocatalytic oxidation of a diol, 1-phenyl-1,2-ethanediol (Figure 5.1), on TiO_2 was briefly investigated, and second, the photocatalytic oxidation of fructose and glycerol (Figure 5.1) were attempted on various metal oxides. And finally,

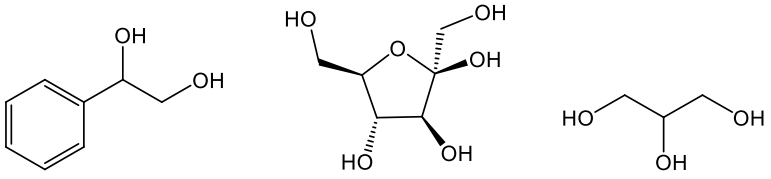

1-phenyl-1,2-ethanediol | Fructose | Glycerol

Figure 5.1: Chemical structures for primary substrates of interest in this chapter.

evidence of curious C-C bond cleavage upon oxidation of some benzylic and aliphatic alcohols was investigate on bismuth tungstate (Bi_2WO_6) powders. While TiO_2 has been shown to oxidize benzyl alcohol and some derivatives, the crystalline phase dependence of the TiO_2 on the product distribution of a diol has not been investigated.[1–4] Since many biomass-derived compounds have more than one hydroxyl group present in their structure, understanding the selectivity of photocatalysts towards the oxidation of polyols is important.

As a photocatalyst, TiO_2 first garnered serious attention when it was used as a photoelectrocatalyst to split water by Fujishima and Honda in 1972.[5] It has a wide band gap of 3.0 – 3.2 eV, depending on which crystalline phase of the metal oxide is considered – anatase has an indirect band gap of ~3.2 eV while rutile has a direct band gap of ~3.0 eV.[6] Other differences also exist between TiO_2 phases, such as carrier lifetime, carrier mobility, nature of surface defects, surface potential, and the ability to adsorb and transfer charge to a substrate (Table 5.1).[6–11] These properties may also differ in a single phase of TiO_2 with respect to different crystallographic planes. For example, charge mobility has been reported to be greater in the <100> direction of rutile over the <001> direction.[12,13] It was thought that these electronic differences could lead to different product distributions when these different phases of TiO_2 were used to oxidize a diol. Along with anatase and rutile TiO_2, the most common commercial TiO_2 photocatalyst, P25, was also used in this work. P25 is a mixture of anatase and rutile phases and is considered to have

Table 5.1: Reported various electronic properties for anatase and rutile TiO_2. All superscripts next to values represent the reference where they were reported.

TiO_2 Phase	Bandgap (eV)	h^+ Diffusion Length (nm)	e^- Diffusion Length (nm)	h^+ Mobility ($cm^2 \cdot V^{-1}s^{-1}$)	e^- Mobility ($cm^2 \cdot V^{-1}s^{-1}$)
Anatase	3.2[6]	3.2 ± 0.6[6]	10[7] – 10,000[8]	16[9] – 70[10]	0.1 – 17[11]
Rutile	3.0[6]	1.6 ± 0.4[6]	100[8]	1.4 – 8[6]	0.5 – 2.5[11]

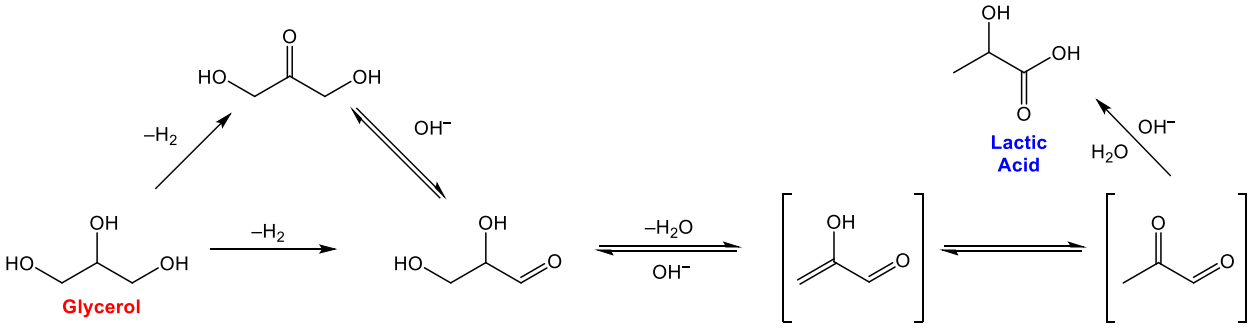

Figure 5.2: Proposed mechanism for the reaction of glycerol to lactic acid under basic conditions. Once glycerol has one of its primary hydroxyl groups oxidized to an aldehyde, a base-catalyzed dehydration to an enol can occur. The final reaction in this series to reach lactic acid is an intramolecular Cannizzaro reaction of the enol.

greater catalytic activity than either of its pure components, though a widely accepted explanation for the difference in photocatalytic activity between TiO_2 phases has not been reached.[6]

Fructose and glycerol were chosen as substrates for the second portion of the work in this chapter since these are biomass-derived compounds that result from the acid catalyzed decomposition of cellulose and the byproduct of biodiesel production, respectively.[14,15] These biomass-derived compounds are also saturated alcohols with no highly activated positions like that present in benzyl alcohol (the benzylic position allows for stabilization of reaction intermediates, making the oxidation of benzyl alcohol much more thermodynamically feasible than a compound like glycerol). Glycerol is attractive as a starting material since this allows the opportunity to upgrade a waste product into a more valuable compound, namely lactic acid. Lactic acid is a precursor to the biodegradable polyester, poly(lactic acid). It is also used as a feedstock for green solvent synthesis and utilized in the pharmaceutical and detergent industries.[15,16] A proposed mechanism for the reaction of glycerol to lactic acid begins with the oxidation of one of the hydroxyl groups to an aldehyde (Figure 5.2). Metal oxides have been shown to photocatalyze this reaction, though the selectivity for a single product typically drops when using a saturated alcohol when compared to reactions where an activate alcohol (e.g. benzyl alcohol) is used.[17] Fructose is also capable of being converted into valuable oxidation products. For example, glucose (a

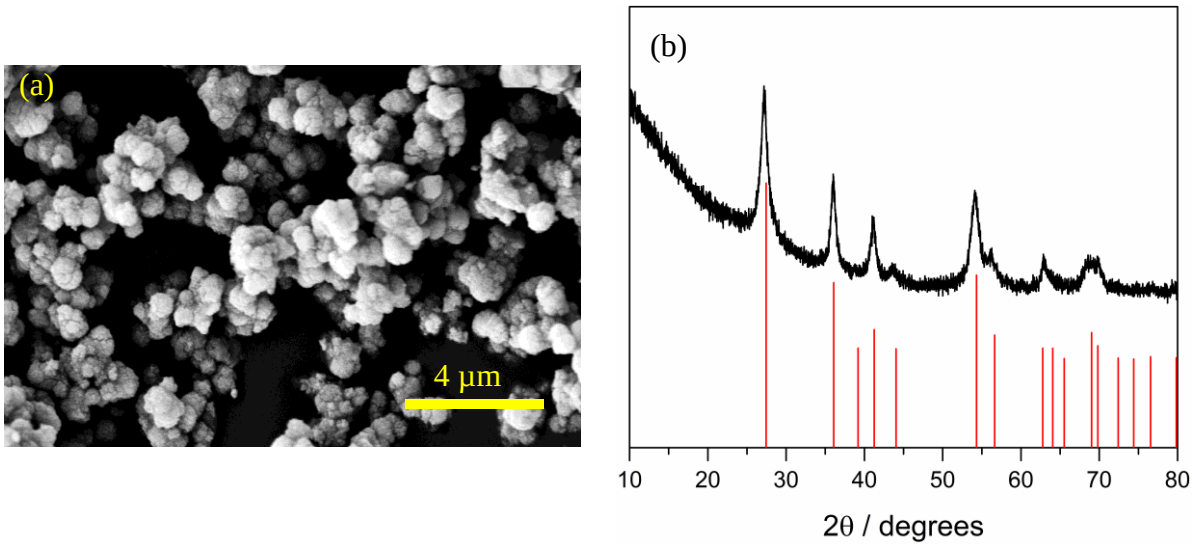

Figure 5.3: Scanning electron micrograph (a) and powder X-ray diffractogram (b) of synthesized rutile TiO_2. The red lines in the diffractogram are the reference patter (PDF#78-1509).

structural isomer of fructose), has been converted by heterogenous catalysts (including TiO_2) into formate/formic acid and levulinic acid.[18,19] Formic acid is valuable due to its potential hydrogen storage applications.[2021] Levulinic acid, like 5-hydroxymethylfurfural discussed in the introduction to Chapter 3 of this thesis, is also recognized by the U.S. Department of Energy as one of the top 12 sugar-derived building block chemicals that "could serve as an economic driver for a biorefinery."[22]

5.2 Synthesis and Characterization of Rutile TiO_2

Rutile TiO_2 was the only phase of TiO_2 that had to be synthesized for this work (anatase and P25 TiO_2 were purchased). Briefly, $TiCl_4$ was added dropwise to water with no stirring. Once the addition of the $TiCl_4$ was complete, the solution was stirred for 2 minutes.[23] After the stir bar was removed the vessel was capped and stored for 6 days. The contents of the vessel were centrifuged and the TiO_2 powder washed multiple times with DI water before it was put into a vacuum oven to dry. The powder had a morphology consisting of about 1 um diameter spheres that were speckled with even smaller particles (Figure 5.3 (a)). The material was pure rutile TiO_2 (Figure 5.3 (b)).

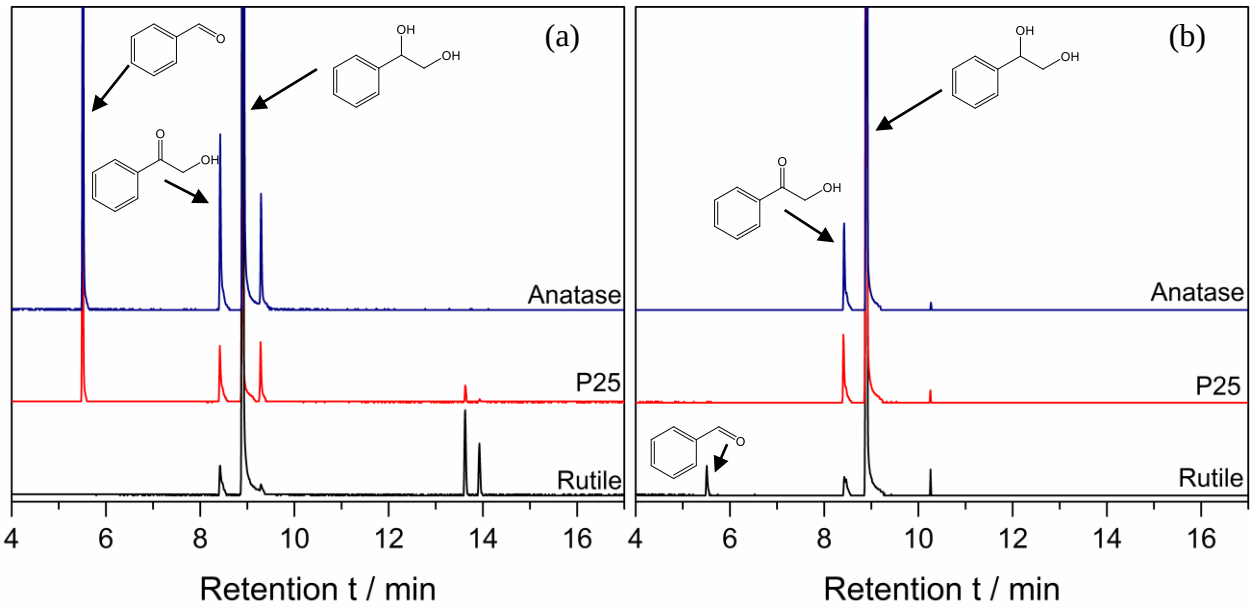

Figure 5.4: GC-MS traces of acetonitrile (a) and water (b) reaction solutions of 1-phenyl-1,2-ethanediol after being stirred with different phases of TiO_2 under illumination by a xenon arc lamp.

5.3 Photocatalytic Oxidation of 1-phenyl-1,2-ethanediol on Anatase, Rutile, and P25 TiO_2

To qualitatively determine the selectivity of 1-phenyl-1,2-ethanediol oxidation on different TiO_2 phases, TiO_2 powder was stirred in both non-aqueous and aqueous solutions of 1-phenyl-1,2-ethanediol while being illuminated by a xenon arc lamp. With no filter applied, the xenon arc lamp provides the low wavelength irradiation that can be absorbed by TiO_2. The reaction vessels were capped and had a positive pressure of O_2 gas on them during the reactions. Since O_2 reduction is the occurring during 1-phenyl-1,2-ethanediol oxidation, the constant O_2 pressure keeps the reactions saturated with O_2 to prevent any limiting of the overall reaction rate due to low oxygen concentration.

For the reactions carried out in acetonitrile, anatase was the only TiO_2 phase to not form higher molecular weight products (seen between retention times of 13-14 minutes, Figure 5.4 (a)). These

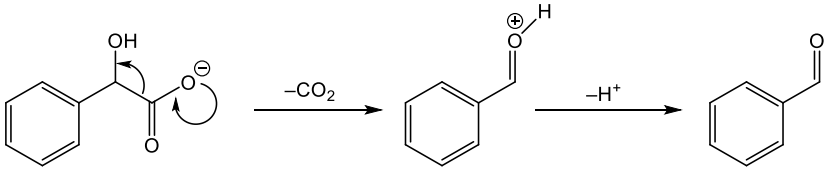

Figure 5.5: Possible mechanism for the formation of benzaldehyde from decarboxylation of mandelic acid. Mandelic acid is a potential product of photocatalytic oxidation of 1-phenyl-1,2-ethanediol with TiO_2.

products did not match any compounds in the GC-MS databank well and their retention times did not match any of the known retention times for the expected oxidation products that were examined. All TiO_2 phases produced benzaldehyde except for rutile. Benzaldehyde was not an expected product of the reaction due to the C-C bond cleavage that would be required for this to occur. The formation of benzaldehyde could be explained by decarboxylation. If the primary alcohol is oxidized completely to the carboxylic acid, loss of CO_2 could occur, leaving only benzaldehyde, in the fashion shown below (Figure 5.5). All phases formed 2-hydroxyacetophenone (~5.5 min) to some extent, along with an unknown product (~9.5 min) seen eluting immediately after the starting material (~9.0 min). For the reactions run in water, no TiO_2 phases formed higher molecular weight products (Figure 5.4 (b)). Opposite of the results from the reaction run in acetonitrile, rutile was the only phase to form benzaldehyde. Again, all phases formed 2-hydroxyacetophenone. There was also an unknown product at ~10.25 min. generated by all TiO_2 phases. The results here confirm that the phase of TiO_2 does have an effect on selectivity.

Solvent also had an effect on the selectivity, but not as expected; the reaction carried out in water actually had a narrower distribution of oxidation products than the reaction conducted in acetonitrile. However, the kinetics of the reaction done in water could be considerably slower than those of the acetonitrile reaction, and thus the products shown are representative of only a small conversion of the original diol. It must also be kept in mind that the particles sizes and morphologies were not all identical between the phases and could have played a role in the product distribution. Even with these considerations, the narrow product distribution was a surprise, as the selectivity of reactions in water are typically plagued by radical side reactions caused by the presence of the hydroxyl radical.[17]

5.4 Photocatalytic Aqueous Oxidation of Fructose and Glycerol on Various Metal Oxides

The reaction of fructose with WO_3 was the first that was investigated. The custom blue LED setup that was used in the work in Chapter 4 was used for all reactions described in this section. The reactions were illuminated under an O_2 atmosphere for 24 hours in water with and without 0.1 M HCl (Figure 5.6 (a)). This resulted in two new peaks observed in the ^{1}H NMR. For all reactions, there was a singlet at ~1.9 ppm (Figure 5.6 (b)). This was not able to be identified. This peak has a similar shift to acetone, however. A shift upfield suggests this signal may be generated by protons no longer adjacent to hydroxyl groups. This would either required multiple hydroxyl group to be oxidized to carbonyls on the fructose structure or multiple C-C bond cleavage events to occur to produce environments that have protons non-adjacent to hydroxyl groups. It is clear that neither of the primary hydroxyl groups get oxidized to aldehydes in this reaction, as there are no new aldehyde signals at ~9-10 ppm where one would expect. One of the reactions, however, does produce a singlet at ~8.1 ppm. This only occurs in the reaction that was illuminated and contained WO_3 and acid (Figure 5.6 (c)). Though the production of formic acid under these

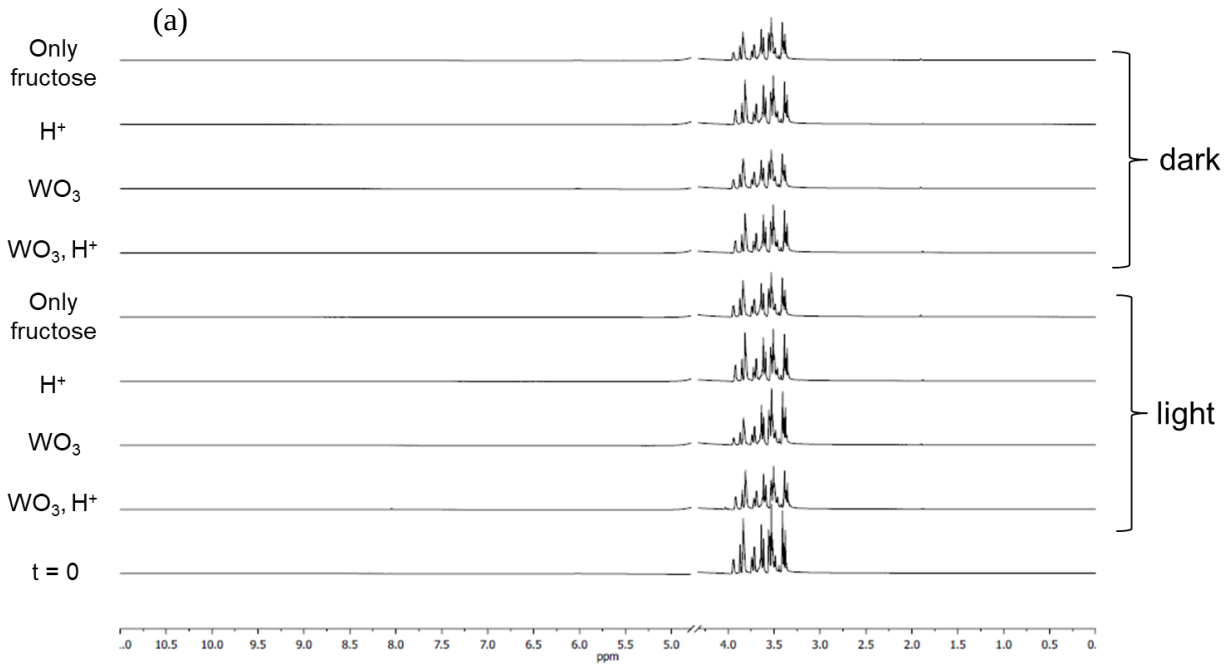

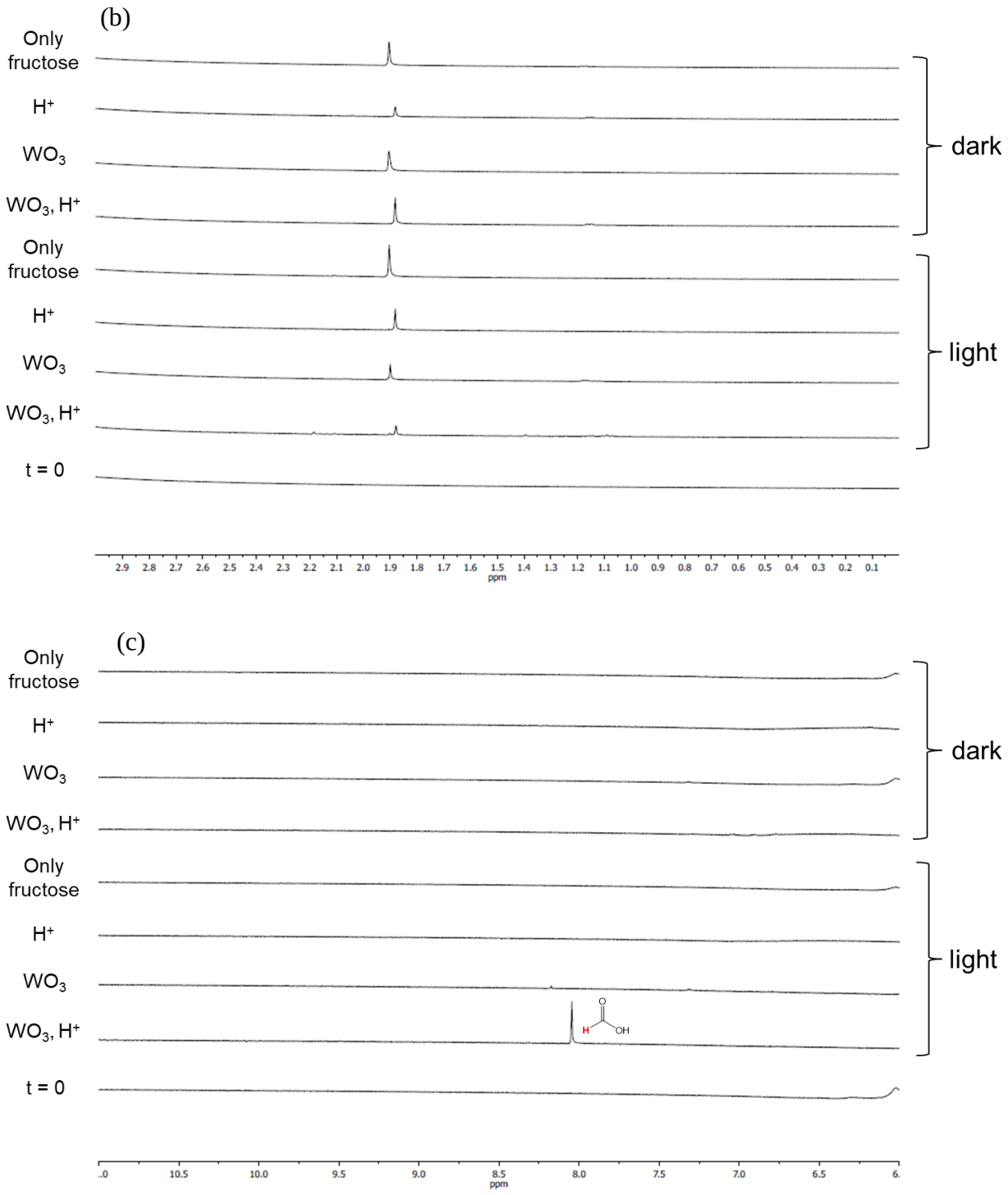

Figure 5.6: [1]H NMR spectra of aqueous solutions of fructose after being subjected to different reaction conditions. The zoomed-out spectrum (a) shows little change between the before and after reaction solutions. However, when zooming into between 0-3 ppm (b) a singlet at ~1.9 ppm is shown to appear after the reaction for all conditions. The reaction that was illuminated and contained WO_3 and acid was the only reaction to exhibit a peak at ~8.1 ppm, which is suspected to be formic acid (c).

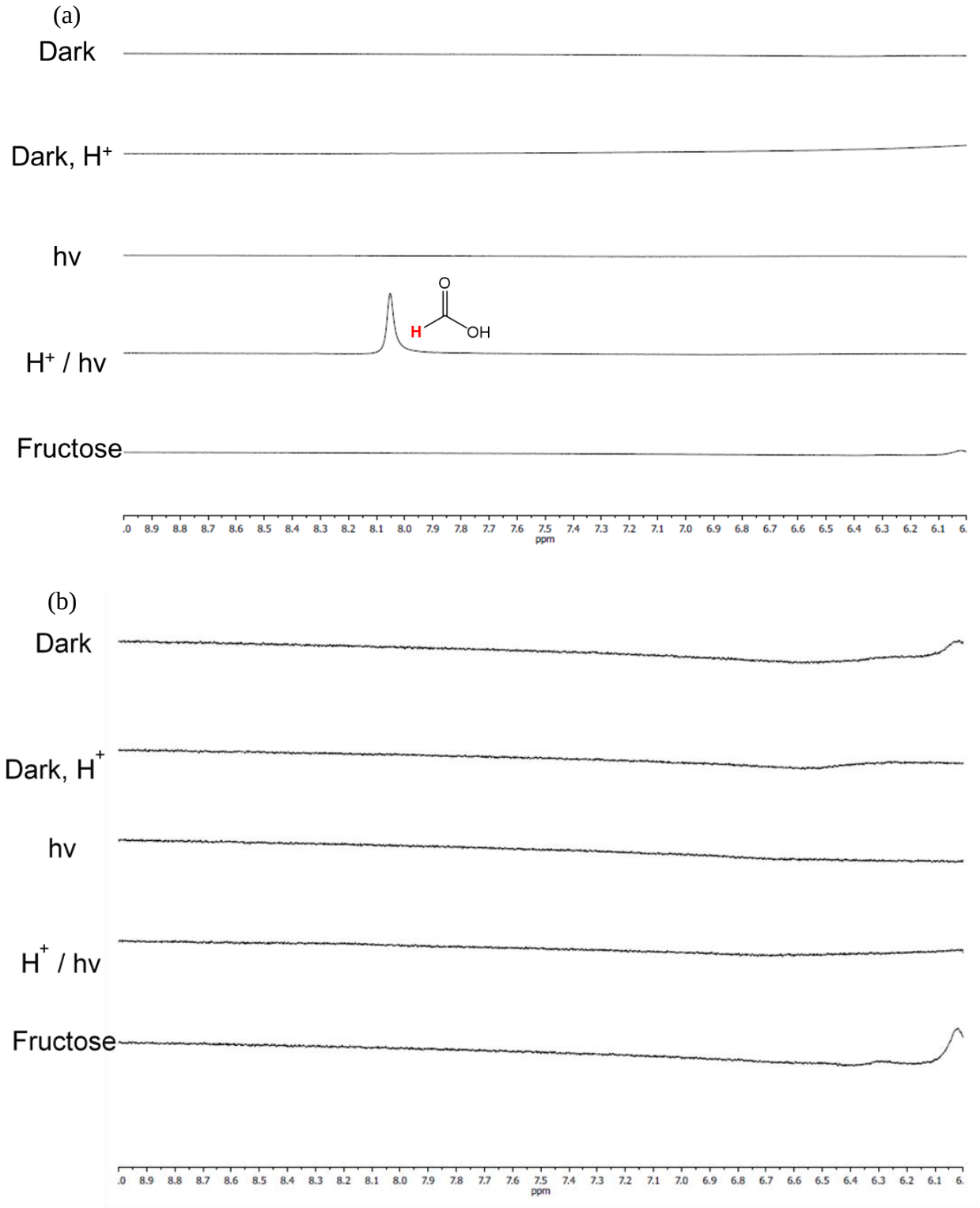

Figure 5.7: ^{1}H NMR spectra of aqueous solutions of fructose after being subjected to different reaction conditions with $BiVO_4$ (a) and $CuWO_4$ (b) used as the photocatalyst. $BiVO_4$ produced formic acid as a product of the reaction under illuminated acidic conditions, whereas $CuWO_4$ was unable to catalyze any reaction.

conditions are slow, it is interesting that only these conditions produced it. The reaction was also attempted to be catalyzed by both $BiVO_4$ and $CuWO_4$ powders. $BiVO_4$ showed the same reactivity, slowly generating formic acid when illuminated under acidic conditions (Figure 5.7 (a)). $CuWO_4$, however, showed no reactivity at all (Figure 5.7 (b)). When WO_3, $BiVO_4$, and $CuWO_4$ were utilized for glycerol oxidation under the same acidic conditions, WO_3 and $BiVO_4$ both again generated formic acid (Figure 5.8). However, $BiVO_4$ also oxidized one of the primary alcohols, generating glyceraldehyde as well. This is the compound that can undergo base-catalyzed dehydration to the enol that can undergo an intramolecular Cannizzaro reaction to produce lactate.

Seeing that it was possible to oxidize glycerol to glyceraldehyde, the reaction conditions were switched to basic conditions (0.25 M NaOH) and the base-stable metal oxide, Fe_2O_3, was utilized as the photocatalyst in an attempt to observe any further reactivity between glyceraldehyde and base in solution. While the catalysis was slow like the previous glycerol and fructose

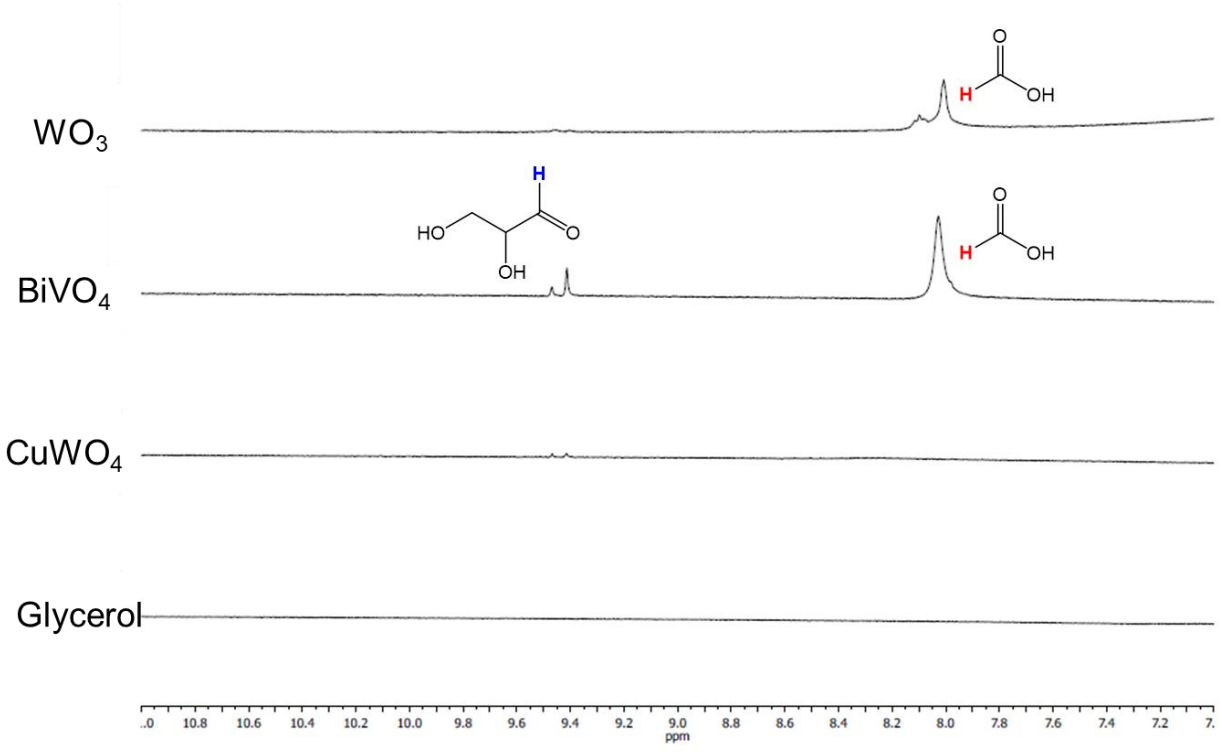

Figure 5.8: ^1H NMR spectra of aqueous solutions of glycerol after being stirred in 0.1 M HCl under illumination with different metal oxide catalysts.

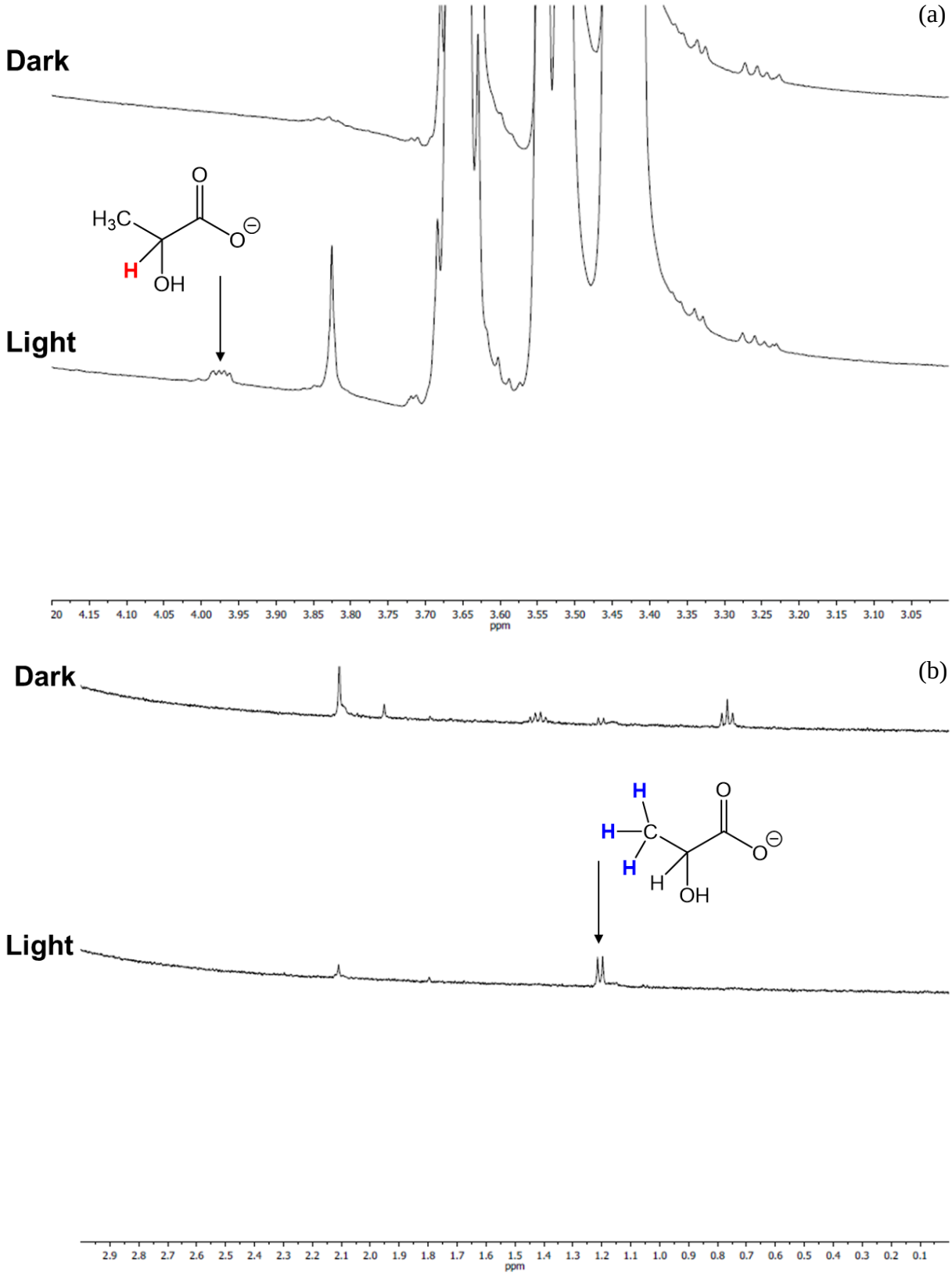

Figure 5.9: ^{1}H NMR spectra of aqueous solutions of glycerol after being stirred with Fe_2O_3 in 0.25 M NaOH under illumination and in the dark. The protons both alpha (a) and beta (b) to the carbonyl are observed.

oxidations, there were resonances observed in the ^{1}H NMR spectrum that were from lactate (Figure 5.9 (a) and (b)). This does happen to a lesser extent in the dark, though dark conditions lead to different byproducts. No other controls experiments (i.e. removal of base, catalyst, light, sacrificial oxidant) result in noticeable lactate formation. This reaction was also attempted to be completed with $LiNO_3$ as a mediator. $LiNO_3$ had been shown in our lab to be a successful mediator for benzyl alcohol oxidation on CdS.[24] However, when used under these conditions no major difference in reactivity was seen from the reactions where it had been excluded. Many other mediators (potassium halides, triethylamine, hydroquinone) were also utilized with no improvement in reactivity.

5.5 Photocatalytic Nonaqueous Oxidation of Benzylic and Saturated Alcohols on Bi_2WO_6

After collecting evidence of C-C bond cleavage in many previous alcohol oxidations (1-phenyl-1,2-ethanediol generating benzaldehyde as an oxidation product, fructose and glycerol producing formic acid), a group of alcohols was chosen to be photocatalytically oxidized on Bi_2WO_6 in acetonitrile under blue LED illumination to see that reactivity continued over other alcohols. Bi_2WO_6 was chosen as the photocatalyst due to its ability to absorb visible light (Bi_2WO_6 has a bandgap of ~2.8 eV, similar to WO_3) and reports of it being capable of oxidizing alcohols selectively in water.[25–29] The Bi_2WO_6 used in this work was synthesized through a hydrothermal preparation.[30] The phase purity and capability to absorb visible light were confirmed by powder X-ray diffraction and diffuse reflectance spectroscopy, respectively (Figure 5.10 (a) and (b)). The powder had a flakey microsphere morphology (Figure 5.10 (c)).

Bi_2WO_6 was first confirmed to oxidize benzyl alcohol under typical blue LED illuminated conditions with acetonitrile as the solvent (Figure 5.11 (a)). Then, two substrates were chosen to confirm that C-C bond cleavage occurs on Bi_2WO_6 – 1-phenylethanol and 1-phenyl-1,2-

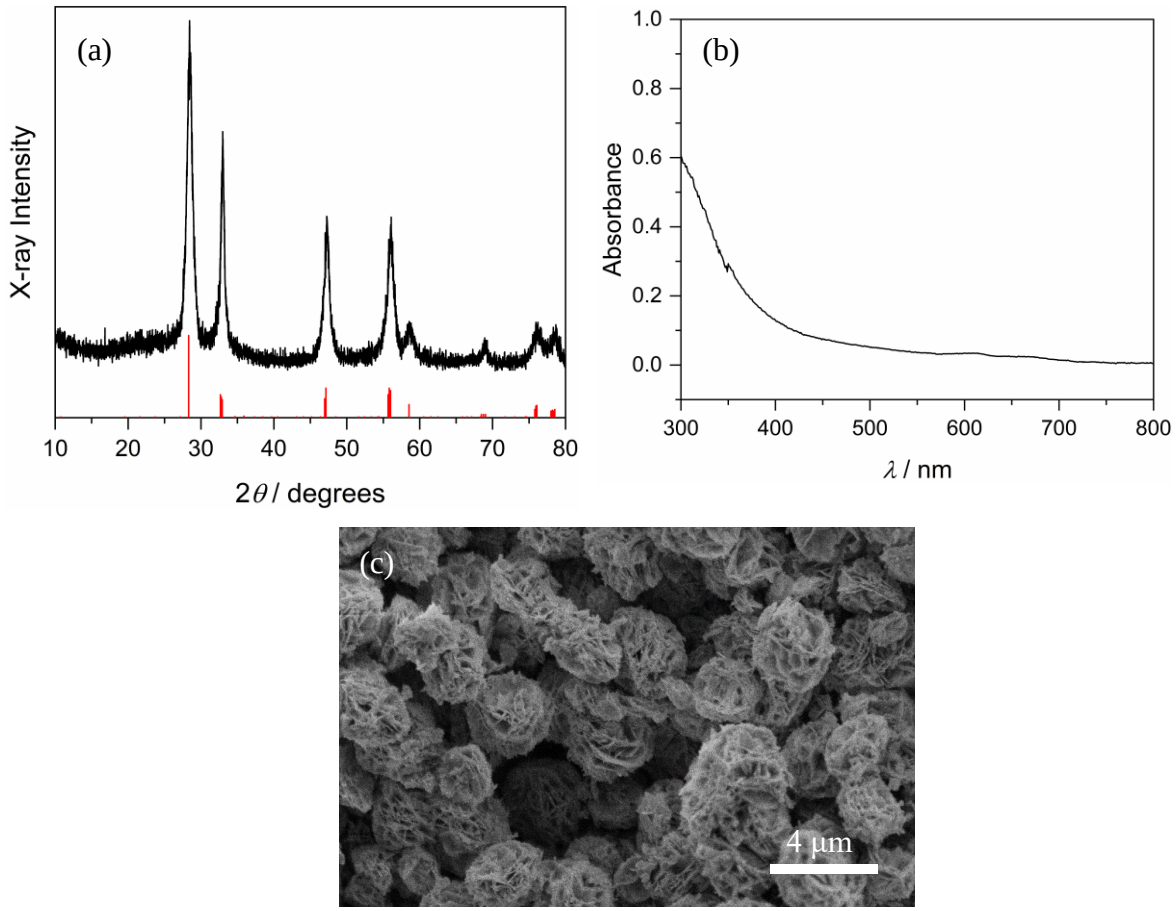

Figure 5.10: Power X-ray diffractogram (a), diffuse reflectance spectrum (b), and scanning electron micrograph (c) of Bi_2WO_6 microspheres used for photocatalytic alcohol oxidation. The red lines in the diffractogram represent the Bi_2WO_6 reference pattern (PDF#39-0256).

ethanediol. The oxidation product one would expect for 1-phenylethanol is acetophenone. However, benzaldehyde was the major product in this reaction (Figure 5.11 (b)). Similarly, the major product observed for the photocatalytic oxidation of 1-phenyl-1,2-ethanediol was benzaldehyde (Figure 5.11 (c)). A difference in these two reactions was that when they were run without catalyst, the 1-phenylethanol did not generate any products, but the 1-phenyl-1,2-ethanediol produced benzaldehyde (Figure 5.11 (d) and (e)). It may be that the O_2 (originally added to serve as the sacrificial oxidant, as done in the work in Chapter 4 of this thesis) is a strong enough oxidant that it can completely oxidize the primary alcohol on 1-phenyl-1,2-ethanediol to a carboxylic acid, where it can undergo decarboxylation (as discussed earlier in this chapter) to yield benzaldehyde as a product.

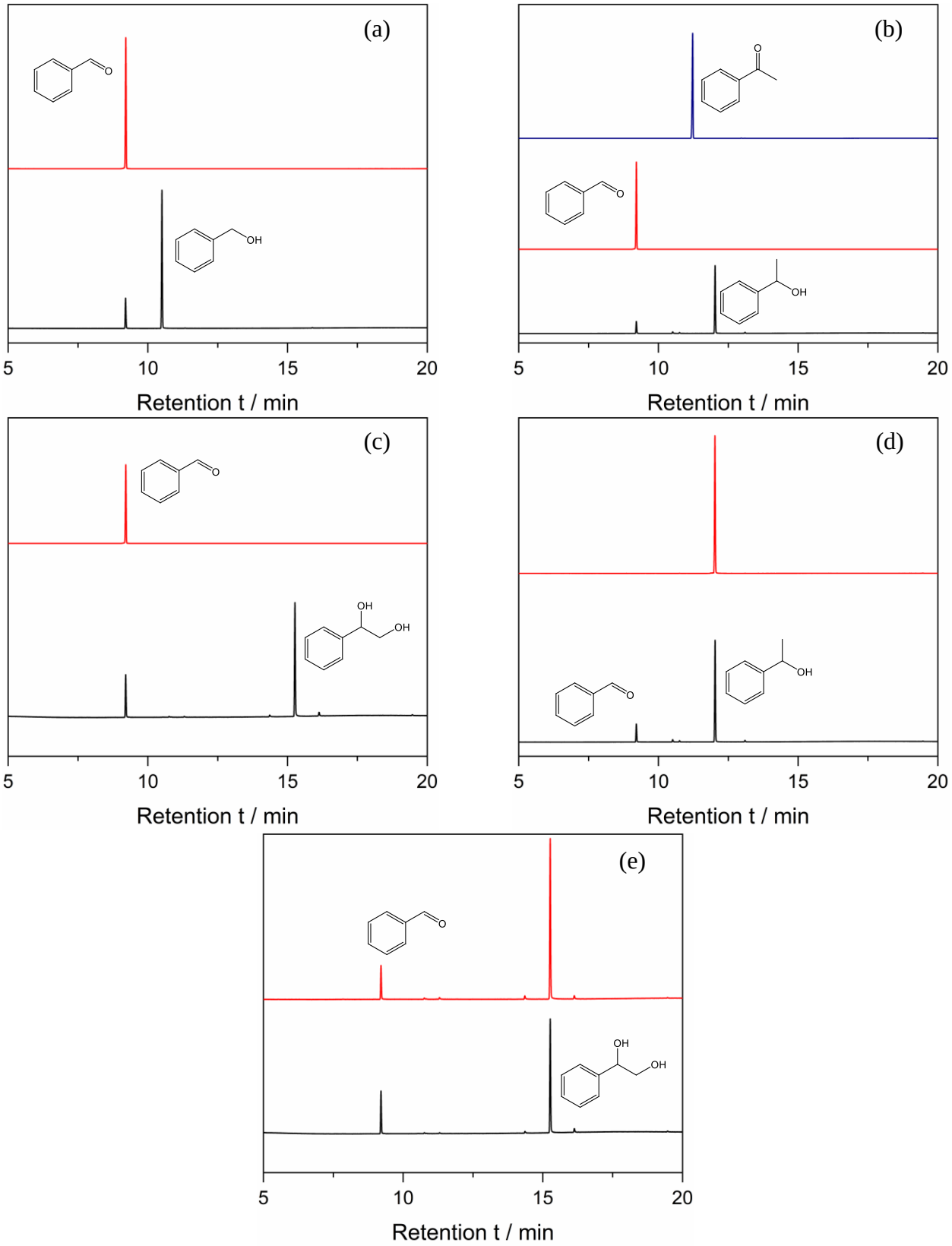

Figure 5.11: GC-FID traces for 48 h photooxidations of benzyl alcohol (a) 1-phenylethanol (b) and 1-phenyl-1,2-ethanediol (c) on Bi_2WO_6. GC-FID traces for illuminated non-catalyst containing solutions of 1-phenylethanol (d) and 1-phenyl-1,2-ethanediol (e). All black traces are reaction solutions. Red and navy traces are control injections of the shown compound.

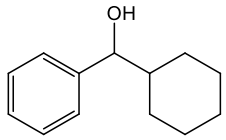

cyclohexyl(phenyl)methanol

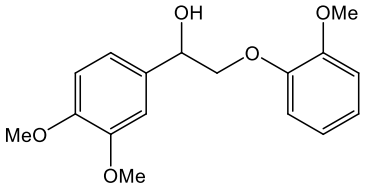

Lignin model compound

Figure 5.12: Chemical structures of cyclohexyl(phenyl)methanol and the lignin model compound (formally 1-(3,4-dimethoxyphenyl)-2-(2-methoxyphenoxy)ethan-1-ol) used in this work.

Next, the bulkiness of the R group on the benzylic position of benzyl alcohol was changed and the effect on the generation of benzaldehyde monitored. The two substrates chosen were cyclohexyl(phenyl)methanol and a lignin model compound (synthesized and donated by Gabe Magallanes from Corey Stephenson's lab) (Figure 5.12). The cyclohexyl(phenyl)methanol did produce benzaldehyde as a product (Figure 5.13 (a) and (b)). While the reaction rates for these alcohol oxidations were not quantified, the intensity of the signal of the resulting benzaldehyde from the cyclohexyl(phenyl)methanol oxidation was much less than that for the 1-phenylethanol oxidation, indicating a slower reaction. It was difficult to determine by GC-FID, but was confirmed through ^{1}H NMR, that the reaction also did produce the expected oxidation product of cyclohexyl phenyl ketone, resulting from the oxidation of the hydroxyl group to a carbonyl (Figure 5.13 (c)). To see if this trend in C-C bond cleavage could be applied to biomass degradation, a lignin model compound was subjected to photocatalytic reaction conditions. The lignin model compound represents a fragment of structural commonality between many different sources of lignin. The predictable and controllable degradation of known lignin linkages would be useful in the degradation of lignin and would further efforts to break down lignin into useful commodity chemicals. The Stephenson group has reported chemistry that allows for the selective cleavage of the ether linkage in the lignin model compound used here with a two-step electrocatalytic / photocatalytic process involving a homogenous iridium catalyst, but the cleavage of the C-C bond adjacent to this ether linkage was

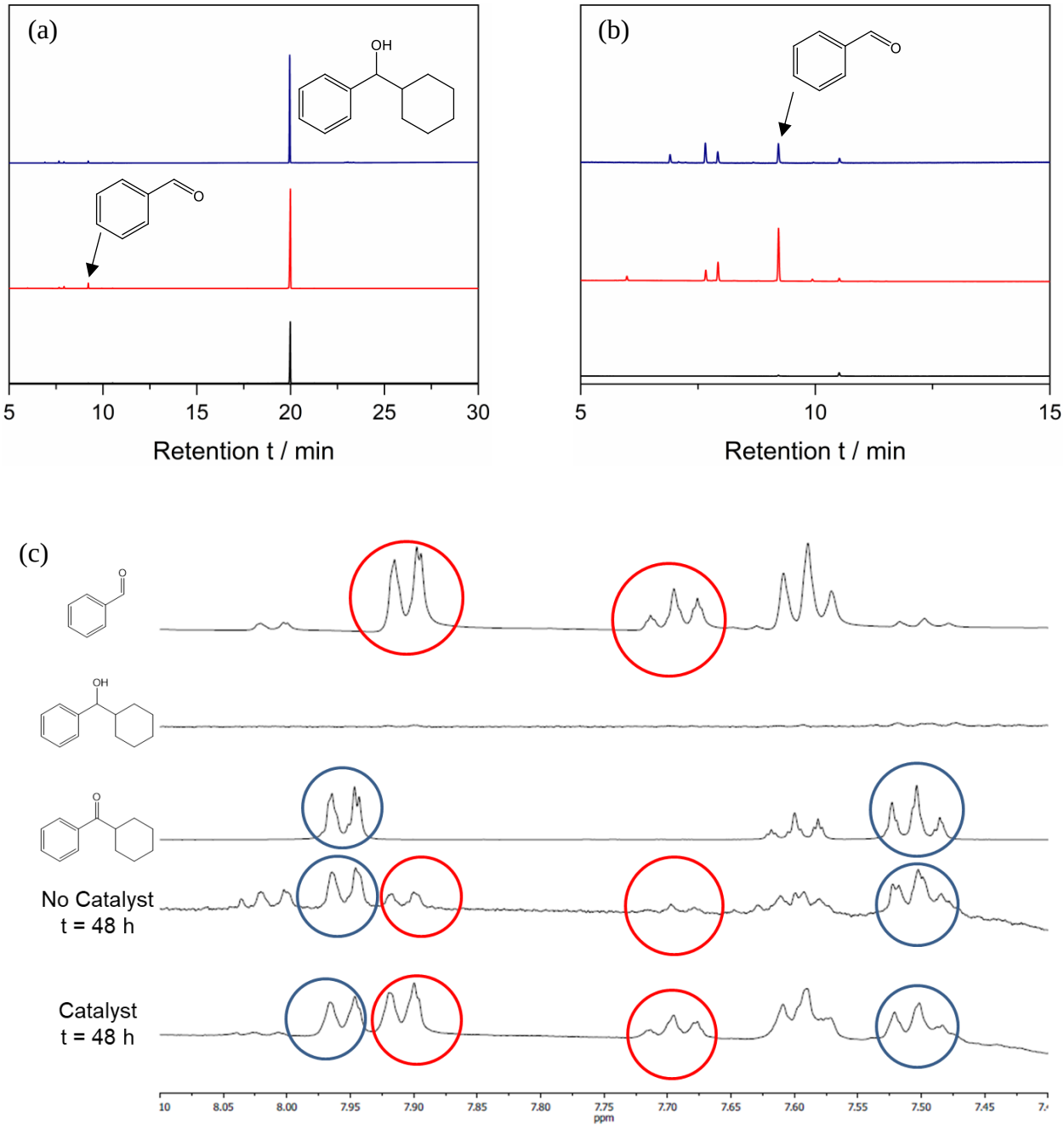

Figure 5.13: Full (a) and zoom-in (b) GC-FID traces and ^{1}H NMR spectra (c) of solutions of cyclohexyl(phenyl)methanol after being stirred for 48 hours with Bi_2WO_6 microspheres. Black traces in (a) and (b) are pre-catalysis, red traces are after a reaction with Bi_2WO_6 for 48 hours, and navy traces are after a reaction for 48 hours with no Bi_2WO_6. Red circles in (c) highlight resonances seen in benzaldehyde, while navy circles highlight resonances seen by cyclohexyl phenyl ketone.

not reported.[31] When stirred under blue LED irradiation for one week in acetonitrile with Bi_2WO_6 microspheres, no major reaction products are seen, with the majority of the lignin model compound unreacted (Figure 5.14 (a)). Curiously, the control reaction with no catalyst also shows the entirety

of the staring lignin material peak at 30.0 minutes disappear, with a peak of similar magnitude appearing at 30.4 minutes (Figure 5.14 (b)). It is unknown what structural changes took place during illumination under an O_2 atmosphere that caused this shift in the lignin model compound peak. The product of the expected C-C bond cleavage (3,4-dimethoxybenzaldehyde) is present is small quantities and was the only identifiable product (Figure 5.14 (c)). However, 3,4-dimethoxybenzaldehyde was also observed in the control reaction with no Bi_2WO_6 microspheres included. It is clear from these data that C-C bond cleavage to generate the aldehyde inherently

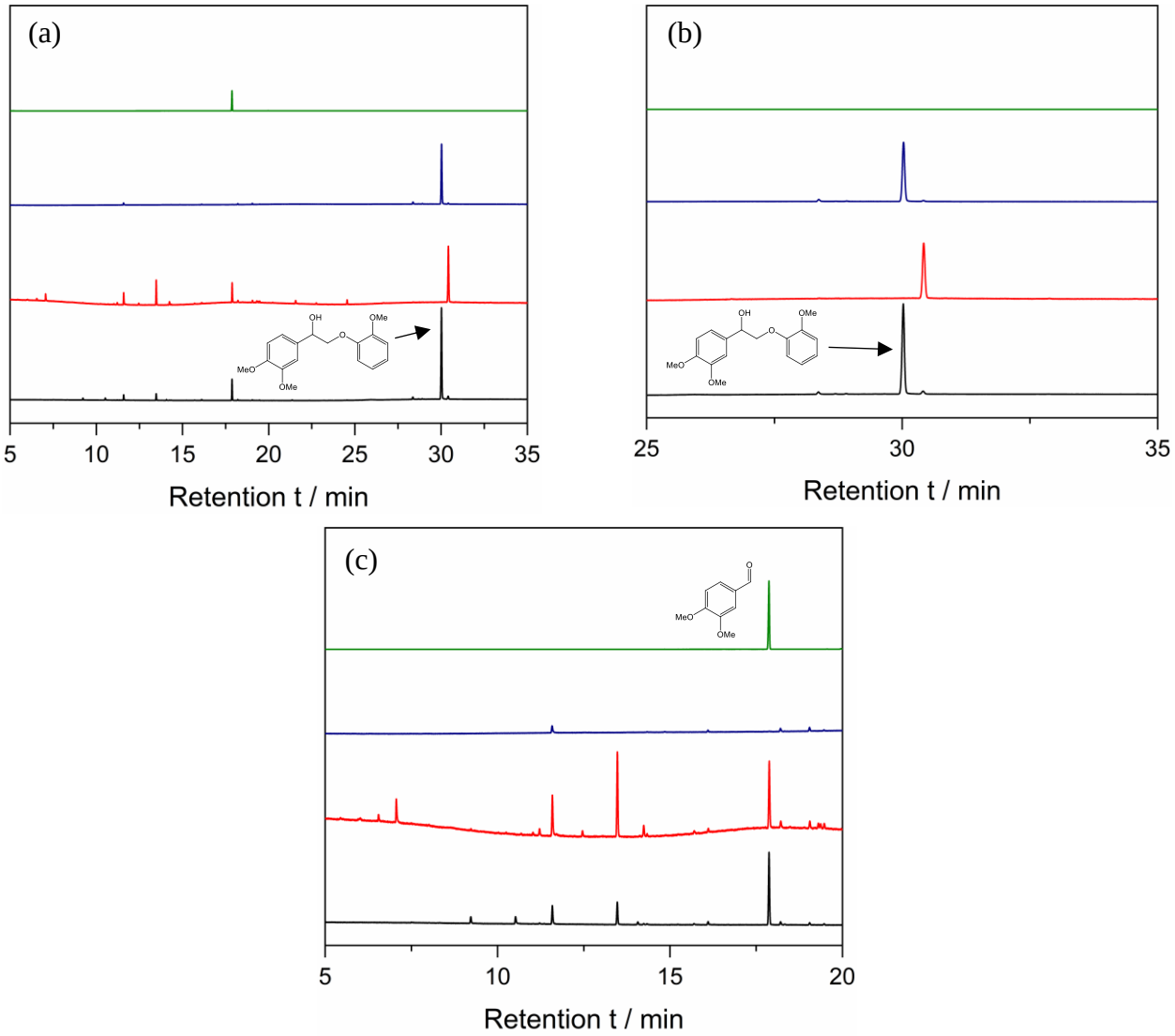

Figure 5.14: Full (a) and zoomed-in (b and c) GC-FID traces of solutions of lignin model compound after being stirred for 1 week with Bi_2WO_6 microspheres. The reaction with (black) and without (red) Bi_2WO_6 are compared to pure lignin model compound (navy) and the expected product of the C-C bond cleavage, 3,4-dimethoxybenzaldehyde (olive).

occurs at a slow rate when the lignin model compound is illuminated with blue LEDs in acetonitrile under an O_2 atmosphere, and that Bi_2WO_6 does not affect that rate.

The final pair of alcohols that served as starting compounds for photocatalytic oxidation by Bi_2WO_6 were 2-hexanol and cyclohexanol. These were both saturated secondary alcohols. Neither of these alcohols have any activated positions that would stabilize any intermediates (e.g. the benzylic position on benzyl alcohol), so the driving force for oxidation is less pronounced. If Bi_2WO_6 were a selective catalyst, only the ketones were expected to result from photocatalytic oxidation. However, C-C bond cleavage was considered as a possibility. If this occurred in 2-hexahol, one could expect pentanal as the product. If it occurred during the oxidation of cyclohexanol, one would expect the ring to be broken and to form hexanal. However, no evidence of C-C bond cleavage was observed for either alcohol (Figure 5.15 (a) and (b)). The reaction with 2-hexanol produced 2-hexanone alone, but at a slow rate. Similar reactivity was observed during the oxidation of cyclohexanol, which only formed small quantities of cyclohexanone. The observation of the expected alcohol to ketone transformations seen for the saturated alcohols here

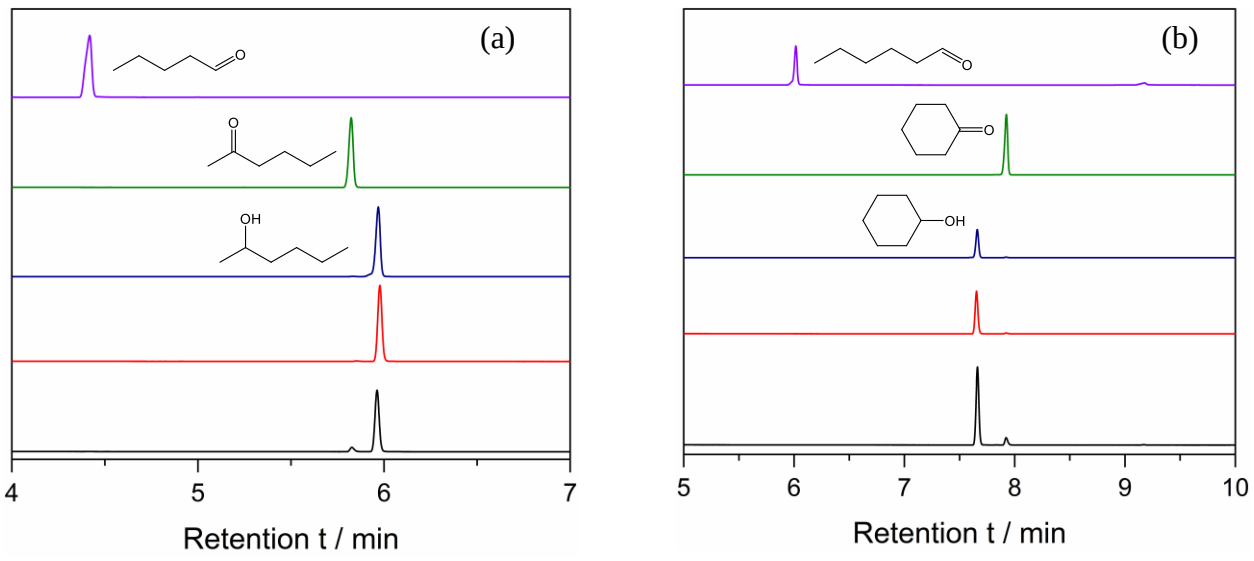

Figure 5.15: GC-FID traces of solutions of 2-hexanol (a) and cyclohexanol (b) after being stirred for 73 hours with Bi_2WO_6 microspheres. The reaction with (black) and without (red) Bi_2WO_6 are compared to injections of known compounds (navy, olive, and violet).

but not for the benzylic alcohols discussed above suggests that having one of the carbons in the C-C bonds that slowly cleaved in the case of the benzylic alcohols at the benzylic position was responsible for that reactivity.

5.6 Conclusions

It was hypothesized that the product distribution of the photocatalytic oxidation of 1-phenyl-1,2-ethanediol on TiO_2 would differ based on the crystal phase of TiO_2 that was used as the catalyst. When anatase, rutile, and P25 TiO_2 were compared for this reaction with water as the solvent, benzaldehyde was the main product for anatase and P25, while rutile did not make benzaldehyde at all. The appearance of benzaldehyde as a product was surprising, though it may be explained by the complete oxidation of the primary alcohol to a carboxylic acid, which then undergoes decarboxylation. All TiO_2 phases oxidized the secondary hydroxyl group, with rutile being the only catalyst that produced appreciable quantities of two unidentifiable compounds at larger retention times. When acetonitrile was used as the solvent, rutile was the only TiO_2 catalyst that formed benzaldehyde, with each phase again oxidizing the secondary hydroxyl group. No TiO_2 phase produced only a single product from the oxidation in either solvent.

When attempting photocatalytic oxidation of fructose (a product of the acid-catalyzed degradation of cellulose) on WO_3, $BiVO_4$, and $CuWO_4$, under neutral and acidic aqueous conditions, the WO_3 and $BiVO_4$ formed formic acid slowly. To be generated, the formic acid required all three illumination, catalyst, and light. Using $CuWO_4$ as the photocatalyst, however, resulted in no reaction with fructose. Under basic conditions, Fe_2O_3 was observed to oxidize glycerol (a waste product from the production of biodiesel) to latctate, albeit extremely slowly.

Following up on observations of C-C bond cleavage in the oxidation of fructose and 1-phenyl-1,2-ethanediol, Bi_2WO_6 was utilized for the photocatalytic oxidation of some benzylic and

saturated alcohols under nonaqueous conditions. Benzaldehyde was not only observed as the major product of 1-phenyl-1,2-ethanediol oxidation as with TiO_2, but also as the major product of 1-phenylethanol oxidation. The methyl group on the benzylic position must somehow be removed for benzaldehyde to be generated. The mechanism of this is unknown. When the methyl group of 1-phenylethanol was exchanged with a cyclohexyl group, benzaldehyde was yet again seen as the major product, though this reaction was slow. Also, while benzaldehyde was produced in a control reaction with no catalyst, the reaction with Bi_2WO_6 occurred at a greater rate, qualitatively. The attempt to utilize this C-C bond cleavage to release a group from the benzylic position of a molecule failed when applied to a lignin model compound. While this cleavage did slowly take place over the course of a week, the rates of the reactions with and without catalyst were approximately similar based on the amount of product formed. When the saturated alcohols 2-hexanol and cyclohexanol were subjected to photocatalytic oxidation conditions, the respective ketones resulted as the exclusive products in low quantities in both cases.

5.7 Experimental

Materials and Methods

Anatase TiO_2, glycerol (Certified ACS, Fisher Chemical), sodium hydroxide (ACS reagent, ≥97.0%, pellets), 1-phenylethanol (98%), WO_3 (nanoparticles, <100 nm), and sodium perchlorate (ACS reagent, ≥98.0%) were purchased from Sigma. P25 TiO_2 was purchased from Evonik. Fe_2O_3 (30-50 nm, Alfa Aesar), Acetonitrile (ACS Certified), 1-phenyl-1,2-ethanediol (97%, ACROS Organics), D-fructose (99%, Alfa Aesar), hydrochloric acid (Certified ACS Plus, 36.5 to 38.0%, Fisher Chemical), cyclohexyl phenyl ketone (98%, Alfa Aesar), and sodium borohydride (powder) were purchased from Fisher. The lignin model compound (1-(3,4-dimethoxyphenyl)-2-(2-methoxyphenoxy)ethan-1-ol*)* was synthesized and donated to this work by Gabe Magallanes from

the Corey Stephenson lab. The Stephenson lab has previously reported the synthesis of this compound.[31] All water was filtered through a Millipore filtration system to give water with a resistance of 18.2 MΩ • cm^{-2} before use in experiments.

Materials Characterization

Powder X-ray diffraction data were collected on a Panalytical Empyrean diffractometer at a power of 1.8 kW (45 kV, 40 mA) with Cu Kα (λ = 1.5418 nm) radiation. The detector was a X'Celerator Scientific, a position sensitive 1D detector equipped with Bragg-Brentano^{HD} x-ray optic delivering only Kα radiation. Patterns were collected with a sampling step of 0.020 and a scan rate of 0.080°• s^{-1} while spinning at a rate of 0.25 Hz. A Zeiss LEO 1455VP scanning electron microscope was used to image powders at a working distance of 5 mm. A Varian Cary 5000 spectrophotometer equipped with an external diffuse reflectance accessory was used for UV-vis measurements. Spectra were collected in reflectance mode and transformed into absorbance using the Kubelka-Monk function. Barium sulfate was used as a 100% reflectance standard.

Catalyst Preparation

Rutile TiO_2

Rutile TiO_2 was prepared according to a report by Palmisano and coworkers.[23] All quantities used here were a quarter of those reported. A volume of 5 mL of $TiCl_4$ was added dropwise to 250 of Milli-Q water in a 500 mL round bottom flask. No stirring was taking place during the addition of $TiCl_4$. After all $TiCl_4$ had been added, the solution was stirred for two minutes. After the stir bar was removed the round bottom flask was sealed with a glass stopper and parafilm and stored in a cabinet, undisturbed, for 6 days. The suspension was placed into 50 mL centrifuge tubes and was

centrifuged and decanted. The precipitated TiO_2 was then washed with Milli-Q water by vortexing and was then centrifuged and decanted again. Three water washes were done before the powder was dried in a vacuum oven at 60 °C overnight.

$BiVO_4$

Bismuth vanadate was synthesized by grinding a 1:1 mole ratio of ammonium metavanadate (0.500 g) and bismuth (III) nitrate pentahydrate (2.07 g) for 10 minutes. This was heated in a muffle furnace at 500 °C for 6 hours. The oven temperature ramped up to and down from 500 °C at a rate of 10 °C • min^{-1}. The powder was then placed in a 12 mL polypropylene centrifuge with 7 mL of Milli-Q (18.2 MΩ•cm^{-1}) water and vortexed for about 30 seconds before centrifuging at 3500 rpm for 5 minutes. The water was then decanted and the process was repeated twice more. The powder was then washed three times with ethanol before drying overnight in a vacuum oven at 60 °C.

$CuWO_4$

Copper tungstate was synthesized by grinding a 1:1 mole ratio of copper (II) oxide (0.51 g) and tungsten oxide (1.49 g) in a mortar and pestle for 15 minutes followed by heating in a muffle furnace at 800 °C for 6 hours. The oven temperature ramped up to and down from 800 °C at a rate of 10 °C • min^{-1}. The powder was then placed in a 12 mL polypropylene centrifuge with 7 mL of Milli-Q (18.2 MΩ•cm^{-1}) water and vortexed for about 30 seconds before centrifuging at 3500 rpm for 5 minutes. The water was then decanted and the process was repeated twice more. The powder was then washed three times with ethanol before drying overnight in a vacuum oven at 60 °C.

Bi_2WO_6

Followed a procedure outlined by Leung, M. K. H. and coworkers.[30] Dissolved 970 mg of $Bi(NO_3)_3 • 5H_2O$ in 10 mL of 1.2 M HNO_3 through sonicating / stirring. $Bi(NO_3)_3$ did not dissolve

readily. Next, 330 mg of $Na_2WO_4 \bullet 2H_2O$ was then dissolved in 10 mL of H_2O and added to the $Bi(NO_3)_3$ solution dropwise while stirring, forming a precipitate. Then 20 mL of H_2O was added to give a final volume of 40 mL. A volume of 20 mL of this was transferred to a microwave tube (30 mL capacity) with a stir bar and microwaved at a ramp rate of 24 °C • min^{-1} to a final temperature of 170 °C, where it was held for 30 minutes. It was then cooled to 55 °C as fast as possible. Stirring at 800 rpm was conducted throughout the entire microwave process. The suspension was then placed into a 50 mL polypropylene centrifuge tube, centrifuged, and decanted. The resulting powder was vortexed with DI water, centrifuged and decanted. The powder was washed a total of three times with DI water and three times with 200 proof ethanol before being dried in a vacuum oven at 60 °C overnight.

Cyclohexyl(phenyl)alcohol Synthesis

The synthesis of cyclohexyl(phenyl)alcohol was accomplished through the reduction of cyclohexyl(phenyl)ketone. A quantity of 300 mg (1.59 mmol) of cyclohexyl(phenyl)ketone was added to a 4 mL dram vial that contained 1.8 mL of THF a stir bar. This was stirred in an ice bath and 2 mol equivalents (120 mg, 3.18 mmol) of sodium borohydride was slowly added. The sodium borohydride is not completely soluble. The suspension was stirred and a volume of 0.3 mL of water was added. This dissolved the remaining sodium borohydride. Another mol equivalent (60 mg, 1.59 mmol) of sodium borohydride was slowly added while stirring. The dram vial was taken out of the ice bath and allowed to warm to room temperature while maintaining stirring. Another mol equivalent of sodium borohydride was then added. This was stirred at room temperature overnight capped with a rubber septum pierced with a needle. After the overnight stirring, the

solvent was removed with a stream of nitrogen gas. Complete conversion of the ketone to the alcohol was confirmed by ^{1}H NMR.

Photocatalytic Oxidation of 1-phenyl-1,2-ethanediol

The acetonitrile and water used for these experiments was sparged with O_2 prior to use. A volume of 10 mL of 50 mM 1-phenyl-1,2-ethanediol solution was placed into a quartz tube with 40 mg of TiO_2 and a stir bar. The tube was capped with a rubber septum, parafilmed, and had a balloon of O_2 attached to it. This was placed in front of a xenon arc lamp (no filter) an illuminated with a power density of ~100 mW • cm^{-2}. The reaction was stirred under illumination for 12 hours. For reactions run in acetonitrile, the solution was then filtered through a syringe filter to remove the TiO_2 and then the acetonitrile was then removed under a stream of nitrogen. ~4 mL of acetonitrile was added back to the container, and 500 uL of this placed into a GC vial already containing 500 uL of fresh acetonitrile. All GC-MS data were collected on a Shimadzu QP-2010 GC-MS. Sample injection volumes of 5 µL were used. The column attached to the instrument was a DB-5 ms column with a length of 30 m, a thickness of 0.25 µm, and a diameter of 0.25 mm. The temperature for GC-MS runs was started at 50 °C, held for 3 minutes, then ramped up to 300 °C at a rate of 20 °C • min^{-1}, and then held for 10 minutes before ending the run. If the catalysis was run in water, after the reaction the suspension was extracted three times with diethyl ether. The ether was filtered through a syringe filter to remove any remaining TiO_2. The ether was removed under a stream of nitrogen. ~4 mL of acetonitrile was added back to the container, and 500 uL of this placed into a GC vial already containing 500 uL of fresh acetonitrile. The GC-MS data was collected the same as that described above.

Photocatalytic Oxidation of Fructose and Glycerol

Fructose and Glycerol Oxidation under Neutral or Acidic Conditions

All photocatalytic reactions were carried out in a custom-built aluminum LED assembly (Figure S1). Royal blue LEDs (λ_{max} = 448 nm) with a power rating of 1.03 W were purchased from Mouser Electronics (Mouser Part#: 997-LXML-PR02-A900). Reactions contained 20 mg of catalyst, 2 mL of 250 mM aqueous fructose or glycerol solution (either with an unadjusted pH or containing 0.1 M HCl), and were run in 4 mL dram vials that had their flat bottoms visible to the LEDs while receiving a power density of 200 mW • cm^{-2}. Reactions were capped with rubber septa and were kept under O_2 using a balloon. The reactions were stopped after 24 hours of stirring and all dram vials were put in 50 mL polypropylene centrifuge tubes with a Kimwipe on the bottom and centrifuged at 2500 rpm for 5 minutes. To prepare NMR samples, 500 µL of the centrifuged reaction solution was added to an NMR tube containing 100 µL of D_2O. All ^1H NMR experiments had solvent suppression conducted and were carried out on a Varian MR400 NMR spectrometer equipped with a Varian 5 mm Dual Broadband probe. All NMR data were processed in MestReNova software.

Glycerol Oxidation under Basic Conditions

These were carried out in a similar fashion to the above fructose and glycerol oxidations, except that the glycerol solution was 0.250 M in NaOH, 0.500 M $NaClO_4$ was used as the sacrificial oxidant in place of O_2, and Fe_2O_3 was the only catalyst used. The switch to $NaClO_4$ as the sacrificial oxidant was driver by experiments not discussed in this thesis that showed that among various sacrificial oxidants (including O_2) in the photocatalytic oxidation of 1-propanol on $CuWO_4$, $NaClO_4$ offered the narrowest product distribution.

Photocatalytic Oxidation of Benzylic and Saturated Alcohols on Bi_2WO_6

These reactions were run on the custom blue LED setup described above. Reactions contained 20 mg of Bi_2WO_6 microsphere catalyst, 2 mL of 250 mM alcohol solution in acetonitrile solvent and were run in 4 mL dram vials that had their flat bottoms visible to the LEDs while receiving a power density of 200 mW • cm^{-2}. Since no density information could be found for cyclohexyl(phenyl) alcohol, ~250 uL of this alcohol was dissolved in acetonitrile instead. The lignin model compound was used in a concentration of 50 mM and 50 mg of Bi_2WO_6 was used as the quantity of catalyst. Reactions were capped with rubber septa and were kept under O_2 using a balloon. Reactions with benzyl alcohol, 1-phenylethanol, 1-phenyl-1,2-ethanediol, and cyclohexyl(phenyl) alcohol were all run for 48 hours. The 2-hexanol and cyclohexanol were reacted for 73 hours. The lignin model compound was reacted for 1 week. After the reactions were complete, the dram vials were put in 50 mL polypropylene centrifuge tubes with a Kimwipe on the bottom and centrifuged at 2500 rpm for 5 minutes. To prepare GC-FID samples, 10 µL of the centrifuged reaction solution was added to a GC vial containing 990 µL of acetonitrile. For the lignin model compound and cyclohexyl(phenyl) alcohol reactions, 50 µL of the solution was added to a GC vial containing 950 µL of acetonitrile. GC-FID analysis was conducted on a Trace 1310 GC-FID system with a TG-5MS Amine column. Argon was used as the carrier gas. The heating method used for analysis was to ramp from 40 °C to 300 °C at a rate of 10 °C • min^{-1} and hold at 300 °C for 10 minutes before cooling.

5.8 References

[1] Lang, X.; Ma, W.; Chen, C.; Ji, H. and Zhao, J. Selective Aerobic Oxidation Mediated by TiO_2 Photocatalysis. *Accu. Chem. Res.* **2014**, *47*, 355-363.

[2] Yurdakal, S.; Palmisano, G.; Loddo, V.; Alagöz, O.; Augugliaro, V. and Palmisano, L. Selective photocatalytic oxidation of 4-substituted aromatic alcohols in water with rutile TiO_2 prepared at room temperature. *Green Chem.* **2009**, *11*, 510-516.

[3] Augugliaro, V.; Loddo, V.; López-Muñoz, M. J.; Márquez-Álvarez, C.; Palmisano, G.; Palmisano, L. and Yurdakal, V. Home-prepared anatase, rutile, and brookite TiO_2 for selective photocatalytic oxidation of 4-methoxybenzyl alcohol in water: reactivity and ATR-FTIR study. *Photochem. Photobiol. Sci.* **2009**, *8*, 663-669.

[4] Pan, X.; Zhang, N.; Fu, X. and Xu, Y.-J. Selective oxidation of benzyl alcohol over TiO_2 nanosheets with exposed {0 0 1} facets: Catalyst deactivation and regeneration. *Appl. Catal., A* **2013**, *453*, 181-187.

[5] Fujishima, A. and Honda, K. Electrochemical Photolysis of Water at a Semiconductor Electrode. *Nature* **1972**, *238*, 37-38.

[6] Luttrell, T.; Halpegamage, S.; Tao, J.; Kramer, A.; Sutter, E. and Batzill, M. Why is anatase a better photocatalyst than rutile? – Model studies on epitaxial TiO_2 films. *Sci. Rep.* **2014**, *4*, 4043: 1-7.

[7] Hodes, G. and Kamat, P. V. J. Understanding the Implication of Carrier Diffusion Length in Photovoltaic Cells. *Phys. Chem. Lett.* **2015**, *6*, 4090–4092.

[8] Yamada, Y. and Kanemitsu, Y. Determination of electron and hole lifetimes of rutile and anatase TiO_2 single crystals. *Appl. Phys. Lett.* **2012**, *101*, 133907-1 – 133907-4.

[9] Bockris, J. O.; Reddy, A. K. N. *Modern Electrochemistry 2B: Electrodics in Chemistry, Engineering, Biology and Environmental Science, Volume 2*; Springer Science & Business Media, 2001.

[10] Liu, M.; de Leon Snapp, N. and Park, H. Water photolysis with a cross-linked titanium dioxide nanowire anode. *Chem. Sci.* **2011**, *2*, 80–87.

[11] Mi, Y. and Weng, Y. Band Alignment and Controllable Electron Migration between Rutile and Anatase TiO_2. *Sci. Rep.* **2015**, *5*, 11482: 1-10.

[12] Hendry, E.; Wang, F.; Shan, J.; Heinz, T. F. and Bonn, M. Electron transport in TiO_2 probed by THz time-domain spectroscopy. *Phys. Rev. B* **2004**, *69*, 081101-1 – 081101-4.

[13] Yagi, E.; Hasiguti, R. and Aono, M. Electronic conduction above 4 K of slightly reduced oxygen-deficient rutile TiO_{2-x}. *Phys. Rev. B* **1996**, *54*, 7945–7956.

[14] Huang, Y.-B. and Fu, Y. Hydrolysis of cellulose to glucose by solid acid catalysts. *Green Chem.* **2013**, *15*, 1095-1111.

[15] Lu, Z.; Demianets, I.; Hamze, R.; Terrile, N. J. and Williams, T. J. A Prolific Catalyst for Selective Conversion of Neat Glycerol to Lactic Acid. *ACS Catal.* **2016**, *6*, 2014-2017.

[16] Sharninghausen, L. S.; Campos, J.; Manas, M. G. and Crabtree, R. H. Efficient selective and atom economic catalytic conversion of glycerol to lactic acid. *Nat. Commun.* **2014**, *5*, 5084-1 – 5084-9.

[17] Zhang, M.; Wang, Q.; Chen, C.; Zang, L.; Ma, W. and Zhao, J. Oxygen Atom Transfer in the Photocatalytic Oxidation of Alcohols by TiO_2: Oxygen Isotope Studies. *Angew. Chem. Int. Ed.* **2009**, *48*, 6081-6084.

[18] Jin, B.; Yao, G.; Wang, X.; Ding, K. and Jin, F. Photocatalytic Oxidation of Glucose into Formate on Nano TiO_2 Catalyst. *ACS Sustainable Chem. Eng.* **2017**, *5*, 6377-6381.

[19] Shen, F.; Smith Jr., R. L.; Li, L.; Yan, L. and Qi, X. Eco-friendly Method for Efficient Conversion of Cellulose into Levulinic Acid in Pure Water with Cellulase-Mimetic Solid Acid Catalyst. *ACS Sustainable Chem. Eng.* **2017**, *5*, 2421-2427.

[20] Singh, A. K.; Singh, S. and Kumar, A. Hydrogen energy future with formic acid: a renewable chemical hydrogen storage system. *Catal. Sci. Technol.* **2016**, *6*, 12-40.

[21] Müller, K.; Brooks, K. and Autrey, T. Hydrogen Storage in Formic Acid: A Comparison of Process Options. *Energy Fuels* **2017**, *31*, 12603-12311.

[22] Werpy, T. and Pertersen, G. *Top Value Added Chemicals from Biomass: Volume I – Results of Screening for Potential Candidates from Sugars and Synthesis Gas*; DOE/GO-102004-1992; U.S. Department of Energy: Oak Ridge, TN, 2004.

[23] Yurdakal, S.; Tek, B. S.; Alagöz, O.; Augugliaro, V.; Loddo, V.; Palmisano, G. and Palmisano, L. Photocatalytic Selective Oxidation of 5-(Hydroxymethyl)-2-furaldehyde to 2,5-Furandicarbaldehyde in Water by Using Anatase, Rutile, and Brookite TiO_2 Nanoparticles. *ACS Sustainable Chem. Eng.* **2013**, *1*, 456-461.

[24] DiMeglio, J. L.; Breuhaus-Alvarez, A. G.; Li, S. and Bartlett, B. M. Nitrate Mediated Alcohol Oxidation on Cadmium Sulfide Photocatalysts. *ACS Catal.* **2019**, *9*, 5732-5741.

[25] Zhang, Y.; Zhang, N.; Tang, Z.-R. and Xu, Y.-J. Identification of Bi_2WO_6 as a highly selective visible-light photocatalyst toward oxidation of glycerol to dihydroxyacetone in water. *Chem. Sci.* **2013**, *4*, 1820-1824.

[26] Qamar, M.; Elsayed, R. B.; Alhooshani, K. R.; Ahmed, M. I. and Bahnemann, D. W. Highly Efficient and Selective Oxidation of Aromatic Alcohols Photocatalyzed by Nanoporous Hierarchical Pt/Bi_2WO_6 in Organic and Solvent-Free Environment. *ACS Appl. Mater. Interfaces* **2015**, *7*, 1257-1269.

[27] Saison, T.; Gras, P.; Chemin, N.; Chanéac, C.; Durupthy, O.; Brezová, V.; Colbeau-Justin, C. and Jolivet, J.-P. New Insights into Bi_2WO_6 Properties as a Visible-Light Photocatalyst. *J. Phys. Chem. C* **2013**, *117*, 22656-22666.

[28] Dittmer, A.; Menze, J.; Mei, B.; Strunk, J.; Luftman, H. S.; Gutkowski, TR.; Wachs, I. E.; Schuhmann, W. and Muhler, M. Surface Structure and Photocatalytic Properties of Bi2WO6 Nanoplatelets Modified by Molybdena Islands from Chemical Vapor Deposition. *J. Phys. Chem. C* **2016**, *120*, 18191-18200.
[29] Zhang, Y. and Xu, Y.-J. Bi_2WO_6: A highly chemoselctive visible light photocatalyst toward aerobic oxidation of benzylic alcohols in water. *RSC Adv.* **2014**, *4*, 2904-2910.
[30] Li, G.; Zhang, D.; Yu, J. C. and Leung, M. K. H. An Efficient Bismuth Tungstate Visible-Light-Driven Photocatalyst for Breaking Down Nitric Oxide. *Environ. Sci. Technol.* **2010**, *44*, 4276-4281.
[31] Bosque, I.; Magallanes, G.; Rigoulet, M.; Kärkäs, M. D. and Stephenson, C. R. J. Redox Catalysis Facilitates Lignin Depolymerization. *ACS Cent. Sci.* **2017**, *3*, 621-628.

Chapter 6 Conclusions and Outlook

6.1 Summary of Presented Work and Reasonable Next Research Steps

The major conclusions from the experiments described in this thesis are:

1. The mechanism of photoelectrocatalytic water oxidation on WO_3 is affected by the photodeposition of a FeOOH layer.
2. Iron and nickel oxyhydroxide-coated WO_3 materials do not increase the Faradaic efficiency for aqueous photocatalytic benzyl alcohol oxidation compared to that observed for bare WO_3.
3. $CuWO_4$ photoanodes can act as photoelectrocatalysts for amine oxidation in nonaqueous conditions, though the high selectivity seen for oxidation of a 1° amine drops when a 2° amine is oxidized.
4. $CuWO_4$ powder is a selective and recyclable photocatalyst for the aerobic oxidation of benzylamine in nonaqueous conditions with a rate constant 1^{st} order in benzylamine that is half that observed for $BiVO_4$ powder.
5. The crystalline phase of TiO_2 does affect the product distribution resulting from the photocatalytic oxidation of 1-phenyl-1,2-ethanediol.
6. Formic acid was observed as a product in the photocatalytic oxidation of fructose and glycerol in acidic conditions on WO_3 and $BiVO_4$, while Fe_2O_3 was able to very slowly oxidize glycerol to lactate under basic conditions.

The work in Chapter 2 corroborates earlier hypotheses done in the Bartlett lab involving PEC water oxidation on WO_3 | FeOOH.[1] Namely, the decrease in the quantity of hydroxyl radical generated during PEC water oxidation on WO_3 | FeOOH electrodes observed in this thesis work could contribute to the decrease in photocurrent density and increase in Faradaic efficiency for PEC water oxidation on WO_3 | FeOOH observed in the earlier work done in this lab. It was hypothesized that the low Faradaic efficiency for PEC water oxidation on bare WO_3 was largely due to electrolyte anion oxidation through the pathway of first oxidizing water to hydroxyl radical that then leaves the electrode surface to react with electrolyte. This is a parasitic reaction pathway since charge used for this reaction does not yield water as a product. What the work in this thesis demonstrates is that, by adding a thick enough layer of FeOOH, which has a valence band too negative to carry out oxidation of water to •OH, the hydroxyl radical production can be shut down during water oxidation, which would then lead to the cessation of the solvent oxidation pathway. Removing this parasitic reaction raises the Faradaic efficiency of WO_3 | FeOOH for PEC water oxidation. While this is the hypothesis, there are currently no experiments that have successfully detected phosphate oxidation products during PEC water oxidation on bare WO_3. Detection of these products, paired with their absence after PEC water oxidation on WO_3 | FeOOH, would be the final set of experiments needed to confirm this hypothesis.

Applying the oxyhydroxide-coated WO_3 to aqueous organic photoelectrocatalysis, it was discovered that no increase in Faradaic efficiency for benzyl alcohol oxidation to benzaldehyde was imparted to WO_3 by coating with either FeOOH, or another metal oxyhydroxide that had been shown to be an electrocatalyst for alcohol oxidation at pH=13, NiOOH.[2] It may be that more basic conditions are required for this catalysis to proceed. If this is true, then a layer that more protects WO_3 from basic conditions will need to be incorporated into this photocatalyst, or another visible

light-absorbing metal oxide will need to be chosen that inherently higher chemical stability under basic conditions. Being more base stable and absorbing significantly more visible light, $BiVO_4$ would be a suitable replacement. There are already reports of $BiVO_4 | FeOOH | NiOOH$ being used as a water oxidation catalyst, as well as a report on how to make $BiVO_4$ even more resilient under basic conditions.[3,4] These experiments could be useful starting points for implementing more base-stable metal oxyhydroxide-coated metal oxide photoelectrocatalysts for aqueous alcohol oxidations.

The photoelectrocatalytic oxidation of benzylamine on $CuWO_4$ photoanodes in Chapter 3 was shown to proceed with 75 ± 16% Faradaic efficiency for the production of *N*-benzylidenebenzylamine in nonaqueous conditions. However, there was a broad product distribution when *N*-methylbenzylamine was used as the starting amine. Most of the products can be accounted for by considering deprotonation of both the benzylic position and the terminal methyl position. This indicates the mechanism of amine oxidation on $CuWO_4$, and likely other metal oxides, is not amenable to high selectivity when there are methylene protons in more than one position alpha to the oxidized nitrogen atom. An interesting experiment would be to use cyclohexanemethylamine (a saturated analog of benzylamine) as the starting amine. The phenyl ring would no longer be present to stabilize the resulting carbon-centered radical after deprotonation of the carbon alpha to the nitrogen. Would the reaction still proceed? If so, how does its rate and selectivity compare to that of benzylamine? Another direction would be moving towards alcohol oxidation instead of amine oxidation. This direction is more in line with the goal of oxidizing biomass-derived compounds.

Chapter 4 demonstrated that the ability of $CuWO_4$ to photocatalyze benzylamine oxidation does not require an applied potential. A $CuWO_4$ powder was shown to catalyze benzylamine

oxidation in nonaqueous conditions under blue LED illumination to give *N*-benzylidenebenzylamine in 99% yield with a rate constant of 0.34 h^{-1} g^{-1}. This performance was compared to that of $BiVO_4$ powder, a more commonly investigated visible light-absorbing ternary metal oxide, which gave *N*-benzylidenebenzylamine in 98% yield at a rate constant of 0.70 h^{-1} g^{-1}. The next experiments to do would be to move to benzyl alcohol oxidation under identical conditions. It is likely that this reaction will be quite slow on $CuWO_4$. To help increase the rate of the reaction, $CuWO_4$ nanoparticles could be synthesized to increase the catalyst surface area. If this is insufficient, another metal oxide should be chosen that has a higher absorption coefficient. Another available route for alcohol oxidation is indirect oxidation of the alcohol via a mediator. There are examples of mediated oxidation from the Bartlett lab and others as ways to get around the sluggish charge transfer kinetics between the semiconductor and alcohol.[5–7] Instead, a mediator is included in the solution, which is a reactant that can undergo a facile one electron oxidation by a valence band hole in the photocatalyst, to then go on and participate in homogenous charge transfer with the alcohol away from the semiconductor surface.

While the photocatalytic alcohol oxidations presented in Chapter 5 were not particularly successful in terms of rates and selectivity, it was hopeful to see that the generation of formic acid from fructose and glycerol required all three light, catalyst, and acid. There may be a way to take advantage of this chemistry to boost the rate of this reaction. Also, while the rate of lactate formation from glycerol was very slow, the fact that Fe_2O_3 was able to catalyze it at all opens up room for this chemistry to be explored. This is thought to be the future work from this chapter that has the highest potential. It would be reasonable to replace Fe_2O_3, which has notoriously high charge recombination rates, with different base-stable metal oxide photocatalysts to catalyze glycerol oxidation. A good start may be $BiVO_4$ photoanodes with a thin layer of $ZnFe_2O_4$ deposited

as an overlayer, which have been shown to have increased photoelectrochemical stability in basic conditions during photoelectrocatalytic water oxidation as compared to bare $BiVO_4$.[4]

6.2 Outlook

6.2.1 Photoelectrocatalytic water oxidation on metal (oxy)hydroxide-coated metal oxides

The application of metal (oxy)hydroxides to underlying metal oxide visible light-absorbing semiconductors has been proven in this thesis and elsewhere to be a method of improving rates of electrocatalytic water oxidation over the bare metal oxide while reducing the reaction overpotential compared to the electrocatalyst alone.[3,8–11] While the role metal (oxy)hydroxide is still not completely understood, it has recently been shown by Boettcher and coworkers that the electrocatalyst facilitates charge separation in the metal oxide by collecting photogenerated holes.[12] In this work the electrochemical potential of the electrocatalyst was also measured and shown to reach positive enough values to carry out water oxidation, suggesting that the electrocatalyst uses the holes it harvests from the illuminated semiconductor to carry out water oxidation. With the fundamentals of these metal (oxy)hydroxide catalysts slowly being more understood, ways to improve these multicomponent photoelectrocatalysts can be better designed.

There is more progress to be made in improving these catalysts by focusing more on the electrocatalyst and the interface between the semiconductor and electrocatalyst layer rather than the semiconductor alone. Layered electrocatalysts may have benefits as well. This has already been demonstrated by Choi and coworkers who layered both FeOOH and NiOOH onto $BiVO_4$ photoanodes and showed that the highest current density and lowest overpotential for water oxidation was the electrode where FeOOH was first deposited onto $BiVO_4$ followed by a NiOOH deposition.[3] Switching the electrocatalyst deposition order or excluding either photocatalyst resulted in lower photocurrent density *and* higher overpotential. This demonstrates that the FeOOH

is a better hole collector while the NiOOH is a more efficient catalyst for water oxidation. When attempting to maximize kinetics for water oxidation, charge separation between the semiconductor and catalyst, and chemical stability during catalysis, it can be beneficial to utilize multiple electrocatalysts.

Identifying the active sites on metal (oxy)hydroxides during photoelectrocatalytic water oxidation would also greatly inform how to design more efficient electrocatalyst layers. Durrant and Choi have made progress on this largely unexplored front with very recent work that demonstrates for Ni/Fe oxyhydroxides (the most efficient Earth-abundant electrocatalysts known for water oxidation) that the accumulation of oxidized metal species is associated with the rate determining step (RDS) of water oxidation.[13] The metal center associated with water oxidation in mixed Ni/Fe oxyhydroxides also changes depending on the metal ratio; a Ni:Fe ratio of 0.21:0.79 has Fe associated with the RDS of water oxidation where a Ni:Fe ratio of 0.95:0.05 has Ni associated with the RDS of water oxidation. Maximizing the synergistic effects of these metals through the optimizing of the metal ratio would be a clear next step. Knowing the oxidation states of the metals responsible for the rate determining step of water oxidation may help in identifying other metals suited for this chemistry not previously considered.

6.2.2 Photo(electro)catalytic oxidation of biomass-derived compounds on metal oxides

The most common biomass-derived compound oxidized photo(electro)chemically has recently been 5-hydroxymethylfurfural. However, there exist few reports of this molecule being oxidized directly by valence band holes of metal oxides. Those reports that do exists describe this chemistry being done in organic solvents.[14,15] Choosing organic solvents prevents the possibility of the formation of hydroxyl radical during photocatalysis, which keeps selectivity for a single oxidation product in these reactions relatively high. However, given its high water solubility,

oxidizing 5-hydroxymethylfurfural in this greener solvent is ideal. There have been some reports of direct photocatalytic oxidation of 5-hydroxymethylfurfural in aqueous conditions, however, the heterogeneous catalysts used are not metal oxides.[16–18]

A reasonable way to begin to tackle aqueous organic oxidations is through photoelectrocatalytic oxidation where a metal oxide is used as the light absorber and is coated by some other catalyst with a valence band lacking the oxidation power to generate hydroxyl radical from water. The first of attempt of this by the Bartlett group was described in Chapter 2 of this thesis. The low Faradaic efficiency for alcohol oxidation in this system indicates that FeOOH and NiOOH are much more selective for water oxidation than alcohol oxidation, which was unexpected given that water oxidation requires the transfer of 4 protons and 4 electrons while benzyl alcohol oxidation only requires 2 protons and 2 electrons to be transferred and that NiOOH had been demonstrated to be an electrocatalyst for 5-hydroxymethylfurfural oxidation by Choi and coworkers.[2] Moving forward, materials that are highly efficient for water oxidation electrocatalysis should not be prioritized when experimenting with various materials as the overlayer for the light-absorbing metal oxide.

Basic conditions are commonly employed when oxidizing alcohols in aqueous conditions, be it photocatalytically, electrocatalytically, or thermally. If the stability of the photoelectrocatalyst allows, basic conditions should serve as the starting point for exploring photo(electro)catalytic aqueous oxidations. While chemistry in neutral conditions is desirable, more work should be accomplished in basic conditions favorable to alcohol oxidations before moving to more challenging neutral conditions. As alluded to at the end of section 6.1 of this chapter, a reasonable photoelectrocatalyst to first investigate for its capability to oxidize organic substrates in basic aqueous conditions is $BiVO_4 \mid ZnFe_2O_4$. The $ZnFe_2O_4$ imparts base stability to the photocatalyst

while also providing a less oxidizing valence band for the holes to transfer to before reaching the solution interface. ($ZnFe_2O_4$ has a valence band edge of 1.1 eV vs NHE).[4,19] While this material has shown water oxidation activity, it would be interesting to determine its Faradaic efficiency for 5-hydroxymethylfurfural oxidation.

6.3 References

[1] Lhermitte, C. R.; Verwer, J. G.; and Bartlett, B. M. Improving the stability and selectivity for the oxygen-evolution reaction on semiconducting WO_3 photoelectrodes with a solid-state FeOOH catalyst. *J. Mater. Chem. A* **2016**, *4*, 2960-2968.

[2] Taitt, B. J.; Nam, D.-H. and Choi, K.-S. A Comparative Study of Nickel, Cobalt, and Iron Oxyhydroxide Anodes for the Electrochemical Oxidation of 5-Hydroxymethylfurfural to 2,5-Furandicarboxylic Acid. *ACS Catal.* **2019**, *9*, 660-670.

[3] Kim, T. W. and Choi, K.-S. Nanoporous $BiVO_4$ Photoanodes with Dual-Layer Oxygen Evolution Catalysts for Solar Water Splitting. *Science* **2014**, *343*, 990-994.

[4] Kim, T. W. and Choi, K.-S. Improving Stability and Photoelectrochemical Performance of $BiVO_4$ Photoanodes in Basic Media by Adding a $ZnFe_2O_4$ Layer. *J. Phys. Chem. Lett.* **2016**, *7*, 447-451.

[5] Cha, H. and Choi, K.-S. Combined biomass valorization and hydrogen production in a photoelectrochemical cell. *Nature Chem.* **2015**, *7*, 328-333.

[6] Li, T.; Kasahara, T.; He, J.; Dettelbach, K. E.; Sammis, G. M. and Berlingguette, C. P. Photoelectrochemical oxidation of organic substrates in organic media. *Nature Communications* **2017**, *8:390*, 1-5.

[7] DiMeglio, J. L.; Breuhaus-Alvarez, A. G.; Li, S.; Bartlett, B. M. Nitrate Mediated Alcohol Oxidation on Cadmium Sulfide Photocatalysts. *ACS Catal.* **2019**, *9*, 5732-5741.

[8] Ge, G.; Liu, M.; Liu, C.; Zhou, W.; Wang, D.; Liu, L. and Ye, J. Ultrathin FeOOH nanosheets as an efficient cocatalyst for photocatalytic water oxidation. *J. Mater. Chem. A* **2019**, *7*, 9222-9229.

[9] Zhang, B.; Wang, L.; Zhang, Y.; Ding, Y. and Bi, Y. Ultrathin FeOOH Nanolayers with Abundant Oxygen Vacancies on $BiVO_4$ Photoanodes for Efficient Water Oxidation. *Angew. Chem. Int. Ed.* **2018**, *57*, 2248-2252.

[10] Kwong, W. L.; Lee, C. C. and Messinger, J. Transparent Nanoparticulate FeOOH Improves the Performance of a WO_3 Photoanode in a Tandem Water-Splitting Device. *J. Phys. Chem. C* **2016**, *120*, 10941-10950.

[11] Huang, J.; Ding, Y.; Luo, X. and Feng, Y. Solvation effect promoted formation of p-n junction between WO_3 and FeOOH: A high performance photoanode for water oxidation. *J. Catal.* **2016**, *333*, 200-206.

[12] Laskowski, F. A. L.; Nellist, M. R.; Qui, J. and Boettcher, S. W. Metal Oxide/(oxy)hydroxide Overlayers as Hole Collectors and Oxygen-Evolution Catalysts on Water-Splitting Photoanodes. *J. Am. Chem. Soc.* **2019**, *141*, 1394-1405.

[13] Francas, L.; Corby, S.; Selim, S.; Lee, D.; Mesa, C. A.; Godin, R.; Pastor, E.; Stephens, I. E. L.; Choi, K.-S. and Durrant, J. R. Spectroelectrochemical study of water oxidation on nickel and iron oxyhydroxide electrocatalysts. *Nat. Commun.* **2019**, *10*, 5208.

[14] Zhang, H.; Wu, Q.; Guo, C.; Wu, Y. and Wu, T. Photocatalytic Selective Oxidation of 5-Hydroxymethylfurfural to 2,5-Diformylfuran over Nb_2O_5 under Visible Light. *ACS Sustainable Chem. Eng.* **2017**, *5*, 3517-3523.

[15] Zhang, H.; Feng, Z.; Zhu, Y.; Wu, Y. and Wu, T. Photocatalytic selective oxidation of biomass-derived 5-hydroxymethylfurfural to 2,5-diformylfuran on WO_3/g-C_3N_4 composite under irradiation of visible light. *J. Photochem. Photobiol. A* **2019**, *371*, 1-9.

[16] Xu, S.; Zhou, P.; Zhang, Z.; Yang, C.; Zhang, B.; Deng, K.; Bottle, S. and Zhu, H. Selective Oxidation of 5-Hydroxymethylfurfural to 2,5-Furandicarboxylic Acid Using O_2 and a Photocatalyst of Co-thioporphyrazine Bonded to g-C_3N_4. *J. Am. Chem. Soc.* **2017**, *139*, 14775-14782.

[17] Han, G.; Jin, Y.-H.; Burgess, R. A.; Dickenson, N. E.; Cao, X.-M. and Sun, Y. Visible-Light-Driven Valorization of Biomass Intermediates Integrated with H_2 Production Catalyzed by Ultrathin Ni/CdS Nanosheets. *J. Am. Chem. Soc.* **2017**, *139*, 15584-15587.

[18] Battula, V. R.; Jaryal, A. and Kailasam, K. Visible light-driven simultaneous H_2 production by water splitting coupled with selective oxidation of HMF to DFF catalyzed by porous carbon nitride. *J. Mater. Chem. A* **2019**, *7*, 5643-5649.

[19] Song, H.; Zhu, L.; Li, Y.; Lou, Z.; Xiao M. and Ye, Z. Preparation of $ZnFe_2O_4$ nanostructures and highly efficient visible-light-driven hydrogen generation with the assistance of nanoheterostructures. *J. Mater. Chem. A* **2015**, *3*, 8353-8360.